Convective extreme precipitation at midlatitudes

Loriaux, Jessica

DOI
10.4233/uuid:c65bda5d-596d-4966-bdc5-20796d21d849

Publication date
2017

Document Version
Final published version

Citation (APA)
Loriaux, J. (2017). *Convective extreme precipitation at midlatitudes*. [Dissertation (TU Delft), Delft University of Technology]. https://doi.org/10.4233/uuid:c65bda5d-596d-4966-bdc5-20796d21d849

Important note
To cite this publication, please use the final published version (if applicable).
Please check the document version above.

Convective extreme precipitation at midlatitudes

Jessica Marie Loriaux

Convective extreme precipitation at midlatitudes
Thesis, Royal Netherlands Meteorological Institute (KNMI), Delft University of Technology

ISBN: 978-94-6299-513-0
Printing: Ridderprint BV
Cover design: Jessica Loriaux

Convective extreme precipitation at midlatitudes

Proefschrift

ter verkrijging van de graad van doctor
aan de Technische Universiteit Delft
op gezag van de Rector Magnificus Prof. Ir. K.Ch.A.M. Luyben,
voorzitter van het College voor Promoties,
in het openbaar te verdedigen op
woensdag 18 januari 2017 om 15:00 uur

door

Jessica Marie LORIAUX

Master of Science in Meteorologie, Fysische Oceanografie en Klimaat,
Universiteit Utrecht
geboren op 24 mei 1985 te Amsterdam

Dit proefschrift is goedgekeurd door de
promotor: Prof. Dr. A.P. Siebesma en
copromotor: Dr. G. Lenderink

Samenstelling promotiecommissie bestaat uit:

Rector Magnificus,	voorzitter
Prof. Dr. A.P. Siebesma,	Technische Universiteit Delft, promotor*
Dr. G. Lenderink,	Koninklijk Nederlands Meteorologisch Instituut, copromotor

Onafhankelijke leden:

Prof. Dr. H.J. Fowler,	Newcastle University
Dr. C. Hohenegger,	Max-Planck-Institut für Meteorologie
Prof. Dr. C. Muller,	Laboratoire de Météorologie Dynamique
Prof. Dr. H.J.J. Jonker,	Technische Universiteit Delft
Prof. Dr. H.W.J. Russchenberg,	Technische Universiteit Delft

*Tevens verbonden aan het Koninklijk Nederlands Meteorologisch Instituut

Dit proefschrift is onderdeel van Kennis voor Klimaat, thema 6.

"Life isn't about waiting
for the storm to pass.

It's about learning
to dance in the rain."

– Vivian Greene

Contents

Samenvatting

Ze zijn steeds vaker in het nieuws; zware regenbuien die tot files, overstromingen, en soms zelfs doden leiden. Naarmate de aarde steeds verder opwarmt kan de atmosfeer meer vocht vasthouden, met als gevolg dat er globaal gezien ook meer regen zal vallen. Gemiddeld genomen gaat dit om een toename van rond de 1-3% per graad opwarming, maar lokaal kan dit behoorlijk verschillen. En hoewel we de globaal gemiddelde respons op klimaatverandering redelijk goed begrijpen, is het gedrag van de extremen moeilijker te bepalen. Een belangrijke vraag is dan ook hoe extreme regenbuien zich zullen manifesteren in een toekomstig klimaat.

Om dit te kunnen bepalen, is het noodzakelijk om te begrijpen onder wat voor omstandigheden extreme buien eigenlijk plaatsvinden. Dit wordt bemoeilijkt doordat de relevante processen op verschillende tijd en ruimteschalen plaatsvinden. In deze dissertatie proberen we in kaart te brengen waardoor neerslagextremen bepaald worden, en hoe ze zich in een toekomstig klimaat zullen gedragen. Dit doen we door gebruik te maken van observaties en modellen met verschillende resoluties. Hierbij richten we ons op convectieve neerslagextremen. Dit zijn zware regenbuien die veroorzaakt worden door instabiliteit waarbij lucht snel opstijgt.

De hoeveelheid vocht die in de lucht opgenomen kan worden totdat verzadiging optreedt wordt beschreven door de Clausius-Clapeyron vergelijking. Wanneer de aanvoer van vocht onveranderd blijft, zou de neerslagintensiteit in de limiet waarin alles wat de lucht op kan nemen uitregent dus ook bepaald worden door deze vergelijking. Uit observaties boven Nederland is echter gebleken dat extreme neerslag een sterke toename laat zien van de neerslagintensiteit met

de temperatuur van 14% per graad, en dit komt ongeveer overeen met twee maal de Clausius-Clapeyron vergelijking.

In de literatuur is gesuggereerd dat deze verhoogde toename verklaard zou kunnen worden doordat de aanwezigheid van verschillende types neerslagextremen de statistiek zouden vervuilen. Wanneer enkel naar convectieve neerslagextremen gekeken zou worden, zou deze verhoogde toename dan niet meer zichtbaar zijn. In deze thesis tonen we echter met behulp van observaties aan dat deze relatie wel degelijk gevonden wordt voor convectieve neerslagextremen. Door de temporele resolutie te verhogen van uurlijks naar 10 minuten bestaan de extremen in de dataset in grotere mate uit convectieve buien. In plaats van een Clausius-Clapeyron toename van 7% per graad, zien we juist dat de geobserveerde toename van 14% per graad over een groter temperatuurinterval geldig is dan voor de uurlijkse data. Hieruit concluderen we dat de geobserveerde toename van 14% per graad robuust is voor convectieve neerslagextremen boven Nederland.

Door middel van een conceptueel model kunnen we vervolgens beter kijken naar de lokale processen die de relatie tussen de neerslagintensiteit en temperatuur beïnvloeden. Twee processen blijken de toename in de neerslagintensiteit te bepalen: de vochtflux aan de wolkenbasis en de laterale vochtconvergentie in de wolk. Het eerste proces wordt voornamelijk door de Clausius-Clapeyron relatie bepaald. Laterale vochtconvergentie (de hoeveelheid vocht die de wolk in getrokken wordt) wordt daarnaast ook beïnvloed door het verticale snelheidsprofiel, en leidt daardoor tot een sterkere toename in de neerslagintensiteit. Immers, wanneer de opwaartse beweging toeneemt, moet die lucht vanuit continuiteitsoverwegingen ook weer aangevuld worden. Hierdoor wordt er dan per graad ook meer van die vochtige lucht een wolk in gezogen, waardoor de neerslagintensiteit sterker toe kan nemen dan verwacht op basis van enkel de Clausius-Clapeyron vergelijking.

Deze versterkte toename blijkt samen te hangen met de mate waarin het temperatuurprofiel van de atmosfeer, en daarmee ook de stabiliteit, verandert ten gevolg van de opwarming van de aarde. In de tropen wordt de atmosferische stabiliteit redelijk constant geacht met opwarming, maar op middelbare breedtegraden verwachten we een afname in de stabiliteit van de atmosfeer. Daardoor kunnen we hier een sterkere klimaatrespons van extreme neerslag verwachten.

Met behulp van modeluitkomsten en observaties hebben we vervolgens in kaart gebracht welke grootschalige omstandigheden typerend zijn voor buien van verschillende sterktes. Buien met hoge neerslagintensiteiten vinden aantoonbaar plaats onder warmere, vochtigere omstandigheden dan zwakkere buien. Bovendien vinden zware buien plaats in een instabielere atmosfeer en met sterkere grootschalige vochtconvergentie dan zwakkere buien. Deze eigenschappen laten een steeds grotere verandering met de tijd zien naarmate de buiensterkte toeneemt.

De bovengenoemde inzichten zijn vervolgens gebruikt om realistische simulaties van extreme neerslag te draaien in een kleinschalig model met hoge resolutie. Bijzonder hieraan is onder meer de tijdsafhankelijke aansturing van het model. Binnen deze experimentele opzet zijn gevoeligheidsexperimenten gedaan door systematische veranderingen in de relatieve luchtvochtigheid, stabiliteit en grootschalige vochtconvergentie toe te passen. Hieruit zijn een aantal belangrijke uitkomsten naar voren gekomen. Zo blijkt dat de totale neerslag toeneemt met relatieve luchtvochtigheid, instabiliteit en grootschalige vochtconvergentie. Decompositie van de totale neerslag in neerslagintensiteit en de oppervlaktefractie (de fractie van het domein waarin neerslag valt) laat zien dat de instabiliteit en de vochtconvergentie die toename op verschillende manieren realiseren. De instabiliteit vergroot namelijk de neerslagintensiteit, maar heeft nauwelijks invloed op de oppervlaktefractie, terwijl de grootschalige vochtconvergentie met name de oppervlaktefractie vergroot, zonder grote impact op de neerslagintensiteit te hebben.

Deze gevoeligheidsexperimenten zijn herhaald voor een warmer klimaat. Hieruit blijkt dat de relaties die voor het huidige klimaat gevonden zijn, ook in een toekomstig klimaat blijven gelden. De klimaat respons van extreme neerslagintensiteiten is met zo'n 7% per graad lager dan verwacht, maar is hoger dan de respons van de totale neerslag, doordat de oppervlaktefractie in de klimaat simulaties afneemt. Dit betekent dat het in een warmer klimaat harder, maar minder vaak zal regenen.

Summary

Reports of extreme precipitation events are becoming more frequent in the news; they are causing traffic jams, floods, and even loss of life. As a result of global warming, the atmosphere will be able to retain more moisture, which means that globally, precipitation will increase. On average, this increase amounts to approximately 1-3% per degree warming, but locally the precipitation increase can deviate from this quite a bit. And although we have a fairly good understanding of the global mean response to climate change, the behavior of the extremes is more difficult to determine. Therefore, an important question is how events of extreme precipitation will manifest in a future climate.

To determine this, it is necessary to understand the circumstances leading to extreme events. This is complicated by the large range of spatial and temporal scales at which relevant processes take place. In this thesis we try to assess the processes and conditions controlling precipitation extremes, and determine the behavior of these events in a future climate. This is done by using observations and various models with different resolutions. The focus of this thesis is on convective precipitation extremes. These are heavy rainfall events that are caused by instability, where the air rises quickly.

The amount of water vapor that air can hold until saturation occurs is described by the Clausius-Clapeyron equation. If the moisture supply remains unchanged, in the limit where all the moisture that the air can take in is precipitated out, the precipitation intensity would also be described by this equation. However, observations over the Netherlands indicate a 14% per degree rise in extreme precipitation intensity with temperature, which corresponds to approximately twice the Clausius-Clapeyron relation.

It has been suggested in the literature that this enhanced increase could be a statistical artifact caused by the presence of different precipitation types affecting the statistics. If only convective precipitation extremes were analyzed, this enhanced increase would vanish. However, using observations, in this thesis we show that this relation does hold for convective extremes. By increasing the temporal resolution from hourly to 10 minutes, extremes in the dataset are made up of a larger amount of convective events. Rather than a Clausius-Clapeyron induced increase of 7% per degree, we see that the observed 14% per degree increase is valid over a larger temperature interval than for the hourly data. From this we conclude that the observed increase of 14% per degree is robust for convective extremes over the Netherlands.

Using a conceptual model we can better assess the local processes that determine the relationship between rainfall intensity and temperature. Two processes seem to determine the increase in the precipitation intensity; the moisture flux at the cloud base and the lateral moisture convergence in the cloud. The first process is mainly determined by the Clausius-Clapeyron relation. Lateral moisture convergence (the amount of moisture that is drawn into the cloud) is also enhanced by the strength of the updraft in the cloud, and as a result leads to a stronger increase in rainfall intensity. After all, when upward motions increase, continuity dictates that this air must also be replenished. As a result, more of that moist air is drawn into the cloud per degree warming, allowing the precipitation intensity to increase by more than expected based on the Clausius-Clapeyron equation alone.

This enhanced increase appears to be related to the extent to which the temperature profile of the atmosphere, and hence also the stability, changes as a result of the global warming. In the tropics the atmospheric stability is considered to be fairly constant with warming, but in the midlatitudes, a decrease in the atmospheric stability is expected. Therefore we can expect a stronger climate response of extreme precipitation there.

Using model results and observations we have mapped the large-scale conditions typical for showers of different strengths. Showers with high precipitation intensities are shown to take place under warmer, more humid conditions than weaker events. Moreover, strong precipitation events take place in an unstable atmosphere with stronger large-scale moisture convergence than weaker events.

These properties show a strengthening temporal signal with increasing rainfall intensity.

The aforementioned insights have been used to perform realistic simulations of extreme precipitation using a high resolution cloud resolving model. What makes this setup stand out amongst other things is that the model is driven by realistic, time dependent conditions. Within this experimental setup, sensitivity experiments have been performed by systematically perturbing the relative humidity, stability and large-scale moisture convergence. This has lead to several important results. The total precipitation is shown to increase with humidity, instability and large-scale moisture convergence. Decomposition of the total precipitation into the precipitation intensity and the area fraction (the fraction of the domain where it has been raining) shows that the instability and moisture convergence realize growth in different ways. While the instability increases the precipitation intensity, but has little impact on the area fraction, the large-scale moisture convergence mainly increases the area fraction, without having a large effect on the precipitation intensity.

These sensitivity experiments have been repeated for a warmer climate. They show that the relations found for the present-day climate, continue to hold in a future climate. With an increase of approximately 7% per degree warming, the climate response of extreme precipitation intensities is lower than expected, but higher than the response of the total rainfall, because the area fraction decreases in the climate simulations. This means that in a warmer climate, it will rain less, but more intensely.

1

Introduction

While I write this, Western Europe is being plagued by incessant high-intensity precipitation. The combination of high intensities and long durations are causing streets to flood and rivers to overflow. Parts of Paris have been evacuated, and flash floods have led to fatalities in Germany, France and Belgium. These extremes could in part be attributed to climate change (van Oldenborgh et al., 2016). So far, these heavy precipitation events have only caused material damages and traffic disruptions in the Netherlands. Even so, the damage caused by heavy showers is running into the hundreds of millions of Euros in the Netherlands alone (NRC, 2016). Clearly, events of extreme precipitation can have a strong societal impact.

Figure 1.1 shows the meteorological conditions over the Netherlands on the 30th of May, 2016, a day with very heavy precipitation. The radar image (a) shows a large band of strong precipitation intensities between 10 and 100 mm/h over the southwest of the Netherlands at 17:00 local time. As a result, the daily cumulative precipitation peaks around 70 mm (b). The weather map (c) shows the meteorological conditions at 18 UTC, which accompany these intensities. The band of high precipitation seen in (a) corresponds to a convergence line (red line) ahead of a cold front (blue line with triangles). The convergence line indicates strong upward motion, leading to high precipitation intensities. In this case, the band of precipitation remained fairly stationary over the course of a couple of hours, increasing the local impact of this particular event.

This example illustrates that precipitation intensity and duration are two important factors controlling the impact of a precipitation event. Apart from this, it is also important to know the frequency of occurrence; can we expect an

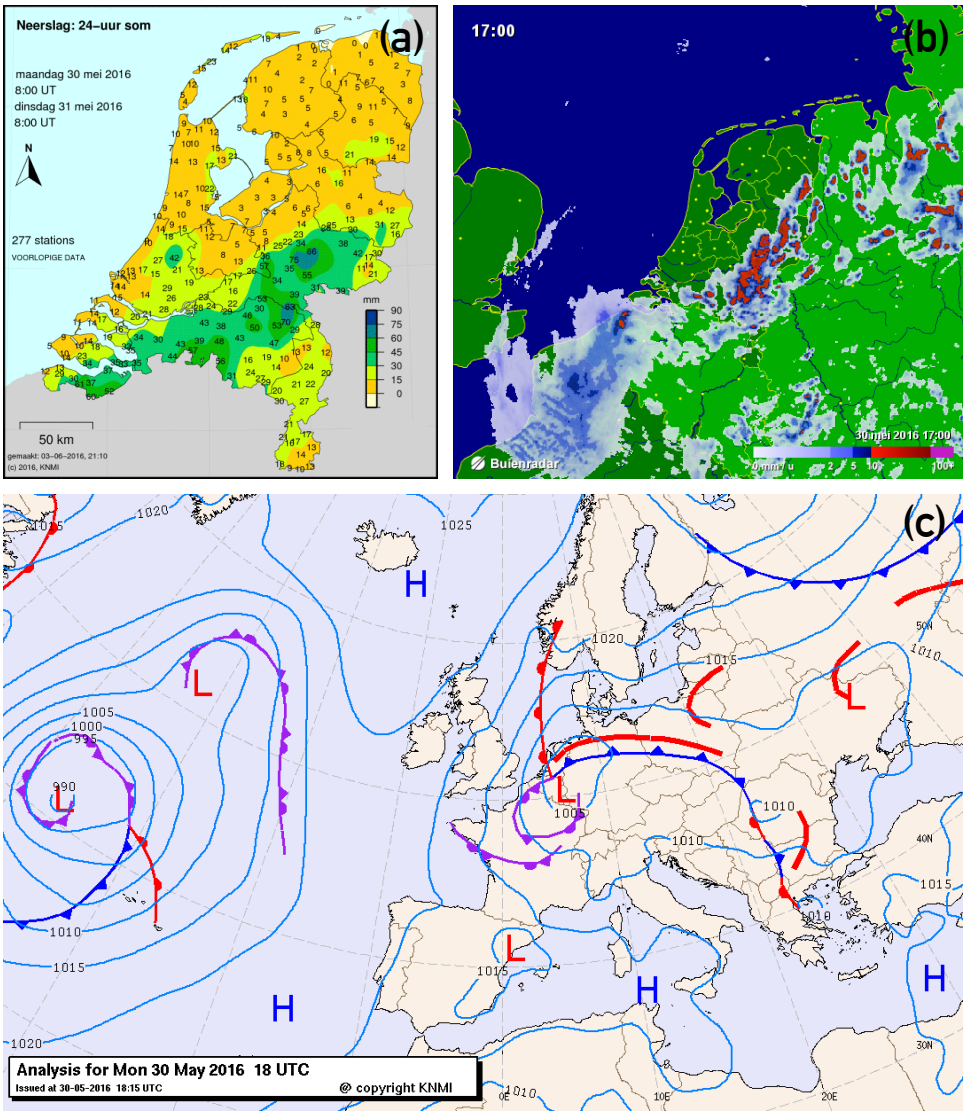

Figure 1.1: Weather conditions over the Netherlands on 30 May 2016, with (a), the daily sum of precipitation over the Netherlands (KNMI, 2016a), (b), the radar image at the time of the extreme event (Buienradar, 2016), and (c), the synoptic weather map at 18 UTC (KNMI, 2016b).

event of a certain magnitude once in a lifetime, or once a year? And how will precipitation change in the future climate? It is important to know the answer to these kind of questions for making policy decisions.

This example also shows that extreme precipitation events and the processes leading up to them span a large range of temporal and spatial scales. In this thesis we expand the knowledge on precipitation extremes by using a multi-scale approach to determine and understand present-day sensitivities of extreme precipitation intensities to local and large-scale conditions. Furthermore, idealized climate change perturbations (i.e., increasing the atmospheric temperature while keeping the relative humidity constant) are used to ascertain how these sensitivities respond to a warmer climate.

1.1 Precipitation

The atmosphere contains moisture in the form of water vapor, condensed water and ice. Precipitation occurs when water vapor condensates, and cloud droplets form. Initially, these droplets are small enough to float in suspension in clouds, but as they grow, they eventually become large enough to fall from the sky. This typically starts to happen when the amount of condensed water exceeds 1 gram per kilogram of air. The mechanisms of droplet formation and growth will not be further discussed in this thesis, as these aren't expected to be a dominant influence on extreme precipitation.

Condensation and precipitation occur when the air cools, leading to saturation. This is generally the result of rising motion. Rising unsaturated air cools at a rate of 9.8 K km^{-1} due to adiabatic expansion.The underlying mechanism causing the air to rise, determines the type of precipitation that will fall. Precipitation can occur due to atmospheric instability, large-scale lifting, or orographic lifting. The first generation type leads to convective precipitation, while the latter two lead to dynamic precipitation.

Dynamic precipitation

Dynamic, in this case, refers to the large-scale processes forcing the air to lift, such as is the case with weather fronts. Weather fronts are associated with

large-scale low pressure systems, often referred to as depressions. Large-scale lifting at fronts occurs either by a cold air mass pushing up warmer air (cold fronts), or by a warm air mass moving over cold air (warm front). As the air rises and cools, the moisture holding capacity decreases and the air becomes oversaturated. At that stage, clouds start to form by condensation, which may lead to precipitation if the cloud condensate has increased sufficiently.The air remains statically stable, which means that its density is in equilibrium with its surroundings, and the air does not want to move to a different level. Since this type of precipitation tends to fall from nimbostratus clouds figure 1.2 (a), it is also known as stratiform precipitation. Stratiform precipitation is characterized by weak to moderate precipitation intensities, and takes place over a relatively large area, depending on the system it is associated with. Due to its relatively long life span, this type of precipitation can lead to a large amount of rainfall on a daily scale.

Another type of precipitation connected to forced lifting is called orographic precipitation. Instead of air being lifted due to large-scale processes, moist air is blown over a mountain.

Convective precipitation

Convective precipitation can occur when the atmosphere is conditionally unstable. A parcel of air needs to become buoyant for convection to occur; for example due to the sun's warming of the surface in the morning. After becoming buoyant, the parcel starts to rise adiabatically, cooling at a rate of 9.8 K km^{-1}. This process is referred to as moist convection, and tends to be more vigorous than forced lifting. As a result, condensation of water vapor occurs faster too. This type of precipitation falls from cumulonimbus clouds figure 1.2 (b), and, due to its rapid formation, is characterized by high intensities. As the air rises it mixes with its environment, stabilizing the atmosphere. As a result, convective precipitation events tend to be relatively short lived, and take place on a local scale.

Figure 1.2: Nimbostratus over the Hardangervidda, Norway (a), and a convective shower over 's-Hertogenbosch, the Netherlands (b, picture taken by Geert Lenderink).

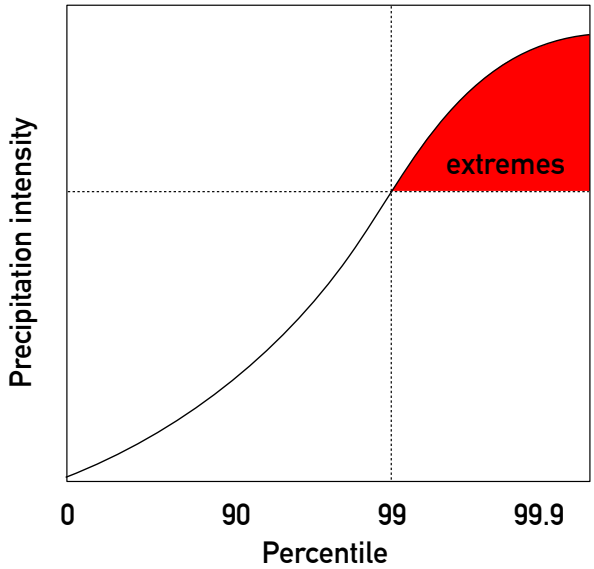

Figure 1.3: Conceptual diagram of a cumulative density function of the precipitation intensity. In this thesis, intensities exceeding the 99th percentile of the distribution are deemed extreme.

Caveat

Stratiform precipitation is often referred to as frontal precipitation. However, it is important to note that air that is initially forced upwards may eventually become unstable. This means that in frontal systems, convective precipitation may exist alongside stratiform precipitation. Similarly, orographic precipitation may consist of both types of precipitation. This makes it hard to distinguish between the two in precipitation observations.

1.2 Extreme precipitation

It has already become clear from the previous section that precipitation can take place in many shapes and forms. Statistically speaking, mean and extreme precipitation may behave very differently, as they may be represented by different physical processes and controlling factors.

If we consider a precipitation distribution (figure 1.3), extreme precipitation

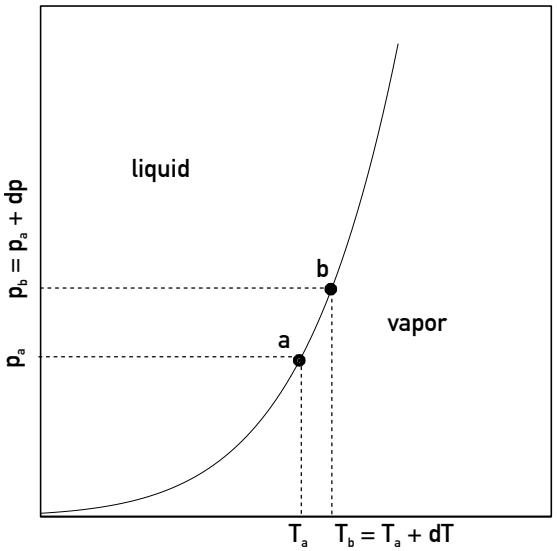

Figure 1.4: p-T diagram of the liquid-water equilibrium line.

is typically defined as events which fall above a certain threshold, often in terms of percentiles. In this thesis, we consider precipitation intensities at and above the 99th percentile to be extreme. In other words, extreme precipitation is precipitation which only occurs 1% of the time. This is still a loose definition, because precipitation can be measured at different temporal resolutions, e.g. monthly, daily or hourly, which will highlight different types of precipitation. For example, an extremely wet month or day may be caused by a large amount of stratiform precipitation, which on an hourly basis may not be out of the ordinary, but does add up over a longer period. On the other hand, hourly, and more so, sub-hourly precipitation extremes are more likely to be formed by short-lived convective precipitation, with high intensities. In this thesis, we focus on the latter.

1.3 The Clausius-Clapeyron relation

Condensation occurs when the atmosphere becomes saturated. The thermodynamic circumstances leading to condensation and evaporation are described

by the Clausius-Clapeyron relation. This relation is a key identity for extreme convective precipitation, and will be derived in this section.

For the phase transition between water vapor and liquid water, saturation occurs when the amount of evaporation is in equilibrium with the amount of condensation. The Clausius-Clapeyron (CC) equation describes the slope of the equilibrium curves of a substance (in this case water) in a pressure-temperature (p-T) phase diagram (figure 1.4). It follows from Gibbs energy constraints. Gibbs energy (g) is a thermodynamic potential that can be used to determine the amount of free energy of a system at constant temperature and pressure

$$g = u + pv - sT \tag{1.1}$$

where u is the internal energy, v the volume and s the entropy of the system per unit mass. T is the absolute temperature.

In equilibrium, two phases can only coexist if they have the same Gibbs energy. Therefore, at the equilibrium line shown in figure 1.4, $g_l = g_v$. This can be used to derive the slope of the equilibrium line.

Given two points at equilibrium, a and b, the difference in Gibbs free energy between these points is $\delta g = g_b - g_a$. Per definition, this holds for both liquid and vapor particles, $\delta g_l = \delta g_v$. However, we also know that

$$dg_l = v_l dp - s_l dT$$
$$dg_v = v_v dp - s_v dT$$

Rearranging leads to the following equation

$$\frac{dp}{dT} = \frac{s_l - s_v}{v_l - v_v}, \tag{1.2}$$

which gives the slope of the equilibrium line. This is the Clausius-Clapeyron equation. If the phase change is reversible under constant temperature and pressure conditions, the entropy of phases i and ii can be written as

$$L_{i,ii} = T(s_{ii} - s_i).$$

For the equilibrium between liquid water and water vapor, v_l is negligible with respect to v_v. Using the ideal gas law for water vapor, $e_s v_v = R_v T$, leads to the more traditional form of the Clausius-Clapeyron equation,

$$\frac{de_s}{dT} = \frac{L_v e_s}{R_v T^2}, \tag{1.3}$$

describing the relation between the saturation vapor pressure e_s and temperature. The saturation vapor pressure is the pressure of the water vapor at which the air becomes saturated, i.e. when an equilibrium between vaporization and condensation occurs. Here, $L_v = 2.5\ 10^6$ J kg^{-1} at 0 K, denotes the latent heat of vaporization.$R_v = 461.5$ J K^{-1} kg^{-1} gives the gas constant of water vapor.

In this thesis, when referring to the Clausius-Clapeyron relation it is implicitly assumed that we are talking about the phase transition between water vapor and liquid water described by equation (1.3). A frequently used approximation (e.g., Bolton, 1980; Emanuel, 1994; Stull, 1988) of the integrated version of this equation is

$$e_s = 6.112 \exp\left(\frac{17.67(T - 273.16)}{T - 29.66}\right), \tag{1.4}$$

which is accurate to within 0.3% in the range of ± 35 °C. Returning to figure 1.4, it can be seen that if the temperature increases from T_a to T_b, the saturation pressure increases exponentially from $e_{s,a}$ to $e_{s,b}$. Simply put, warm air can hold more water vapor than cold air.

It is often proposed (Trenberth et al., 2003) that the saturation vapor pressure at the surface is proportional to the maximum precipitation rate that can fall (see section 1.4). This is where the slope of the saturation curve becomes relevant, as it dictates an exponential increase with temperature. The relative increase in e_s per °C depends on the initial temperature. Given a typical midlatitudinal surface temperature of 10 °C, an increase of 1 °C leads to an increased saturated water vapor pressure of close to 7%. In tropical regions, the increase is smaller; with an initial temperature of 30 °C, e_s increases by approximately 6% °C^{-1}. For the tropics and midlatitudes the CC rate is therefore generally approximated to be 6-7% °C^{-1}, based on their surface temperatures. Note

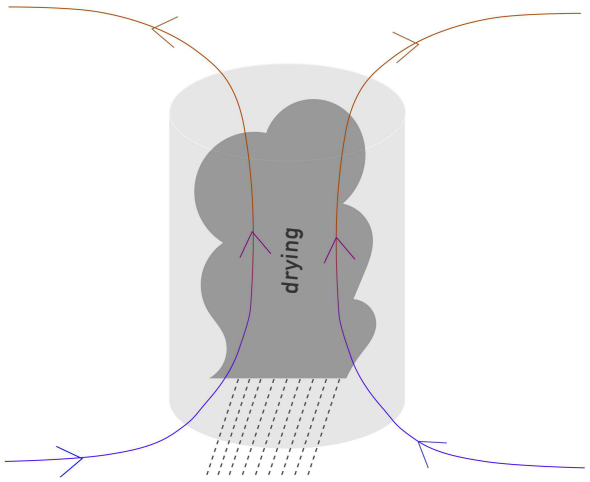

Figure 1.5: Schematic representation of moist air converging into a column of air, rising and saturating as a result of adiabatic cooling, forming a precipitating cloud. Drier air diverges from the column.

that higher up in the atmosphere, the slope is stronger. An initial temperature of -30 °C leads to an increase in e_s of approximately 10% $°C^{-1}$. This becomes important when considering atmospheric profiles, rather than surface parameters.

1.4 (Thermo)dynamics of extreme precipitation

It is well established that in a warmer climate, precipitation will increase. As the temperature rises, the moisture holding capacity of the atmosphere increases by 6-7% $°C^{-1}$, following the CC relation (1.3). However, it has been shown that on a global scale precipitation is constrained not by the amount of moisture available, but by the energy budget of the atmosphere (e.g. Allen & Ingram, 2002; Stephens & Ellis, 2008), leading to a mean precipitation response to global warming of 1-3% K^{-1}.

Locally, the precipitation response can deviate from this amount. This is also true for different percentiles of the precipitation distribution. It is expected that convective precipitation extremes follow (thermo)dynamic scaling relations. These relations will be discussed below.

Clausius-Clapeyron scaling (thermodynamics)

Vapor pressure, e, is proportional to the specific humidity, q, which gives the mass of water vapor per kg of air. Analogously, $e_s \propto q_s$, where q_s, the saturation specific humidity (kg kg_{air}^{-1}), gives the amount of water vapor the atmosphere can hold until saturation occurs. A better known quality, the relative humidity, relates the amount of water vapor in the air to the amount of water vapor at saturation, given a certain temperature;

$$RH \equiv \frac{e}{e_s(T)} \approx \frac{q}{q_s(p,T)}. \tag{1.5}$$

Consider a column of air where air is lifted and cools, transporting moisture from the surface upwards until it starts to precipitate. The air at the bottom is replaced by new air through convergence (figure 1.5). As a result, moisture converges at the lower levels and is transported into the column. Low level convergence of air has to be balanced by diverging air at higher levels; what goes in, must come out. The diverging air at higher levels is drier than the air coming in, since the moisture holding capacity decreases with height. In the most extreme case, the diverging air contains no more moisture, and the precipitation intensity (P) should eventually balance the inflow of moisture near the surface.

$$P \propto q \propto e \equiv e_s(T_d). \tag{1.6}$$

Here, we have introduced the dew point temperature, T_d, which is defined as the temperature at which an air parcel with vapor pressure e becomes saturated. This is where the CC relation comes into play. The precipitation response (P_2/P_1) to an increase in dew point temperature from $T_{d,1}$ to $T_{d,2}$ can be written as

$$\frac{P_2}{P_1} = \frac{e_s(T_{d,2})}{e_s(T_{d,1})}. \tag{1.7}$$

This shows that convective extreme precipitation intensities increase with T_d following a CC increase of 6-7% $^{\circ}C^{-1}$. This will be referred to as CC scaling.

Several studies have shown that the relative humidity at midlatitudes is reasonably unchanged as a result of global warming (Sherwood et al., 2010;

Dal Gesso et al., 2014). In that case we can write

$$\frac{P_2}{P_1} = \frac{RHe_s(T_2)}{RHe_s(T_1)} \approx \frac{e_s(T_2)}{e_s(T_1)}. \tag{1.8}$$

In other words, if the relative humidity remains constant, convective extreme precipitation intensities increase with T following the CC relation.

Enhanced moisture convergence (dynamics)

Above, it was implicitly assumed that the low-level moisture convergence is unaffected by temperature. However, for convective precipitation, the increase in temperature may lead to stronger updrafts, and thus stronger moisture convergence. The near-surface moisture convergence is proportional to the near-surface wq, where w is the large-scale vertical velocity. If $P \propto wq$ and RH is again assumed to be constant with temperature, equation 1.6 becomes

$$P(T) \propto w(T)q(T) \propto w(T)e_s(T). \tag{1.9}$$

The precipitation response can then be written as

$$\frac{P_2}{P_1} = \frac{w(T_2)}{w(T_1)} \frac{e_s(T_2)}{e_s(T_1)}. \tag{1.10}$$

This shows that apart from the CC component (thermodynamic contribution), the precipitation response can also be influenced by on the change in the vertical velocity, a dynamical contribution.

The scaling relations presented here, offer a simplified view of the precipitation response to temperature change. Present-day observations in different climatic regions give a large range of relations between precipitation extremes and temperature. While CC scaling was found by Hardwick-Jones et al. (2010a); Utsumi et al. (2011) over a large range of temperatures, Lenderink & Meijgaard (2008); Lenderink et al. (2011) found an increase in precipitation intensity approximately following CC scaling for dew point temperatures below 15 K, but twice CC (2CC) scaling for higher dew point temperatures. This supports the

theory that dynamical processes also influence the relation between precipitation and temperature O'Gorman & Schneider (2009a); Emori & Brown (2005); Trenberth et al. (2003).

It is important to note that the present-day relations between precipitation and temperature may not necessarily hold for global warming (Westra et al., 2014). There have been several studies investigating the precipitation response to climate perturbations and the physics behind it, in terms of thermodynamical and dynamical components. Studies based on general circulation models (GCMs, e.g. O'Gorman & Schneider, 2009a,b) provide a global overview of the response, with results varying from sub- to super-CC scaling depending on the latitude. However, GCMs have a coarse spatial resolution, and as a result convection has to be calculated indirectly, which reduces the reliability for strong convective processes that we are interested in.

Alternatively, high resolution, convection permitting cloud-resolving models (CRMs) and large-eddy simulation (LES) models have been used to perform idealized experiments in a tropical setting (e.g. Muller et al., 2011; Romps, 2011; Muller, 2013). The precipitation response for the above mentioned studies remains relatively close to CC scaling, but shows different dynamical contributions depending on the study.

Several case studies of extreme events focusing on midlatitudes using CRMs have been able to reproduce the super-CC scaling response to perturbations found in observations (Singleton & Toumi, 2013; Attema et al., 2014). Attema et al. (2014) examined the precipitation responses to climate change for 11 cases of extreme precipitation. While the mean response is consistent with observations (between 9 and 11% K^{-1}), the differences between cases vary from zero to 18% K^{-1}. This indicates that while the conceptual mechanisms described here might play an important part in the precipitation response, individual precipitation events are controlled by many factors.

1.5 Multi-scale approach

One of the main challenges of understanding precipitation extremes is that it spans many spatiotemporal scales (figure 1.6) and therefore requires analysis of

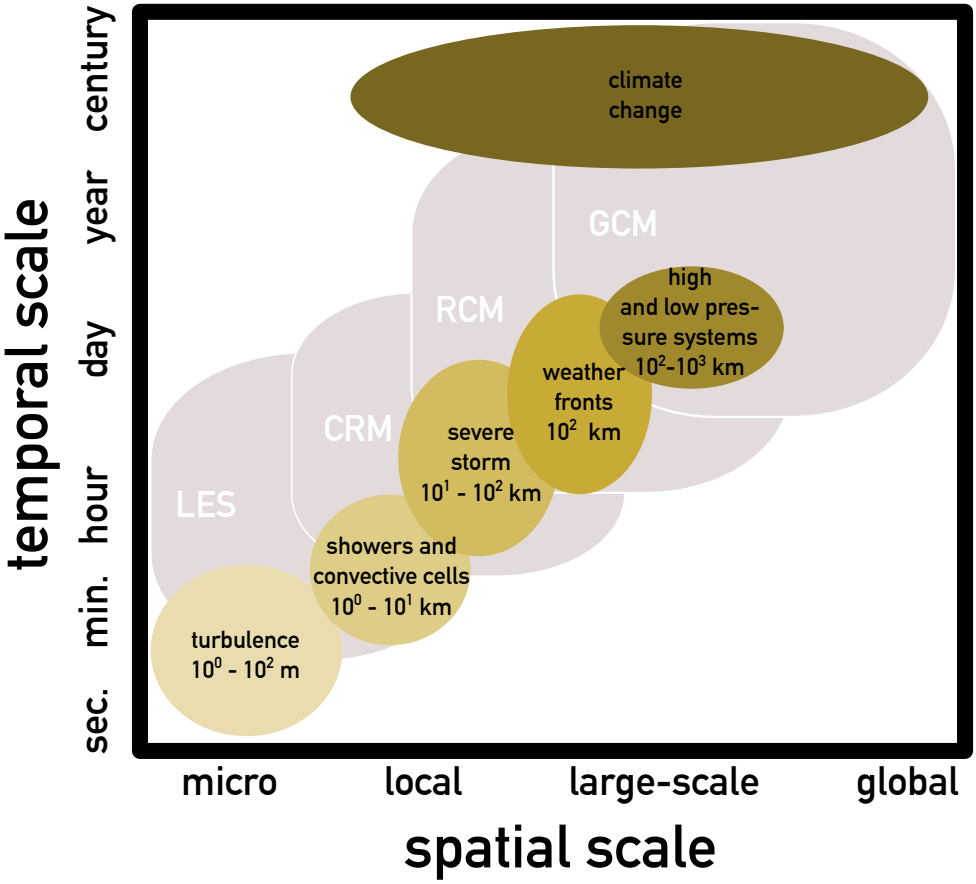

Figure 1.6: Diagram depicting the different temporal and spatial scales of relevant meteorological phenomena and the scales that can be represented by a large-eddy simulation (LES) model, cloud resolving model (CRM), regional climate model (RCM), and global circulation model (GCM).

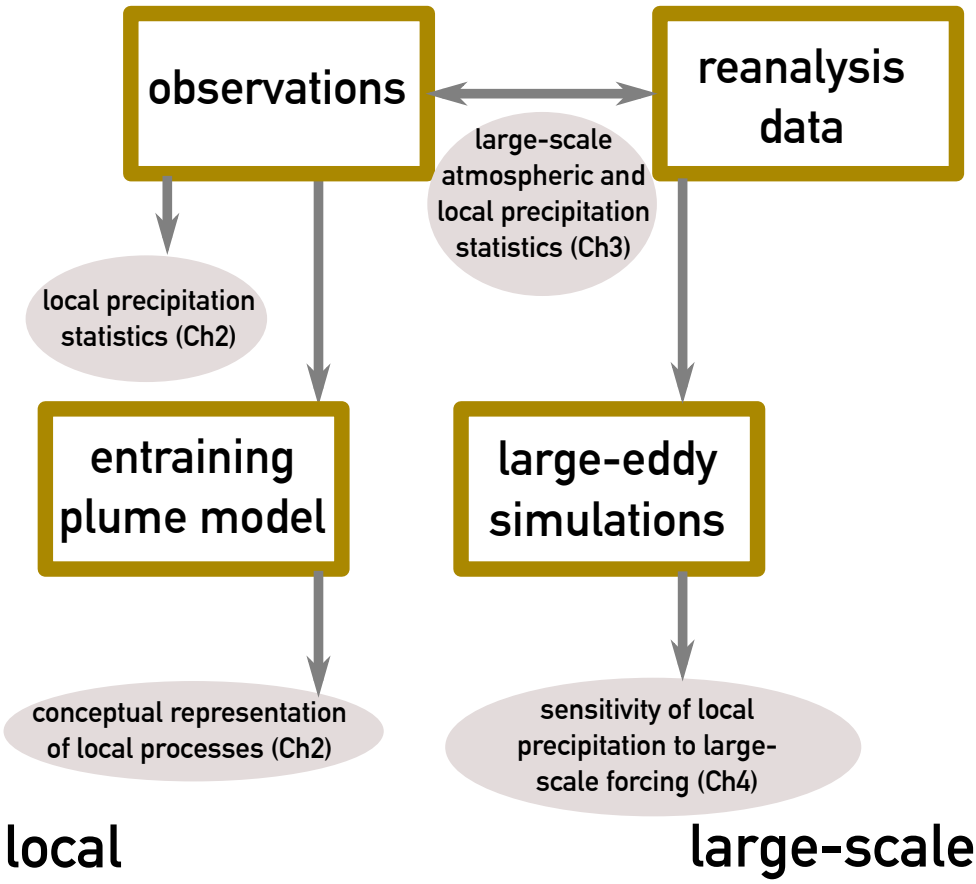

Figure 1.7: Chart showing how, and for what purpose, the different models and data sets used in this thesis were combined to investigate different components of extreme precipitation. These methods are ordered from local (left) to large-scale (right) spatial scales.

the problem from different angles. Rain showers (1- 10 km) and more organized storms (up to 100 km) can be influenced by large-scale meteorological processes (100-1000 km). Analogously, the temporal scale of these processes ranges from minutes to days. And when climate change is considered, even centuries.

Since there is no single model that can cover all of these scales, in this thesis, we have made use of several methods to ascertain a more complete overview of the driving factors behind convective extreme precipitation. This section gives an overview of how we combined different methods to connect different processes and theories. Figure 1.7 shows a schematic of how local and large-scale methods were combined and used to work out different aspects of extreme precipitation. A brief description of each method and why it was chosen follows below.

Observations

Local conditions such as precipitation intensities, are most accurately measured from observations. Therefore, observations play an important role in this thesis. We have used automated weather station (AWS) measurements over the Netherlands (KNMI, 2014) for hourly, and 10 minute precipitation data. In addition, we have used AWS observations of surface data (e.g., temperature, relative humidity) at an hourly resolution for realistic surface conditions. These data are used to determine local present-day sensitivities of precipitation extremes to surface conditions over the Netherlands in chapter 2. They are also combined with reanalysis data, and used as input in a conceptual model. This will be further discussed in the paragraphs describing these methods.

Reanalysis data

For accurate, large-scale processes such as forced lifting and other atmospheric profile conditions, observations are not available. Instead, reanalysis data which is downscaled to a 12 km horizontal resolution with a regional climate model (RCM) is used for this purpose. Reanalysis data is obtained by assimilating all available observations into a weather model at set intervals (e.g., every 12 hours), thus recreating an accurate and uniform data set of day to day weather and climate conditions. In order to determine large-scale atmospheric conditions

associated with high intensity precipitation events, a regional climate model forced by reanalysis data was used in combination with the AWS precipitation observations (chapter 3). A time dependent, composite mean case setup based on realistic extreme conditions was created to use as input for the large-eddy simulation model in chapter 4.

Conceptual model

In order to test conceptual theories on the local scale in a highly controlled, idealized setup, an entraining plume model was used in chapter 2. The entraining plume model is a conceptual tool to simulate the ascent of a buoyant air parcel, given prescribed atmospheric background conditions. To this end, sounding profiles at the KNMI at noon were combined to create an idealized convective profile.

The model is based on the governing equations of dry static energy s, specific humidity q_v, and liquid water specific humidity q_l. It can be used to determine relevant quantities such as the height to which the parcel will rise, the vertical velocity profile of the parcel, and the convective available potential energy (CAPE), a measure of the atmospheric instability. Furthermore, the height at which a parcel becomes saturated, and the condensation rate during its ascent can be calculated. This model has been used in combination with an atmospheric profile based on radiosonde data to determine local physical properties and processes involved in extreme precipitation intensities. A thorough description of the entraining plume model can be found in section 2.3.

Large-eddy simulation model

When studying physical processes, the conceptual model described above is useful for better qualitative understanding, but cannot be used as a substitute for three dimensional models which capture the dynamics and variability up to the model resolution. Since convective updrafts and precipitation events have typical length scales in the order of a hundred meters to a few kilometers (figure 1.6), a high horizontal resolution model is needed. A large-eddy simulation (LES) model, has an even higher resolution than the CRM ($\mathcal{O}(10 - 10^2$ m) versus $\mathcal{O}(10^3 - 10^4$ m)). Due to its high resolution, this model is able to

resolve the largest turbulent eddies, which makes it very suitable for studying local processes such as convective precipitation. Furthermore, environmental conditions can be prescribed and changed over time. By using time-dependent large-scale atmospheric conditions from the reanalysis data as the basis of LES model runs, we were able to perform sensitivity analyses of large-scale conditions in relation with the precipitation intensity in chapter 4.

1.6 Aim and outline

The obvious impact of convective extreme precipitation on society motivates the need to understand and eventually predict its behavior. With this thesis we investigate physical processes and controlling factors behind extreme precipitation intensities in the present-day and future climate. This is done by looking at local and regional scales, in present-day and future climate, and by making comparisons between atmospheric conditions accompanying mean and extreme intensities. To this end, the following research questions are addressed:

1. *How robust is the observed 2CC scaling between extreme precipitation scaling and (dew point) temperature?*

   Observed relations between the extreme precipitation intensity and (dew point) temperature over the Netherlands indicates an increase of 2CC above $\sim$ 15 K (Lenderink & Meijgaard, 2008). This increase can not be explained solely by thermodynamical arguments. In chapter 2 we analyze sub-hourly observations over the Netherlands to determine the robustness of the aforementioned scaling relation. Using observations we determine the temperature range of this relation, whether the behavior changes for different time intervals, and whether this behavior depends on the percentiles used.

2. *Which local processes are responsible for the 2CC scaling relation?*

   In chapter 2 we use an entraining plume model to determine the dynamical and thermodynamical contributions and identify physical processes involved at the local scale.

3. *How does precipitation depend on atmospheric conditions and large-scale forcing?*

   In chapter 3 we provide an assessment of typical atmospheric conditions and large-scale dynamics for precipitation events of different magnitudes in an event-based setting. The temporal evolution of these conditions are investigated with respect to the time of the peak intensity of each event. Several potential precipitation controlling factors are assessed statistically by means of linear regression, and temporal correlations. This study is performed using a combination of surface observations and a dynamical downscaling of the ERA-Interim reanalysis.

   In chapter 4, the atmospheric conditions and lateral forcing found in chapter 3 for the highest peak intensities are implemented in a large-eddy simulation (LES) model, to simulate precipitation in a convective framework. In this study, the atmospheric stability, relative humidity and large-scale moisture convergence are systematically perturbed to analyze how precipitation depends on atmospheric conditions and lateral forcing.

4. *How are these relations affected by climate change?*

   In chapter 4, the perturbations of the large-scale atmospheric stability, relative humidity and large-scale moisture convergence are repeated for a warmer climate to determine the influence of these conditions on the precipitation response to an increase in temperature.

2

Convective extreme precipitation scaling

Previously observed twice Clausius-Clapeyron (2CC) scaling for extreme precipitation at hourly timescales has led to discussions about its origin. The robustness of this scaling is assessed by analyzing a sub-hourly dataset of 10-minute resolution over the Netherlands. The results confirm the validity of the previously found 2CC scaling for extreme convective precipitation.

Using a simple entraining plume model, an idealized deep convective environmental temperature profile is perturbed to analyze extreme precipitation scaling from a frequently used relation based on the column condensation rate. The plume model simulates a steady precipitation increase that is greater than Clausius-Clapeyron scaling (super-CC scaling). Precipitation intensity increase is shown to be controlled by a flux of moisture through the cloud base, and in-cloud lateral moisture convergence. Decomposition of this scaling relation into a dominant thermodynamic and additional dynamic component, allows for better understanding of the scaling, and demonstrates the importance of vertical velocity in both dynamic and thermodynamic scaling. Furthermore, systematically increasing the environmental stability by adjusting the temperature perturbations from constant to moist adiabatic increase, reveals a dependence of the scaling on the change in environmental stability. As the perturbations become increasingly close to moist adiabatic, the scaling found by the entraining plume model decreases to CC scaling. Thus, atmospheric stability changes, which are expected to be dependent on the latitude, may well play a key role in the behavior of precipitation extremes in the future climate.

This chapter has been published as:

J.M. Loriaux, G. Lenderink, A.P. Siebesma and S.R. de Roode, Understanding convective extreme precipitation scaling using observations and an entraining plume model, *J. Atmos. Sci*, 2013, **70**, 3641–3655

2.1 Introduction

Events of convective extreme precipitation are highly disruptive to society, and are likely to intensify with global warming (Pall et al., 2011; Min et al., 2011). With increasing temperatures, the moisture holding capacity of the atmosphere increases. Therefore, when sufficient moisture is available, precipitation extremes are expected to be thermodynamically related to surface temperature through the Clausius-Clapeyron relation of a ∼6-7 % $^{o}C^{-1}$ increase (Allen & Ingram, 2002; Pall et al., 2007). We will refer to this rate of precipitation increase as CC scaling. However, dynamical processes may influence precipitation intensity leading to deviations from CC scaling (O'Gorman & Schneider, 2009a; Emori & Brown, 2005; Trenberth et al., 2003). With this research we try to assess the behavior of extreme convective precipitation intensity over the Netherlands, and determine which processes are responsible for it.

Observational studies of extreme precipitation scaling for different climatic regions have led to diverging results ranging from decreasing precipitation intensity with temperature (Maeda et al., 2012) to an intensity increase of up to two times CC (2CC) over the Netherlands (Lenderink & Meijgaard, 2008; Lenderink & van Meijgaard, 2010). Scaling exceeding the CC relation (super-CC scaling) followed by leveling off at 15 ^{o}C is observed for convective precipitation by Berg & Haerter (2013). Other studies (Hardwick-Jones et al., 2010b; Utsumi et al., 2011) show CC increase for temperatures up to approximately 25 ^{o}C, after which scaling becomes negative.

There may be several causes for these divergent scaling results, such as different dynamic behavior in different regions, but at least some of the varying results can be attributed to the moisture availability in the area. In moisture deprived areas, the atmospheric moisture content does not necessarily increase with temperature, and the precipitation rate can decrease. Research has shown that using dew point temperature (T_d) rather than temperature leads to more robust scaling results, with more uniform scaling over a larger range of T_d (Lenderink et al., 2011; Lenderink & van Meijgaard, 2010). These dew point temperature studies for the Netherlands (Lenderink et al., 2011; Lenderink & van Meijgaard, 2010) and Hong Kong (Lenderink et al., 2011) consistently show CC scaling in the low T_d-range, with 2CC scaling for dew point temperatures up

to approximately 22 °C (Lenderink et al., 2011). For dew point temperatures beyond this, precipitation scaling displays leveling off behavior.

The 2CC scaling found by Lenderink & Meijgaard (2008) occurred for temperatures above approximately 12 °C, using hourly precipitation extremes in De Bilt, the Netherlands. At lower temperatures CC scaling applied. In correspondence to this article, Haerter & Berg (2009) have argued that the observed 2CC scaling might be a statistical artifact, caused by a shift from stratiform to convective precipitation extremes. Though similar scaling results were found using dew point temperature (Lenderink & van Meijgaard, 2010; Lenderink et al., 2011), the validity of 2CC scaling for convective precipitation has not yet been satisfactory resolved.

In this paper, we assess the validity of 2CC scaling over the Netherlands using daily, hourly, and 10 minute observations, with the aim of resolving whether 2CC scaling applies for convective precipitation. Following Lenderink et al. (2011), this analysis is based on dew point temperature rather than temperature, for more robust results. Though the observational study is based on data from the current climate, the underlying assumption when using this observed scaling in a global warming scenario, is that the relevant parameters behave the same in a future climate as in the current climate. Lenderink et al. (2011) have found good agreement between observed scaling relations and climate predictions. Therefore, in this study we will assume precipitation scaling found from observations to be applicable to a global warming scenario.

Apart from observational analyses, convective precipitation scaling has also been analyzed using general circulation models (GCMs), and non-hydrostatic high resolution models in which convection is resolved, rather than parameterized. Based on a set of GCMs, O'Gorman (2012) finds precipitation increases of approximately 10 % per degree with a 90 % confidence interval of 6-14 % per degree for tropical extremes. Cloud resolving models (CRMs) with different resolutions show lower tropical extreme precipitation increases, consistent with CC scaling (Muller et al., 2011; Romps, 2011).

Using an entraining plume model, we try to reproduce observed precipitation scaling behavior by analyzing a condensation rate scaling relation similar to previously used scaling relations (e.g. O'Gorman & Schneider, 2009a,b; Romps, 2011; Muller et al., 2011). To understand the precipitation scaling better, we

take a closer look at the processes behind it in the plume model, as well as the thermodynamic and dynamic contributions, and in particular the importance of the vertical velocity. Furthermore, we expect that some of the differences in scaling results might be attributed to latitudinal dependencies. While the thermal stratification in the tropics is expected to increase approximately moist adiabatically (e.g. Romps, 2011), this is not clear for midlatitudes (Frierson, 2006; Schneider & O'Gorman, 2008). The influence of environmental changes on the increase of extreme intensities is investigated by perturbing the temperature profile based on moist adiabatic to constant temperature increase.

One of the limitations of the plume model with respect to cloud resolving models, is that environmental conditions are fixed, and are unaware of processes that might affect these conditions, such as convective organization. We recognize the limitations of the plume model, and emphasize that it is used merely as a conceptual tool, for better qualitative understanding of the processes determining precipitation scaling.

Summarizing, this article considers two main research questions;

1. Is 2CC scaling robust for convective extreme precipitation over the Netherlands, or can previously found 2CC scaling results be ascribed to a statistical artifact; and

2. can we increase our conceptual understanding of extreme precipitation scaling using an entraining plume model.

The first question is dealt with in section 2.2, in which the observational setup and results are presented. This is followed by the model description and experimental setup in section 2.3. The second question is treated in sections 2.4 and 2.5. In section 2.4, a precipitation rate scaling relation is introduced, and plume model results are shown. Section 2.5 provides an analysis of thermal stratification changes. Finally, we present an overview of our findings in section 2.6.

2.2 Observations

Previous research on precipitation extremes in the Netherlands has shown 2CC scaling behavior at an hourly resolution for (dew point) temperatures above a certain value (Lenderink & Meijgaard, 2008; Lenderink & van Meijgaard, 2010; Lenderink et al., 2011). At lower temperatures, CC scaling was found. Whether this unexpectedly high 2CC scaling is an intrinsic property of extreme convective precipitation, or transitional behavior between two scaling regimes has been a point of discussion. Both points of view are related to the fact that precipitation events can be of stratiform or convective origin, and that both types have different characteristics. First of all, stratiform events have longer durations and lower intensities than convective events (Berg et al., 2013). Second, convective events generally take place at higher temperatures than stratiform events.

Lenderink & van Meijgaard believe that the 2CC scaling observed at higher temperatures for the hourly analysis is robust for convective extremes, while CC scaling, as found for the daily and lower temperature hourly analyses, indicates extremes of a stratiform origin. They argue that as a result of the typical time scales of stratiform and convective precipitation, at a daily resolution stratiform events dominate the extremes even at high temperatures, while at an hourly resolution, both convective and stratiform events are important. Since stratiform extremes are expected to dominate at lower temperatures than convective extremes, the bifurcation in hourly data between CC and 2CC scaling is interpreted as a stratiform-dominated CC scaling range and a convection-dominated 2CC scaling range.

However, based on the same characteristics Haerter & Berg (2009) have argued that the observed 2CC scaling might be a statistical artifact, induced by the difference in intensities between stratiform and convective extremes. They suggest that stratiform and convective extreme events are both described by CC scaling, with consistently higher intensities for convective events. On an hourly time-scale, precipitation extremes are predominantly stratiform at low temperatures, while at high temperatures convective extremes become dominant. In the transition zone between these two precipitation types, enhanced CC scaling (super-CC) is expected. According to this explanation, the 2CC trend observed by Lenderink & van Meijgaard originates from a transition between stratiform

dominated and convection dominated events.

Both hypotheses concur that the bifurcated scaling found by Lenderink & van Meijgaard for hourly precipitation extremes is somehow caused by a shift from stratiform to convective dominated extremes, but differ on the interpretation of the 2CC scaling. The hypotheses are based on hourly and daily precipitation analyses. Following the same arguments, convective extremes are expected to dominate even at low dew point temperatures when sub-hourly data is used. If a transition zone is present in the sub-hourly data, it is thus expected at low dew point temperatures. Therefore, by analyzing precipitation extremes at sub-hourly resolution, we can clarify whether 2CC scaling is a property of convective extremes, or if it is simply a transitional effect between two CC scaling regimes.

2.2.1 Methods

To examine how scaling of precipitation extremes changes for different time scales, KNMI in situ precipitation data from 27 stations across the Netherlands are analyzed for three different temporal resolutions. The dataset with the highest temporal resolution is a 10-minute data set of precipitation data, with a length of eight years. Due to the amount of stations, this set contains 216 years of data. For consistency hourly and daily datasets are also analyzed. The hourly dataset contains 16 years of precipitation data per station. A set of daily precipitation extremes is obtained by upscaling an hourly dataset by binning into groups of 24 hours. To ensure a large enough data pool, 31 years of data per station are used for this.

For each dataset, only wet intervals are considered. This is determined by a precipitation threshold of 0.1 mm. Since scaling relations are more clear when dew point temperature rather than temperature is used (Lenderink et al., 2011), we will evaluate precipitation intensities with respect to dew point temperature. When analyzing the relation between precipitation intensities and dew point temperature, the dew point temperature used is measured four hours prior to the event, to exclude any T_d-effects induced by the event itself. Results based on daily T_d, T_d two hours prior to the event, or instantaneous T_d are consistent with, but slightly more noisy than the results based on this method (not shown). The daily mean dew point temperature is used for the analysis of daily precipita-

tion intensities. The precipitation data is binned in overlapping 1 degree T_d-bins of 2 degree width.

For each bin, extreme precipitation is analyzed using three different percentiles (the 90th, 99th and 99.9th) in the upper range of the distribution. These percentiles are determined by $pct = 100(n - 1/2)/N$, where N is the sample size of the bin, and n is the index of the sorted distribution vector corresponding to percentile pct. To ensure individual solutions, the distributions need to consist of a minimum of $n = N$ data points. In order to determine the 90th percentile, there must therefore be at least 5 data points, while for the 99.9th percentile a minimum of 500 data points are required. Bins with less than twice this amount of data points are discarded.

2.2.2 Results

Figure 2.1 shows the 90th, 99th and 99.9th percentile of the precipitation intensity distributions with dew point temperature along the x-axis for daily, hourly and 10 minute resolution. Note the logarithmic y-axis, where precipitation intensity is given in millimeters per day, hour and 10 minute intervals for the daily, hourly and 10 minute resolutions, respectively. The dashed lines indicate an exponential 7 % per degree intensity increase, consistent with CC scaling for dew point temperatures close to 12 °C. The dotted lines indicate an exponential 14 % per degree increase of intensity, consistent with 2CC scaling in the same T_d range. The grey shading shows the 95% confidence level determined by means of Monte Carlo, by randomly dropping 10% of the data for each bin for 100 runs.

For all temporal resolutions, the 90th percentile is more noisy, and shows less clear scaling behavior than the higher percentiles. This is especially true for the sub-hourly resolution. It indicates that the scaling relations discussed here are valid only for the most extreme cases, while for less extreme events precipitation is no longer determined by moisture availability alone, leading to deviations from (2)CC scaling. The classification of convective versus stratiform events in this paper is based on the predominance of one type over the other for the highest intensities given a temporal resolution. As we move towards lower percentiles, the scaling is no longer determined by either stratiform or convective events.

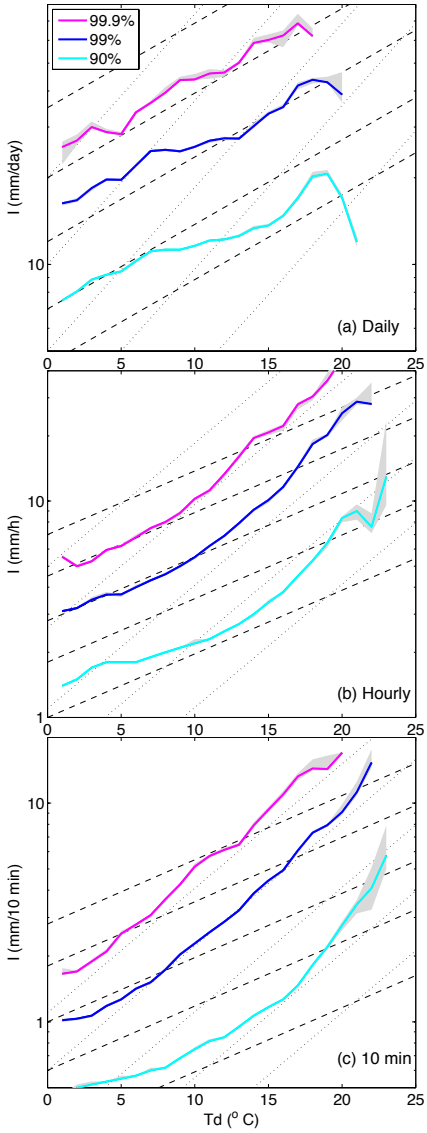

Figure 2.1: Observed precipitation intensity for the 90th, 99th and 99.9th percentile with respect to dew point temperature (T_d) at (a) daily, (b) hourly, and (c) 10 minute resolution. Grey shading indicates the 95% confidence interval. Dashed lines indicate a CC intensity increase, while dotted lines indicate a 2CC increase. Analysis is performed following Lenderink et al. (2011).

Figure 1(a) shows the daily extremes. At this temporal resolution, stratiform extremes are expected to dominate over convective extremes. The plotted percentiles seem to follow CC scaling for all T_d. At an hourly resolution (b) we find a transition from CC scaling at $T_d < 8$ °C to 2CC scaling at higher T_d. These findings are consistent with Lenderink & Meijgaard (2008); Lenderink & van Meijgaard (2010). To determine whether or not the 2CC scaling relation found for hourly extremes is robust or a statistical artifact as proposed by Haerter & Berg, we turn to 10 minute precipitation (c). At this temporal resolution, convective extremes dominate stratiform extremes even at low temperatures. Therefore, if 2CC scaling is indeed caused by a shift from stratiform to convective extremes, the transition zone should be present at lower dew point temperatures than in the hourly analysis, and show CC scaling over most of the domain. However, the 99.9th percentile displays 2CC scaling over the full range of dew point temperatures, as does the 99th percentile for dew point temperatures above approximately 7 °C. This demonstrates that the observed shift in scaling is not caused by a transition between two regimes with CC scaling. Instead, while CC scaling seems applicable for stratiform precipitation, 2CC scaling appears to be an intrinsic property of convective precipitation extremes.

2.3 The entraining plume model

The convective scaling found from observations will be further analyzed using an entraining plume model based on moist static energy and total water content. Due to its simplicity, the model is very useful as a conceptual tool, and therefore lends itself to the purpose of gaining insight in the processes behind precipitation scaling.

The bulk plume model that we use is standard and is identical to many steady state models that form the basis of many moist convection parameterizations in stratiform models (Tiedtke, 1989; Siebesma & Holtslag, 1996). In terms of the dry static energy $s = c_p T + gz$, specific humidity q_v and liquid water q_l, it

can be formulated as

$$w_c \frac{\partial s_c}{\partial z} = L_v c - \epsilon w_c (s_c - s_e), \tag{2.1}$$

$$w_c \frac{\partial q_{v,c}}{\partial z} = -c - \epsilon w_c (q_{v,c} - q_{v,e}), \tag{2.2}$$

$$w_c \frac{\partial q_{l,c}}{\partial z} = c - G - \epsilon w_c q_{l,c}, \tag{2.3}$$

where w_c is the updraft velocity, c the net condensation rate, and G the autoconversion from q_l to precipitable water. In the equations above, subscript c refers to the in-cloud values, while subscript e indicates the environment. The entrainment rate, ϵ can be set to zero for an undiluted plume. For a diluted plume, a value of $\epsilon = \max(0.4/z,\ 10^{-4}\ \mathrm{m}^{-1})$ is used (e.g. Siebesma, 1998; de Rooy & Siebesma, 2008; Holloway & Neelin, 2009). This set of equations can be recombined into equations for moist static energy ($s_{m,c} = s_c + L_v q_{v,c}$), and total water specific humidity ($q_{t,c} = q_{v,c} + q_{l,c}$) in the cloud. These parameters, in combination with pressure, p, describe the thermodynamic state of the atmosphere. The equations for $s_{m,c}$ and $q_{t,c}$ become

$$w_c \frac{\partial s_{m,c}}{\partial z} = -\epsilon w_c (s_{m,c} - s_{m,e}), \tag{2.4}$$

$$w_c \frac{\partial q_{t,c}}{\partial z} = -G - \epsilon w_c (q_{t,c} - q_{t,e}). \tag{2.5}$$

The equations above illustrate how in steady state the advection of $s_{m,c}$ and $q_{t,c}$ is balanced by autoconversion and lateral entrainment. Assuming zero evaporation of rain, the surface precipitation rate P is related to the autoconversion rate through

$$P = \int_{z_b}^{z_t} G \rho dz. \tag{2.6}$$

Here, z_b is the cloud base height; the lifting condensation level (LCL). The cloud top, z_t, is the height at which the vertical velocity becomes zero. Since we are interested in extreme precipitation intensities, we assume that the maximum amount of precipitation that can fall out of an atmospheric column is determined by the total amount of condensation in the column (Iribarne & Godson, 1981),

so that $q_{l,c} = 0$ and $c = G$. This assumption relates the precipitation intensity directly to the condensation rate (2.2).

In the sub-cloud layer, lateral entrainment is assumed to be to zero. Hence, $s_{m,c}$ and $q_{t,c}$ are conserved in the sub-cloud layer below the LCL. Above the LCL $q_{t,c}$ is bounded by $q_{s,c}$ as prescribed by the Clausius-Clapeyron equation [1]. In order to solve these equations, the vertical velocity w_c is computed from buoyancy B and the entrainment, using

$$\frac{1}{2}\frac{\partial w_c^2}{\partial z} = -\alpha_1 \epsilon w_c^2 + \alpha_2 B, \quad \text{with} \quad B = g\frac{T_{v,c} - T_{v,e}}{T_{v,e}}. \tag{2.7}$$

Here, $\alpha_1 = 1$ and $\alpha_2 = 0.6$ are constants (de Roode et al., 2012). The buoyancy is computed from the difference between cloud and environmental virtual temperature T_v and gravitational constant, g.

The model is implemented on a 20 m vertical grid. Equations (2.4), (2.5) and (2.7) are solved in an upward loop using a first order implicit discretization in the vertical. This process continues until the vertical velocity vanishes, and the cloud top is reached.

The environmental profile used is based on a database of soundings taken twice a day between 1995 and september 2011 at De Bilt. From these soundings, ten profiles with the highest undiluted, pseudo-adiabatic convective available potential energy (CAPE) have been combined by taking the mean temperature and relative humidity (RH) at each level, resulting in a typical profile for deep convective circumstances. The temperature and moisture conditions of this idealized profile, as well as the parcel ascent, are shown in figure 2.2. In this figure, the dark blue line indicates the dew point temperature profile, while the temperature is depicted in pink. Skewed black lines are lines of constant temperature, red lines represent dry adiabats, green lines the moist adiabats. The undiluted ascent is depicted by the dashed black line, the diluted ascent by the dashed grey line.

In figure 2.3, the diluted and undiluted profiles of $s_{m,c}$ and $q_{v,c}$ are plotted against the environmental variables. For undiluted ascent, $s_{m,c}$ is conserved,

[1] The Clausius-Clapeyron equation can be written as $de_s/e_s = L_v/R_v dT/T^2$. Here, e_s is the saturation vapor pressure, and L_v and R_v are the latent heat of vaporization and the gas constant, respectively.

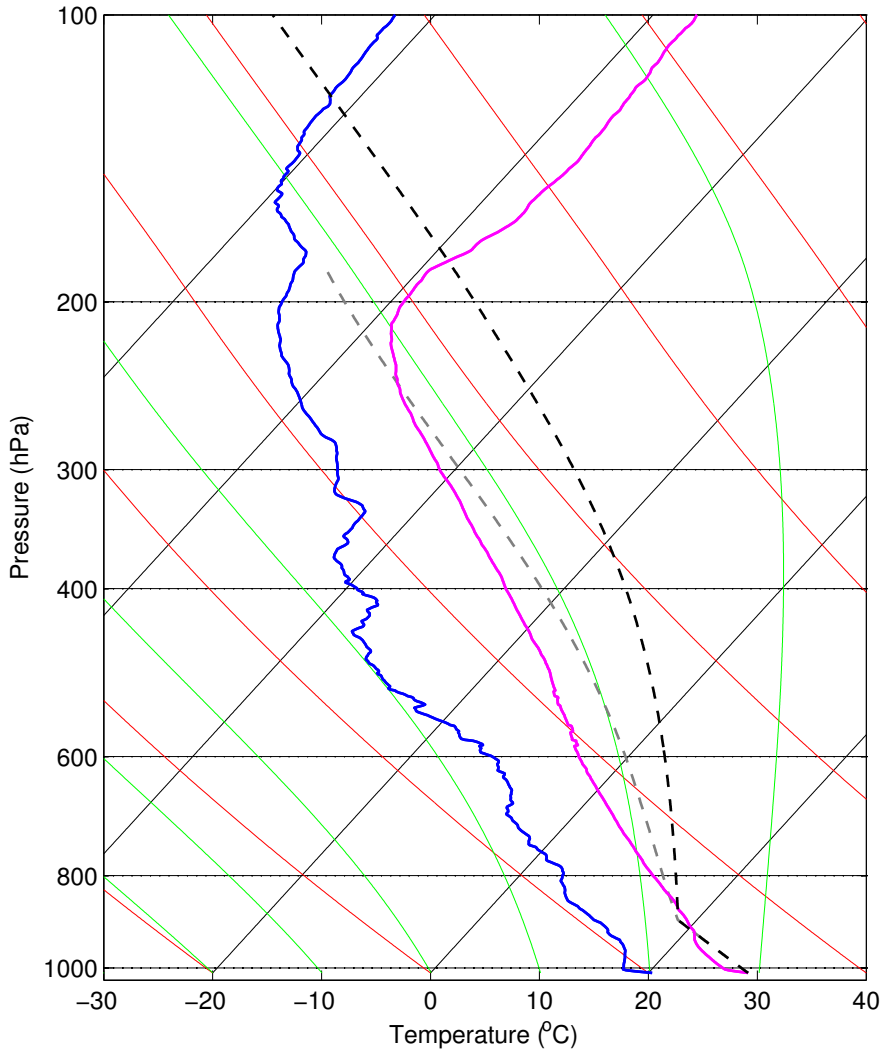

Figure 2.2: Idealized environmental temperature (pink) and dew point temperature (blue) profiles. The updraft profile for diluted and undiluted ascent are shown by the dashed grey and black lines, respectively. Skewed black lines are lines of equal temperature. The red lines indicate dry adiabats, while the green lines give the moist adiabats.

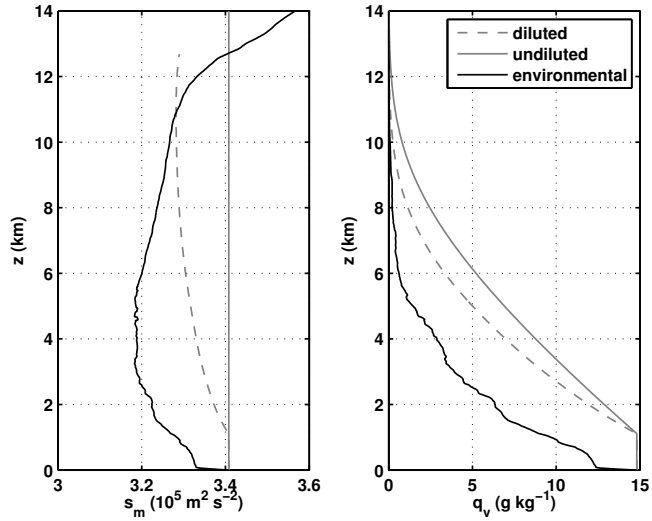

Figure 2.3: Environmental and modeled profiles of moist static energy (left) and specific humidity (right).

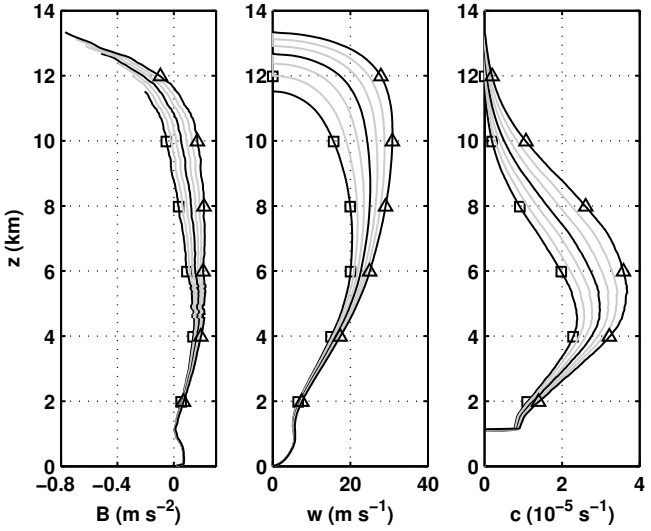

Figure 2.4: Evolution of diluted buoyancy (B), vertical velocity (w) and condensation rate (c) profiles with temperature perturbations of -3°C (black squares) to +3 °C (black triangles) to the environmental profile. The reference profile is depicted by the black line in the middle, while grey lines depict the remaining perturbations between ± 3°C.

since it is not affected by condensation. The diluted updraft profile decreases upon reaching cloud base due to lateral entrainment. The figure shows that for both diluted and undiluted ascent, the updraft profiles are unstable and deep. The $q_{v,c}$ profiles (right) are affected by the condensation rate. The influence of condensation is the difference between $q_{v,c}$ at cloud base and the undiluted $q_{v,c}$, the difference between the diluted and undiluted $q_{v,c}$ shows the influence of entrainment. It is clear that the condensation rate has a larger effect on the profiles than lateral entrainment does.

In order to analyze precipitation scaling behavior, the environmental temperature profile is perturbed by -3 °C to +3 °C in steps of 1 °C. These perturbations occur under the assumption of constant relative humidity (Sherwood et al., 2010), so that at each level for a 1 °C temperature increase, T_d increases following $RH = e_s(T)/e_s(T_d)$. Similar temperature perturbations are carried out in a recent precipitation study by Singleton & Toumi (2013). The sensitivity to stability changes is analyzed in section 2.5.

Figure 2.4 shows diluted parcel profiles of buoyancy, vertical velocity and condensation, for each perturbation. All three parameters increase at all levels for increasing temperature perturbations. The weight of the profiles moves upwards. For example, the maximum condensation rate not only increases, but also shifts towards higher altitudes for increasing temperature.

Perturbed profiles of the saturation specific humidity and its gradient are shown in figure 2.5. The q_s profile decreases exponentially with height. With increasing temperature perturbations the moisture increases at all heights. The saturation specific humidity gradient, $\partial q_s/\partial z$, also becomes stronger with increasing perturbations. Since there is hardly any moisture at higher levels, the moisture gradient is most pronounced at low levels, weakening with height.

Analysis of the changes in the perturbed profiles allows for the scaling of model output with temperature. The scaling of a variable X is written as $\delta X/X$, the fractional rate of change. Here, the numerator gives the difference between the perturbed and reference value. The denominator gives the reference value. Rather than using the initial profile as a reference, we have chosen to use the lowest temperature perturbation (-3 °C) instead, to ensure a continuous scaling range. This has not affected scaling results. Following Hardwick-Jones et al., 2010b, the rate of change per degree is computed from

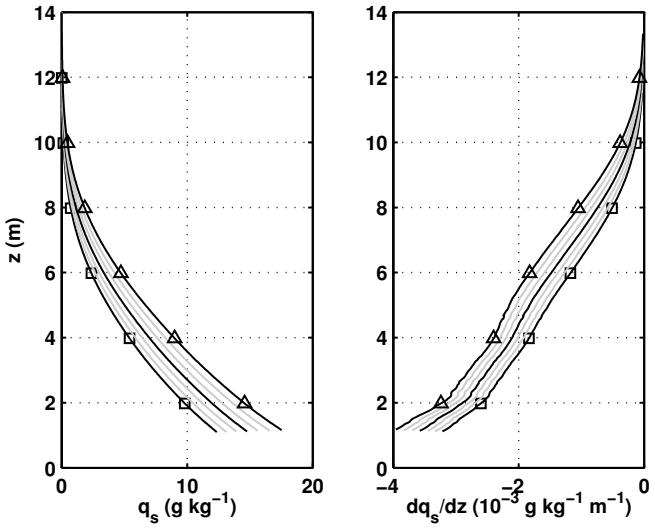

Figure 2.5: Evolution of diluted saturation specific humidity (q_s) and $\partial q_s/\partial z$ with temperature perturbations of -3°C (black squares) to +3 °C (black triangles) to the environmental profile. The reference profile is depicted in black, while the grey lines depict the remaining perturbations between $\pm$ 3°C.

$$\left(\frac{\delta X}{X}+1\right)^{1/\Delta T}-1, \tag{2.8}$$

where we assumed an exponential relation. Here, ΔT is the temperature difference with respect to the reference value.

2.4 Precipitation scaling

In section 2.2 it was shown that 2CC scaling is robust for convective extremes over the Netherlands, which suggests that this behavior is governed by a few basic processes. The aim of the plume model experiment is to analyze the modeled precipitation scaling behavior, in order to assess the consistency with the observations made in section 2.2, and further develop our understanding of this behavior. Since the autoconversion is approximated by the rate of con-

densation, the column integrated precipitation rate P follows directly from the condensation rate;

$$\begin{aligned} P &= [c]\,, \\ &= -\left[w_c\left(\frac{\partial q_{s,c}}{\partial z} + \epsilon(q_{t,c} - q_{t,e})\right)\right], \end{aligned} \tag{2.9}$$

where for simplicity we use $[\ldots] = \int_{z_b}^{z_t} \rho dz$. Here, z_b indicates cloud base height, and z_t the cloud top. The precipitation rate is thus determined from the vertical advection of saturation specific humidity, corrected for entrainment.

To determine precipitation scaling behavior due to temperature perturbations of the initial profile, we take the fractional rate of change of P,

$$\frac{\delta P}{P} = \frac{\delta\left[w_c \frac{\partial q_{s,c}}{\partial z}\right] + \delta\left[w_c \epsilon(q_{t,c} - q_{t,e})\right]}{\left[w_c\left(\frac{\partial q_{s,c}}{\partial z} + \epsilon(q_{t,c} - q_{t,e})\right)\right]}. \tag{2.10}$$

The undiluted form of this equation ($\epsilon = 0$) has been frequently used for extreme precipitation analysis (e.g. Muller et al., 2011; O'Gorman & Schneider, 2009a,b; Romps, 2011). In figure 2.6, the precipitation scaling for diluted and undiluted plumes are shown in blue. Auxiliary lines scaling lines for CC and 2CC scaling are also included. They are computed from surface q_s using T_d, which approximates CC scaling at cloud base, since the parcel rises undiluted from the surface to this height. The fractional rate of change of P shows super-CC scaling slightly below 10 % per degree, and varies little with perturbations, indicating robust scaling behavior. Furthermore, the difference in scaling behavior between diluted and undiluted plumes is small. From this we conclude that the fractional rate of change of P is hardly affected by the environment. For simplicity, we therefore continue the scaling analysis for the undiluted case.

2.4.1 Lateral versus cloud base influence on precipitation

By rewriting (2.9) for $\epsilon = 0$, the two processes responsible for the scaling behavior of P appear;

$$P = w_c \rho q_{s,c}\big|_{z_b} + \int_{z_b}^{z_t} \frac{\partial(\rho w_c)}{\partial z} q_{s,c} dz. \tag{2.11}$$

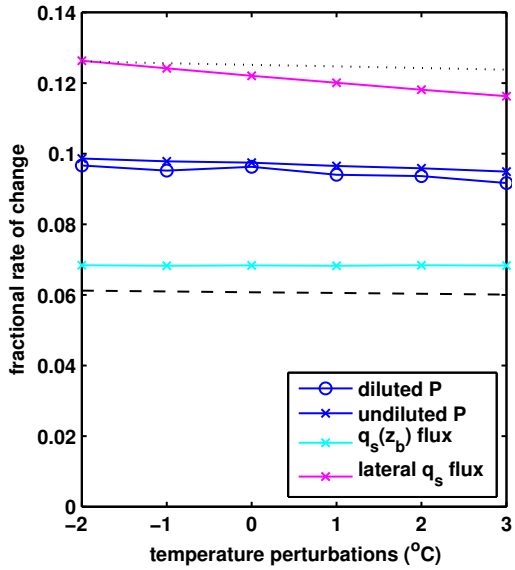

Figure 2.6: The fractional rate of change per °C of diluted and undiluted precipitation rate in blue. Scaling of the undiluted cloud base moisture flux and the integrated lateral moisture convergence are shown in light blue and pink, respectively. For illustration purposes CC (dashed black) and 2CC (dotted black) scaling are also included.

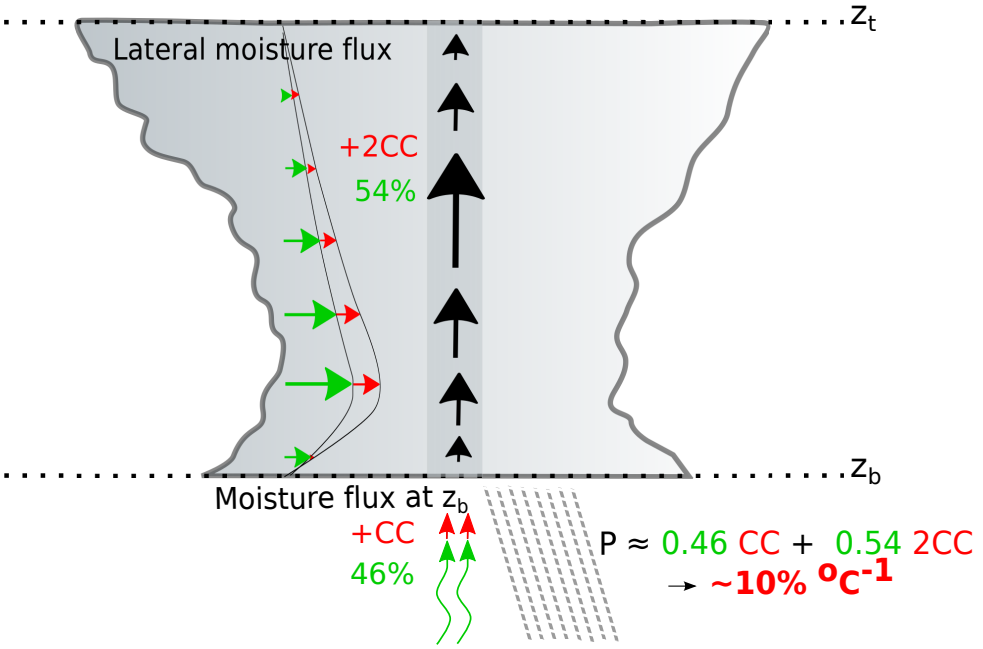

Figure 2.7: Cartoon describing how precipitation intensity scaling as found from the plume model is built up from lateral and cloud base moisture fluxes. Green is used to indicate the initial state, while scaling is depicted in red.

The first rhs term is the moisture flux at cloud base (P_{cb}). The moisture flux at cloud top has been neglected, since vertical velocity is zero at this height, and q_s decreases exponentially with height. The second rhs term gives the column integrated lateral cloud moisture convergence (P_{lm}). So, precipitation rate scaling is determined by the moisture flux at cloud base and the lateral moisture convergence. This is also depicted in figure 2.7. To understand how these processes contribute to the precipitation intensity scaling, we substitute (2.11) into the undiluted form of (2.10),

$$\frac{\delta P}{P} = \frac{\delta P_{cb}}{P} + \frac{\delta P_{lm}}{P}. \tag{2.12}$$

Each rhs term gives the total contribution to the 10 % increase found for precipitation rate scaling. For a better understanding of the behavior of both terms, we rewrite (2.12), so that

$$\frac{\delta P}{P} = \frac{P_{cb}}{P}\frac{\delta P_{cb}}{P_{cb}} + \frac{P_{lm}}{P}\frac{\delta P_{lm}}{P_{lm}}. \tag{2.13}$$

For each rhs term, the first part of the decomposition gives the relative importance of the process to the total precipitation scaling through the initial relative contribution of the process (P_{cb}/P and P_{lm}/P, respectively). The second part of the rhs terms gives the fractional rate of change of the process ($\delta P_{cb}/P_{cb}$ and $\delta P_{lm}/P_{lm}$).

Figure 2.7 shows how these processes contribute to the rate of increase of precipitation intensity. With a relative contribution of 54 %, the lateral moisture convergence has a slightly larger influence on the precipitation scaling than the moisture flux at cloud base (46 %). Both processes are thus of almost equal importance to precipitation scaling behavior. Scaling of the cloud base moisture flux is shown in figure 2.6 (light blue). With an approximate increase of 7 % per degree, it exceeds CC scaling by close to 1 %. Scaling of the lateral moisture flux approaches an increase close to 2CC scaling (figure 2.6, pink). Following (2.13), we can indeed explain the precipitation scaling of 10 % per degree as found from the model by weighing the scaling of both the cloud base and lateral moisture fluxes with their initial magnitude, since

$$\frac{\delta P}{P} \approx 0.46 * 6.7 + 0.54 * 12.5 \approx 10\ \%\ {}^{\circ}\mathrm{C}^{-1}. \tag{2.14}$$

2.4.2 (Thermo)dynamics and the vertical velocity

Assuming changes in density with perturbations to be small, scaling of the cloud base moisture flux can be understood in terms of thermodynamic and dynamic changes. The thermodynamic changes are computed by analyzing temperature and humidity variations using the velocity field from the reference profiles, whereas dynamic changes are computed by analyzing the changes in velocity, while using the temperature and humidity profiles from the reference profile;

$$\delta P_{cb} = \delta P_{cb,th} + \delta P_{cb,d}, \tag{2.15}$$

where $P_{cb,th} = w_c \rho \delta(q_{s,c})|_{z_b}$ and $P_{cb,d} = \delta(w_c) \rho q_{s,c}|_{z_b}$ represent the thermodynamic and dynamic components of P_{cb}, respectively. The thermodynamic scaling contribution equals CC scaling at cloud base, which can be approximated by CC scaling with surface T_d. The vertical velocity at cloud base also increases with increasing temperature perturbations due to increased buoyancy. This accounts for another ~ 1 % per degree scaling, leading to the small exceedance of CC scaling. The results of this decomposition into thermodynamic and dynamic scaling can be found in figure 2.8.

Analogous to the cloud base moisture flux, the integrated lateral moisture convergence scaling is also governed by thermodynamic and dynamic changes, so that

$$\delta P_{lm} = \delta P_{lm,th} + \delta P_{lm,d}, \tag{2.16}$$

with $P_{lm,th} = \int_{z_b}^{z_t} \delta(q_{s,c})\ \partial(\rho w_c)/\partial z\ dz$ the thermodynamic component, and $P_{lm,d} = \int_{z_b}^{z_t} q_{s,c}\ \partial(\rho \delta(w_c))/\partial z\ dz$ the dynamic component of P_{lm}. With an increase close to 8 % per degree, the thermodynamic contribution (first rhs) exceeds CC scaling. Bearing in mind the column integrated nature of the lateral moisture convergence, it is not surprising that the thermodynamic increase lies closer to the increase of column integrated q_s, or water vapor path (WVP) scaling of 9 % per degree, than CC scaling as determined from surface values. The dynamic contribution (second rhs) is positive and accounts for another 5 % per degree of the lateral moisture convergence scaling (figure 2.8).

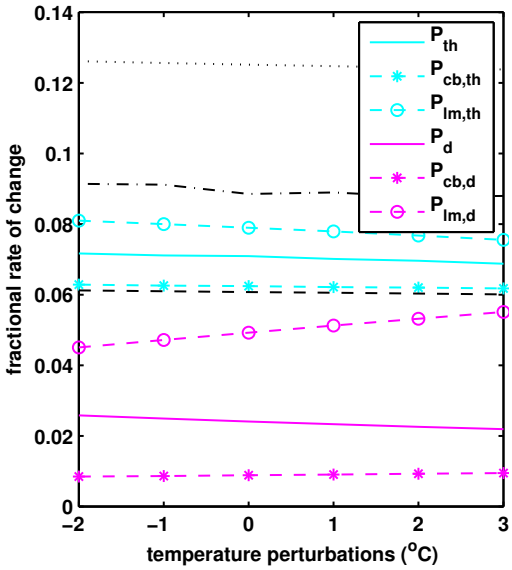

Figure 2.8: The fractional rate of change per °C of the thermodynamic (light blue) and dynamic (pink) scaling contributions, as well as the cloud base and lateral (thermo)dynamic components. For illustration purposes CC (dashed black), WVP(dash-dotted black), and 2CC (dotted black) scaling are also included.

Now that we have an analysis of the thermodynamic and dynamic changes per process, we can also assess the total thermodynamic and dynamic contributions to the precipitation, where

$$\frac{\delta P}{P} = \frac{\delta P_{th}}{P} + \frac{\delta P_d}{P}. \tag{2.17}$$

Here, P_{th} and P_d denote the thermodynamic and dynamic scaling contributions, respectively. Note that the relative contributions of the integrated lateral (54 %) and cloud base (46 %) moisture flux are unchanged for thermodynamical and dynamical decomposition. Therefore, following (2.13), thermodynamic and dynamic contributions become

$$\frac{\delta P_{th}}{P} = \frac{P_{cb}}{P}\frac{\delta P_{cb,th}}{P_{cb}} + \frac{P_{lm}}{P}\frac{\delta P_{lm,th}}{P_{lm}} \tag{2.18}$$

$$\approx 0.54 * 8 + 0.46 * 6 = 7 \text{ \% } ^{\circ}\text{C}^{-1}, \text{ and} \tag{2.19}$$

$$\frac{\delta P_{d}}{P} = \frac{P_{cb}}{P}\frac{\delta P_{cb,d}}{P_{cb}} + \frac{P_{lm}}{P}\frac{\delta P_{lm,d}}{P_{lm}} \tag{2.20}$$

$$\approx 0.54 * 5 + 0.46 * 0.7 = 3 \text{ \% } ^{\circ}\text{C}^{-1}, \tag{2.21}$$

respectively (figure 2.8). This shows that changes in thermodynamics account for most of the scaling, with slight exceedance of surface CC scaling. This exceedance is caused by the column integrated moisture convergence. The super-CC scaling found from the model is mostly caused by the dynamic contribution, which adds an additional 3 % per degree to the precipitation intensity scaling. This signifies the important role of vertical velocity changes in precipitation intensity scaling.

Note however, that apart from the dynamic contribution, the reference vertical velocity profile also determines the relative magnitude of the column integrated and cloud base moisture fluxes. Depending on the shape and magnitude of the vertical velocity profile, the balance between the column integrated moisture convergence and the cloud base moisture flux is determined. Though thermodynamics make up for the largest part of precipitation scaling, this portrays the important role of the vertical velocity in precipitation intensity scaling, not only through the dynamic contribution, but also in determining which process has the largest influence on the scaling.

2.4.3 Robustness of the results

To ensure the robustness of the experiment results, the experiment was performed using several modifications to the deep convective profile regarding the environmental moisture. These profile variations yielded similar results to those discussed in this paper. The experiment was also repeated using the deep convective Weisman & Klemp (1982) profiles. With a precipitation increase of around 9 % per degree, these results are consistent with the results presented in this article. Furthermore, rather than using the assumption that $G = c$, we

also implemented several frequently used autoconversion schemes. Condensation scaling when using Kessler autoconversion (Kessler, 1969), as well as more advanced formulations such as proposed by Sundqvist (1978) with and without ice microphysics, did not significantly alter the results. This puts the results found in this section in stronger footing.

2.5 Scaling sensitivity to environmental stability

In the tropics, the thermal stratification of the atmosphere is dominated by moist convection. There, warming following the moist adiabat appears to be a reasonable approximation (Romps, 2011). However, there is no consensus in literature on the change in thermal stratification for Northern Hemispheric midlatitudes (e.g. Frierson, 2006; Schneider & O'Gorman, 2008). The change in thermal stratification with warming is likely to vary with latitude.

Up to now, we have assumed warming to occur homogeneously with height, so that the temperature perturbation at each height equals the surface temperature perturbation, maintaining the dry stability of the profile. This is not the case for a moist adiabatic perturbation, which leads to stabilization of the profile as the moist adiabatic lapse rate decreases with warming. With this stabilization of the environmental profile, precipitation scaling is expected to be lower than that found in section 2.4. In this section we analyze how the scaling of precipitation intensity is affected by changing stability, and assess whether the choice of perturbing the climate by a constant amount is justified over the Netherlands.

To determine how precipitation intensity scaling changes when the environmental stability increases with warming, we have systematically perturbed the climate with increasing stability from the constant temperature perturbation ($c_0 = 1$) to the moist adiabatic temperature perturbation ($c_0 = 0$), following

$$T'_e = T_e + c_0 \Delta T_0 + (1 - c_0)\Delta T_m. \tag{2.22}$$

Here, T'_e indicates the perturbed environmental temperature profile, which is now described by linear combination of the constant temperature perturbation, ΔT_0, and the moist adiabatic temperature perturbation, ΔT_m, with c_0

a constant, varying from zero to one. For the moist adiabatic temperature perturbation, the environmental temperature is increased by ΔT_m starting at LCL, where ΔT_m is the difference between the moist adiabatic profiles based on the original surface temperature $T_{0,e}$, and the perturbed surface temperature $T_{0,e} + \Delta T_0$. Below the LCL, the temperature perturbation is kept constant at ΔT_0. Figure 2.9 shows the 2 °C temperature perturbations ranging from ΔT_0 to ΔT_m with height, which ranges from 2 °C at the surface, to 6.5 °C at the top of the troposphere, clearly showing the stabilization effect of the moist adiabatic adjustment.

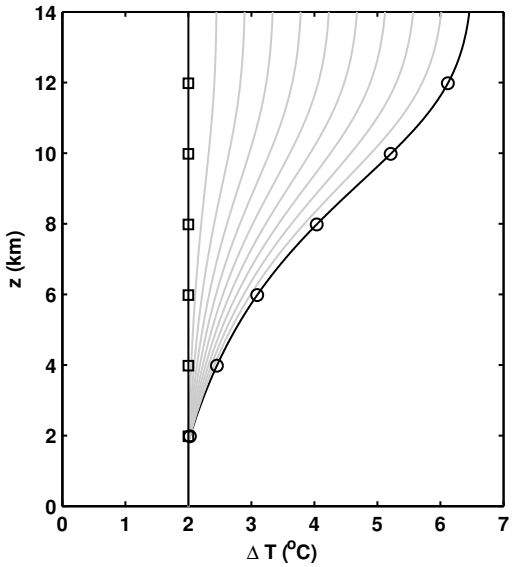

Figure 2.9: Temperature perturbations from $c_0 = 0$ (moist adiabatic, black circles) to $c_0 = 1$ (constant with height, black squares). The perturbations based on a linear combination of these two perturbation types, i.e. for $c_0 = [0, 1]$ are shown in grey.

The change in stability from the moist adiabatic to constant perturbation with height, is visualized in figure 2.10, which shows the phase space of CAPE in the domain of c_0 versus ΔT_0, i.e. the perturbation step versus perturbation type. Since the $c_0 = 0$ perturbation is based on the same adiabats as the parcel,

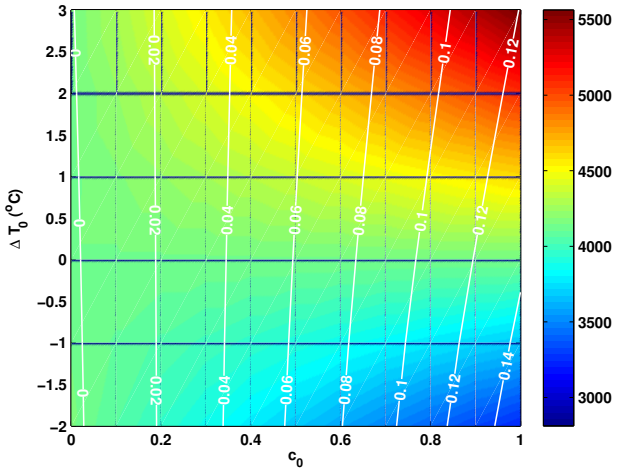

Figure 2.10: The phase space of CAPE (J/kg) as a function of surface perturbation (ΔT_0) and perturbation type (c_0). Here, $c_0 = 0$ represents a purely moist adiabatic perturbation, while $c_0 = 1$ represents a perturbation that is constant with height. The contours of the fractional rate of change of CAPE are overlain in white.

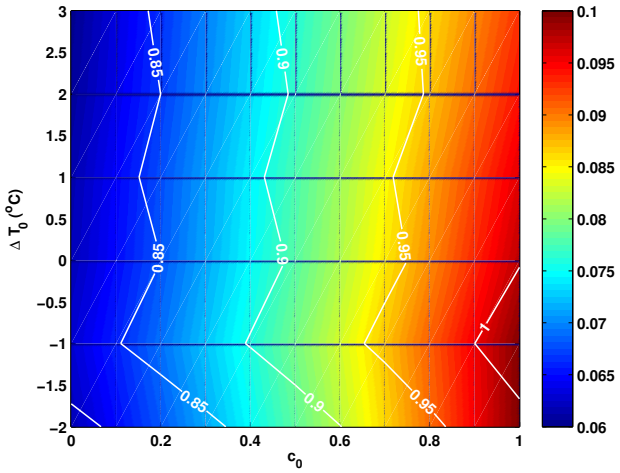

Figure 2.11: The phase space of the precipitation rate scaling per degree for diluted ascent as a function of surface perturbation (ΔT_0) and perturbation type (c_0). Here, $c_0 = 0$ represents a purely moist adiabatic perturbation, while $c_0 = 1$ represents a perturbation that is constant with height. The ratio of the increase in precipitation rate for diluted over undiluted ascent is depicted in white.

CAPE is unaffected by the perturbation step in this case. As c_0 increases, the profile becomes less stable, and CAPE will increase with increasing ΔT_0. This increase becomes more pronounced as the stratification destabilizes. The growth rate of CAPE is also visualized. It shows that the increase in CAPE is more or less unaffected by the perturbation step, and increases from 0 % per °C for $c_0 = 0$, to approximately 14 % per °C for $c_0 = 1$.

Figure 2.11 shows the precipitation intensity increase in the phase space of ΔT_0 versus c_0, where scaling is performed for the entraining plume. The precipitation scaling is fairly constant with perturbation step, in line with figure 2.6. The precipitation rate ranges from ∼6 % per °C for the moist adiabatic adjustment, to just under ∼10 % per °C for the constant temperature perturbation with height. As expected, scaling is lower when profile perturbations show increasing stabilization with height. Interestingly, the scaling for the moist adiabatic perturbation is close to CC scaling, which is in agreement with precipitation scaling in the tropics as found by Muller et al. (2011); Romps (2011). The figure also contains contours of the ratio of precipitation scaling for diluted versus undiluted ascent. Though scaling is more or less unaffected by entrainment for the constant perturbation with height, the difference between diluted and undiluted precipitation scaling increases as perturbations come closer to the moist adiabatic perturbation. These results show that the increase of precipitation rate is strongly influenced by how the temperature is perturbed.

Next, we determine whether the constant temperature perturbation is a reasonable choice for extreme precipitation over the Netherlands. For comparison, we analyze the data of an eight member downscaling with the regional climate model RACMO2 (Meijgaard et al., 2008) at 12 km resolution on a domain over western Europe, which is driven by the global model EC-Earth (Hazeleger et al., 2012). The model configuration of the runs with the global model are identical to those performed for CMIP5 (Taylor et al., 2012) and use the RCP8.5 greenhouse gas scenario. The period 2041-2070 is compared to 1981-2010, during which the global mean temperature rise reaches 2 degrees. Profile data is available at seven points in the Netherlands. Since we are interested in extremes, a further selection is made of the 1000 profiles with the highest CAPE for each summer month (JJA).

Figure 2.12 shows the temperature perturbation for a data selection based

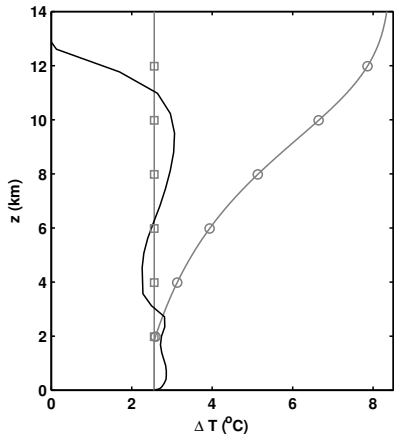

Figure 2.12: RACMO2 temperature perturbation profile, based on the temperature increase of the 1000 profiles with the highest CAPE per month for June, July and August. For reference, the constant (grey squares) and moist adiabatic (grey circles) perturbations corresponding to the surface perturbation temperature of the RACMO2 profile have been added.

on the profiles with the highest CAPE in the summer months. The perturbation profile is fairly constant with height up to ∼750 hPa, decreases by about 0.5 °C to ∼60 hPa, and then increases to close to its surface value at 300 hPa, after which it dies out. Though the perturbation is not constant with height, deflections from the surface perturbation are less than 1 °C, in both positive and negative directions. The use of a perturbation constant in height thus seems reasonable. Furthermore, the increase of CAPE found for (near-) constant temperature perturbations is consistent with CAPE increase found for the output of the RACMO2 climate analysis for the Netherlands. Apparently, the change in stability is well portrayed by this type of perturbation over the Netherlands.

Overall, this analysis has provided important insights in stability changes and precipitation scaling. Comparison with climate run data indicates that a perturbation maintaining the tropospheric thermal stratification is justified over the Netherlands. Furthermore, with super-CC scaling for the perturbation that

is constant with height, and CC scaling for the moist adiabatic perturbation, it is clear that the perturbation intensity increase is dependent on the change in environmental stability.

2.6 Summary and discussion

This paper offers a comprehensive analysis of extreme precipitation intensity increase over the Netherlands. First, a temporal analysis of precipitation data over the Netherlands is used to verify that the previously found 2CC dependency of hourly extreme precipitation on surface moisture is robust for convective events. To understand this dependency, a frequently used scaling based on the column condensation rate is analyzed in depth, by means of an entraining plume model. Scaling analysis shows that the precipitation rate increase is determined by both the integrated lateral moisture flux and the cloud base moisture flux. A decomposition into thermodynamic and dynamic effects further enhances our understanding of how this scaling is affected by different parameters. Finally, a sensitivity study of environmental stability perturbations indicates that precipitation scaling is influenced by how the stability changes with warming.

At an hourly resolution, previous studies have shown bifurcated scaling behavior for extreme precipitation over the Netherlands, with CC scaling for low surface moisture and temperature and 2CC scaling at higher values. Until now, it has remained unclear whether the observed 2CC dependency describes the scaling of convective extremes, or if this behavior is a statistical artifact induced by the transition between the stratiform and convective regimes which both scale with CC. By analyzing extreme scaling with respect to surface moisture at three different temporal resolutions, we have attempted to resolve this. While hourly precipitation extreme scaling is analogous to previous work, CC scaling is found for the daily resolution, where stratiform precipitation dominates the extremes. By analyzing sub-hourly precipitation, convective events are selected from the dataset, leading to a 2CC trend over the entire range of dew point temperatures. This places hourly scaling relations into context, showing that 2CC is not a statistical artifact. We instead confirm that while CC scaling applies for stratiform extremes, 2CC scaling is a robust relation for

convective extreme precipitation in the Netherlands.

Using a basic entraining plume model, we have attempted to reproduce the 2CC dependency based on the scaling of the condensation rate as proposed in previous studies. Though the plume model does not replicate 2CC, it produces a robust, super-CC condensation rate increase just below 10 % $^{o}C^{-1}$. Changes in entrainment only have a minor effect on this. Two processes are responsible for the scaling we find; the integrated lateral moisture convergence, with ∼2CC, and the cloud base moisture flux, which shows an increase slightly greater than CC scaling. With a weight of 54 % versus 46 %, respectively, the lateral moisture convergence and the cloud base moisture flux contribute to the increase of precipitation rate almost equally. These relative contributions are controlled by the unperturbed vertical velocity and specific humidity profiles. Decomposition into thermodynamic (perturbed humidity) and dynamic (perturbed vertical velocity) contributions show that thermodynamic scaling is related to surface CC scaling through the cloud base moisture flux, and WVP scaling through the integrated lateral moisture convergence, leading to a total thermodynamic contribution of ∼7 % per degree. An additional 3 % per degree is provided by the dynamical scaling contribution, based on changes in vertical velocity.

The scaling analysis of precipitation increase illustrates the important role of the vertical velocity. Muller et al. (2011) find a negative dynamical contribution. In their experiment, which uses radiative convective equilibrium, vertical velocity increases in the upper part of the profile, but decreases in the lower part, which has the most weight due to the shape of the humidity gradient. However, in this experiment the dynamic contribution is always positive, simply because of the way w has been defined. Apart from determining dynamic scaling, the vertical velocity also determines the importance of the integrated lateral moisture flux with respect to the cloud base flux. Assuming the dynamic scaling to be unchanged, alterations in w can theoretically lead to scaling results in the range of approximately CC up to 2CC scaling. To understand extreme precipitation scaling, therefore requires a deeper understanding in both shape and evolution of the vertical velocity.

The influence of environmental stability change on extreme intensity scaling is assessed by a sensitivity analysis, where the environmental temperature is increased by a range of moist adiabatic to constant temperature perturbations.

Use of the constant perturbation for the Netherlands is supported by comparison to RACMO2 climate data, while a moist adiabatic perturbation might be more valid for the tropics. Precipitation scaling varies with stability from CC scaling for the moist adiabatic perturbation, to super-CC scaling for the constant temperature perturbation with height. The CC scaling is in line with intensity increase found for CRM studies in the tropics (Romps, 2011; Muller et al., 2011). These results thus imply that there could be a latitudinal effect on the scaling of extreme precipitation, which depends on how the thermal stratification changes with global warming. This is an important point which deserves more attention.

The entraining plume model is obviously a very simple representation of reality. This leads to shortcomings in the dynamical contributions to the rate of change of the precipitation intensity. For example, in nature the dynamics of the sub-cloud layer are coupled to the dynamics of the cloud, as downdrafts generated in the cloud influence the sub-cloud layer. This mechanism is not present in the model, since there is no transfer of information from high to lower levels, as is sometimes done by using a scheme such as CAPE closure. This may have consequences for the dynamical contribution at cloud base. Furthermore, unlike cloud resolving models, the plume model has fixed environmental conditions. Processes that might affect these conditions are not taken into account. While the plume model has provided us with useful insights into the scaling behavior of extreme precipitation, we therefore think that to go further in this analysis, using a model that resolves 3D dynamics is needed.

Acknowledgements

The authors thank Erik van Meijgaard and Jisk Attema for providing us with the RACMO profile data, The authors are grateful to Steef Böing for useful discussions. This study was funded by Knowledge for Climate theme 6.

3

Atmospheric conditions and large-scale forcing

Research on relations between atmospheric conditions and extreme precipitation is important to understand and model present-day climate extremes and assess how precipitation extremes might evolve in a future climate. Here, we present a statistical analysis of the relation between large-scale conditions and hourly precipitation at midlatitudes, by using observations of the Netherlands combined with a regional reanalysis. The aim is to gain a better understanding of the typical large-scale atmospheric conditions and large-scale forcing associated with extreme hourly precipitation, and determine the typical differences between cases of extreme precipitation and weaker events. To avoid double counting, we perform an event based analysis and consider the hourly peak intensity, rather than all hourly data. Atmospheric large-scale profiles consistently show a clear separation between precipitation deciles, characterized by increasing instability and moisture content of the atmosphere for more extreme precipitation. Furthermore, stronger events are characterized by larger atmospheric forcing preceding the event, which primarily relates to vertical motions. Based on these results, four atmospheric parameters, describing atmospheric moisture, stability and large-scale convergence, are analyzed as potential indicators of strong precipitation events. Despite positive relations between these parameters and the peak intensity, their correlations are found to be weak.

This article has been published as:

J.M. Loriaux, G. Lenderink and A.P. Siebesma, Peak precipitation intensity in relation to atmospheric conditions and large-scale forcing at midlatitudes, *J. Geoph.Res.: Atmos*, 2016, **121**, 5471–5487

3.1 Introduction

Due to the high impact extreme precipitation events have on society, numerous studies have been done to assess the response of extreme precipitation to climate change (Westra et al., 2014; O'Gorman, 2015). There is general consensus that climate change will lead to a global increase in frequency and magnitude of extreme precipitation (IPCC, 2014) and observed changes are already being attributed to observed warming (Min et al., 2011; Pall et al., 2011; Lenderink & Attema, 2015).

Various studies describe the atmospheric conditions related to extreme precipitation events at midlatitudes by presenting detailed descriptions of mesoscale dynamics (Houze, 2004), or by describing essential ingredients for extreme events to occur (Doswell et al., 1996). These approaches are valuable, especially in the area of weather prediction, where detailed structures of the atmosphere at the mesoscale need to be considered for accurate forecasting. However, these studies are often based on analysis of a limited number of events or rather short periods (Hand et al., 2004; Ducrocq & Coauthors, 2013), and usually contain qualitative rather than quantitative descriptions. This limits the applicability for research in climate and climate change.

In view of climate and climate change, an important line of research focuses on the sensitivity of precipitation intensity to temperature and moisture. Observational studies of hourly precipitation over midlatitudes show sensitivities from 7% up to 14% per K for local precipitation extremes for a large range of temperatures (Lenderink & Meijgaard, 2008; Lenderink & van Meijgaard, 2010; Berg et al., 2013; Blenkinsop et al., 2015). Whether these observed sensitivities can be used as guide for future changes remains an open question (Westra et al., 2014). They do not necessarily express a direct cause and effect relation, with precipitation responding to the higher moisture content of a warmer atmosphere. Furthermore, Loriaux et al. (2013) demonstrated that changes in atmospheric stability potentially affect the sensitivity results. Thus, observed sensitivities are likely connected to changes in circulation and atmospheric stability. Changes in atmospheric flow conditions are also likely to affect the changes in precipitation extremes in the future climate (O'Gorman & Schneider, 2009a; Emori & Brown, 2005).

At midlatitudes, strong convection tends to occur ahead of synoptic disturbances, where upward vertical motions lead to moistening and destabilization of the atmosphere (Doswell & Bosart, 2001). Studies have tried to connect extreme precipitation to cyclones (Pfahl & Wernli, 2012), and fronts (Catto & Pfahl, 2013). A large amount of 6-hourly precipitation extremes were associated with fronts. Since many precipitation extremes occur under a combination of convective and large-scale precipitation, in this study we will not make an explicit distinction between the different precipitation types.

In order to determine what causes extremes, several studies have focused on the role of CAPE and moisture. For example, Lepore et al. (2015) have analyzed the dependence of CAPE and dew point temperature for extreme precipitation in a climatological study over the US, finding that both parameters are of similar importance. The relations between tropical precipitation and large-scale moisture convergence and atmospheric stability parameters have been studied by Davies et al. (2013). They found a strong relation between precipitation and moisture convergence, but no strong relation between atmospheric stability, such as measured by CAPE, and precipitation intensity. Another tropical study (Dorrestijn et al., 2014) found a strong cross-correlation between large-scale vertical velocity and deep convection.

A study for Europe showed weak correlations of extreme precipitation with CAPE, and stronger correlations with atmospheric moisture (Barkidija & Fuchs, 2013) based on radiosonde soundings, taken from nearby stations. The use of proximity data from radiosonde soundings or relatively low-resolution global reanalysis data is widespread in studies relating extreme events to atmospheric conditions (Dyson et al., 2014; Craven & Brooks, 2004; Allen & Karoly, 2014). However, due to the coarse spatial resolution, these data may not always represent the atmospheric conditions very well.

With this study we aim to catalog the atmospheric conditions and large-scale forcing that accompany precipitation events of increasing intensities in a statistical sense. We will investigate how large-scale advection of moisture influences precipitation intensity, and how these terms evolve over time. The atmospheric conditions are derived from a regional reanalalysis using a downscaling of ERA-interim, which provides high resolution data both in time and space. This data is combined with surface observations, for instance when deriving CAPE. Based

on the combination of surface observations and model output, we furthermore evaluate several controlling factors for extreme precipitation. To this end, we investigate whether the large-scale vertical velocity, and stability parameters correlate well over the Netherlands, since Davies et al., 2013 and Dorrestijn et al., 2014 show a strong correlation between tropical precipitation and vertical velocity, but weak correlations for stability parameters. Furthermore, the water vapor path is evaluated as a potential indicator for extreme events, as this is also an often used sensitivity parameter for tropical precipitation (Bretherton & Peters, 2004; Peters & Neelin, 2006).

To summarize, we aim to realize a better understanding of atmospheric conditions for the precipitating atmosphere at midlatitudes, as well as assess potential indicators for extreme precipitation events at midlatitudes. To this end, we first present the data sets used and the post processing of the data in section 3.2. Section 3.3 contains an analysis of the atmospheric profiles and large-scale forcing, and their temporal evolution. This is followed by a comprehensive survey of potential precipitation indicators in section 3.4. To conclude, in section 3.5 we present a summary of our findings.

3.2 Data and methods

In this study, we try to identify typical midlatitudinal atmospheric conditions for precipitation events and examine the relations between these conditions and precipitation intensity, with an emphasis on the more extreme precipitation events. To this end, we first analyze the environmental profiles of moisture, temperature, and large-scale forcing, followed by an analysis of several potential indicators of extreme precipitation, based on moisture, stability, and convergence. This analysis uses in situ precipitation observations and constrained model results, which are evaluated in an event based setting.

The precipitation data set consists of the Royal Netherlands Meteorological Institute hourly rain gauge data from 1995 to June 28, 2014 (KNMI, 2014). Measurements from 34 automated weather stations (AWS) across the Netherlands are used (figure 3.1), resulting in 5.8 million hours of data, of which $2.4{\cdot}10^5$ hours (i.e. 4%) are wet (> 0.5 mm/h).

The atmospheric profiles and other large-scale atmospheric conditions are determined for the same period, using the high resolution Regional Atmospheric Climate Model (RACMO,Van Meijgaard et al., 2008). RACMO has been used as an interpolator of the ERA interim reanalysis (Dee & Coauthors, 2011) by performing short 36 h forecasts starting from 12 UTC. These forecasts are initialized from ERA interim, and use ERA interim boundary fields. The model forecasts from 12 h to 36 h are used to build a continuous data set of atmospheric conditions. While the atmospheric profiles are comparable with ERA interim, the RACMO output is available at a high resolution (12 km and (sub)hourly), making it more suitable for this purpose. Model output consists of surface data that has been interpolated to all 34 AWS station locations, profile data that has been interpolated to 7 AWS stations spread out across the Netherlands (closed circles in figure 3.1), and several cross sections of the vertical velocity. An overview of the data that has been used can be found in table 3.1.

Table 3.1: Overview of the data used. The locations of the stations can be found in figure 3.1, along with the domain over which the large-scale vertical velocity was calculated.

Source	Variable	Spatial res.	Post processed
AWS	Precipitation intensity	34 stations	34 stations
	Surface T, q_v	34 stations	34 stations
	ω_{LS} (700 hPa)	12 km x 12 km	area mean
RACMO	Profiles (T, q_v, RH, ω)	7 stations	mean profile
	Surface (WVP, T, q_v)	34 stations	34 stations

In section 3.3, we analyze large-scale potential temperature, specific and relative humidity, and vertical velocity profiles as well as the temperature and moisture tendency profiles, by combining hourly mean profiles based on 4 minute snapshots from the 7 locations marked by closed circles in figure 3.1, into one large-scale profile over the Netherlands. Furthermore, in section 3.4 we study several atmospheric parameters that might be relevant as precipitation indicators; the large-scale vertical velocity at 700 hPa (ω_{LS}), convective available

potential energy (CAPE), the water vapor path (WVP), and the K-index. These hourly parameters are obtained from the RACMO output in different ways.

The vertical velocity is a highly fluctuating parameter. In order to get a good estimation of the large-scale vertical velocity, we therefore make use of a cross section of the vertical velocity at 700hPa. This is done by taking a field average of the hourly instantaneous vertical velocity over an area of approximately 50.05° N - 54.5° N by 1.68° E - 8.31° E. This corresponds to the area displayed in figure 3.1 (approximately 450 km x 500 km). Smaller areas were also used but this did not affect the data (not shown). The obtained hourly ω_{LS} is used at all 34 locations corresponding to the AWS stations shown in figure 3.1. Unfortunately, this method can not be extended to the profiles of the vertical velocity, since we only have 3 cross sections. Therefore, the vertical velocity profile used in section 3.3 has been determined by combining the profiles of the 7 station locations instead.

The hourly mean water vapor path based on 4 minute snapshots is available at all 34 locations. At the same locations, hourly snapshot profiles of temperature and specific humidity are used to calculate the K-index and CAPE.

The K-index is originally an indicator for the likelihood of thunderstorms to occur (Charba, 1977). It uses the temperature lapse rate (LTS, first RHS term), lower atmospheric moisture content (LLM, second RHS term) and mid-level relative humidity (MLH, third RHS term) of the atmosphere:

$$K_{IDX} = (T_{850\ \mathrm{hPa}} - T_{500\ \mathrm{hPa}}) + T_{d,\ 850\ \mathrm{hPa}} - (T_{700\ \mathrm{hPa}} - T_{d,\ 700\ \mathrm{hPa}}). \quad (3.1)$$

An alternative method for calculating the K-index was presented by Davies et al. (2013). The alternative K-index uses a mean of (dew point) temperature values at 1000 hPa and 850 hPa, rather than 850 hPa. Both K-indexes have been analyzed and lead to similar results. Since it is more widely used, in this document we will present results for the established K-index.

CAPE is calculated from hourly RACMO temperature and specific humidity profiles at all station locations in figure 3.1, using

$$CAPE = \int_{z_0}^{z_t} g \frac{T_{v,p} - T_{v,e}}{T_{v,e}} \mathrm{d}z, \quad (3.2)$$

which describes the vertical integral of the buoyancy, calculated from the difference between the virtual temperature of the parcel, $T_{v,p}$, and the environment, $T_{v,e}$, along with the gravitational constant, g. Here, the lower bound of the integral, z_0, is the level of free convection, while the upper bound of the integral, z_t, is the height of the equilibrium level, so that CAPE is calculated over the region above cloud base, where the temperature excess is positive. The parcel is released near the surface.

Figure 3.2 shows scatterplots for CAPE calculated from radiosonde data at 12 UTC at station De Bilt (KNMI) against CAPE calculated from the modeled temperature, humidity and pressure profiles from RACMO over the period 1995 to 2012 (left). The modeled CAPE underestimates the CAPE based on radiosonde data. Profile analysis (not shown) suggests that this is primarily due to the underestimation by the model of near surface high moisture conditions that sometimes accompany high CAPE values. To overcome this, we calculated CAPE for RACMO profiles where the parcel profiles were initialized with 2m specific humidity and temperature from the radiosonde (right). It is clear that this greatly improves the results. Apparently, the RACMO profiles beyond the surface layer are very accurate. In this study, we have therefore enhanced the CAPE calculations using RACMO profiles, by initializing the parcel profiles with 2m specific humidity and temperature from the KNMI in situ data set. This data is available at the same temporal resolution and station locations as the precipitation observations.

In order to avoid double counting and scatter in the analysis of the relation between atmospheric conditions and the precipitation strength, we will analyze the data in terms of precipitation events. The strength of the event will be measured by its peak intensity, i.e. the highest measured hourly precipitation intensity during the event. Previous studies (Gaál et al., 2014; Molnar et al., 2015) have proposed a way to organize rain gauge data into events by using a precipitation threshold and a dry interval to separate events. We have applied a similar method. However, the stations used are often located close together. Since one event can pass multiple stations, we have also adding a spatial condition. This way, events that are spaced too closely together are also connected.

This means that precipitation events are formed based on a precipitation threshold, a minimum dry interval (separation time), and a minimum distance

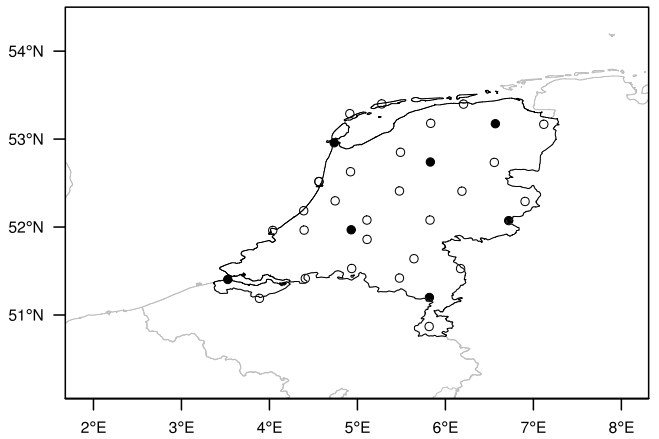

Figure 3.1: Map of the locations of the in situ observations (open and closed circles). The RACMO point data is available at the same locations. The closed circles are locations for which RACMO profile data is available, which will be used in section 3.3. The area of this figure is the area used to calculate large-scale vertical velocity, ω_{LS}.

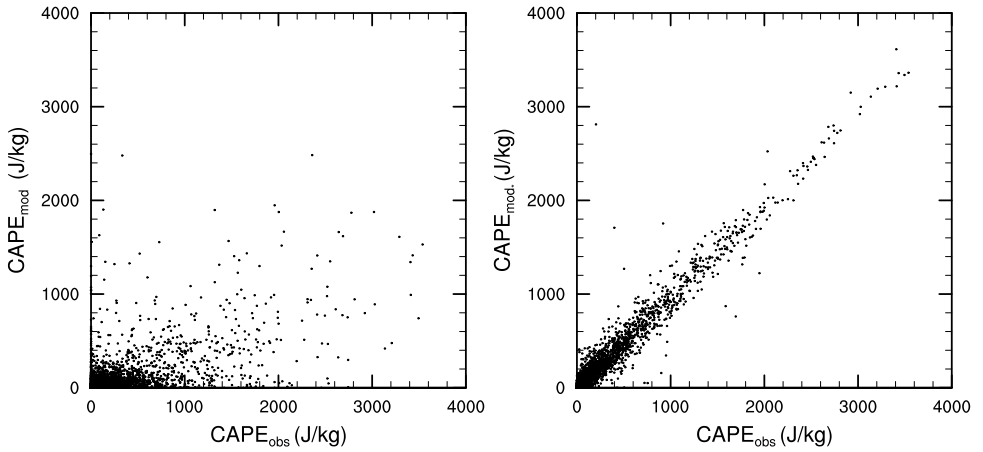

Figure 3.2: Scatterplot of CAPE from soundings versus CAPE calculated for RACMO data (a), and CAPE supplemented with surface temperature and specific humidity from the sounding data.

between events (spatial threshold). We use a precipitation threshold of 0.5mm/h, considering all other data as dry. Following Gaál et al. (2014) and Molnar et al. (2015), a separation time of 2 hours is used. The spatial threshold has been set at 50 km. Increasing this parameter reduces the amount of scatter, but also causes a reduction in the amount of events, while decreasing the spatial threshold leads to an increase of scatter as well as events. Overall, the results aren't greatly affected by adjusting this parameter.

Using a precipitation threshold of 0.5 mm/h, separation time of 2h, and distance of 50 km, we are left with 44,475 separate precipitation events. For each event, we have determined the peak precipitation intensity. The atmospheric data is selected for the corresponding time $\pm$12 hours, and (if applicable) location of the peak intensity.

This is a coarse, but effective method to ensure that extreme intensities belonging to the same event are not double counted. However, sometimes unrelated events can also be connected, and only the highest intensity of this selection will be used in our analysis. As a result, weaker peak intensities are a bit underrepresented in the statistics, and event characteristics such as the duration are not reliable.

For part of our analysis, the event data is grouped into bins separated by deciles of the peak intensity of the event, so that changes in behavior from mild to heavy precipitation events can be seen. Table 3.2 shows the decile bins, along with the mean peak intensity and the intensity range within the bin. In section 3.4, we will look at potential indicators, and it will be useful to zoom in on more extreme events. Therefore, the highest decile has also been split up into percentile bins. With a mean peak intensity of nearly 20 mm/h, the top percentile bin contains the strongest precipitation events.

3.3 Atmospheric forcing and response

We start our examination of the precipitating atmosphere by analyzing the atmospheric conditions and large-scale tendency profiles. Figure 3.3 shows the mean atmospheric profiles of relevant parameters for deciles of the peak precipitation intensity. These profiles are taken 3 hours prior to the peak intensity of

Table 3.2: Peak intensities (mm/h) and their range for each decile bin. There are 4447 data points in each bin. The percentile bins (444 points per bin) are shown below the horizontal line.

Deciles	Decile range	Peak intensity	Intensity range
10%	0% - 10%	0.51	0.5 - 0.6
20%	10% - 20%	0.64	0.6 - 0.7
30%	20% - 30%	0.79	0.7 - 0.9
40%	30% - 40%	0.99	0.9 - 1.1
50%	40% - 50%	1.24	1.1 - 1.4
60%	50% - 60%	1.56	1.4 - 1.8
70%	60% - 70%	1.99	1.8 - 2.3
80%	70% - 80%	2.62	2.3 - 3.0
90%	80% - 90%	3.74	3.0 - 4.7
100%	90% - 100%	8.40	4.7 - 79
Percentiles	Percentile range	Peak intensity	Intensity range
91%	90% - 91%	4.83	4.7 - 5.0
92%	91% - 92%	5.13	5.0 - 5.3
93%	92% - 93%	5.49	5.3 - 5.7
94%	93% - 94%	5.91	5.7 - 6.1
95%	94% - 95%	6.43	6.1 - 6.7
96%	95% - 96%	7.12	6.7 - 7.6
97%	96% - 97%	8.07	7.6 - 8.7
98%	97% - 98%	9.43	8.7 - 10.3
99%	98% - 99%	11.67	10.3 - 13.7
100%	99% - 100%	19.98	13.7 - 79

the event, to minimize event induced effects. They are created by combining hourly profiles from seven station locations in the Netherlands (closed circles in figure 3.1), by means of a spatial average over these 7 stations. The profiles are depicted for precipitation bins, separated by the precipitation deciles (table 3.2), and increase in strength from blue to red.

Figure 3.3 (a) shows the hourly mean potential temperature profile of the

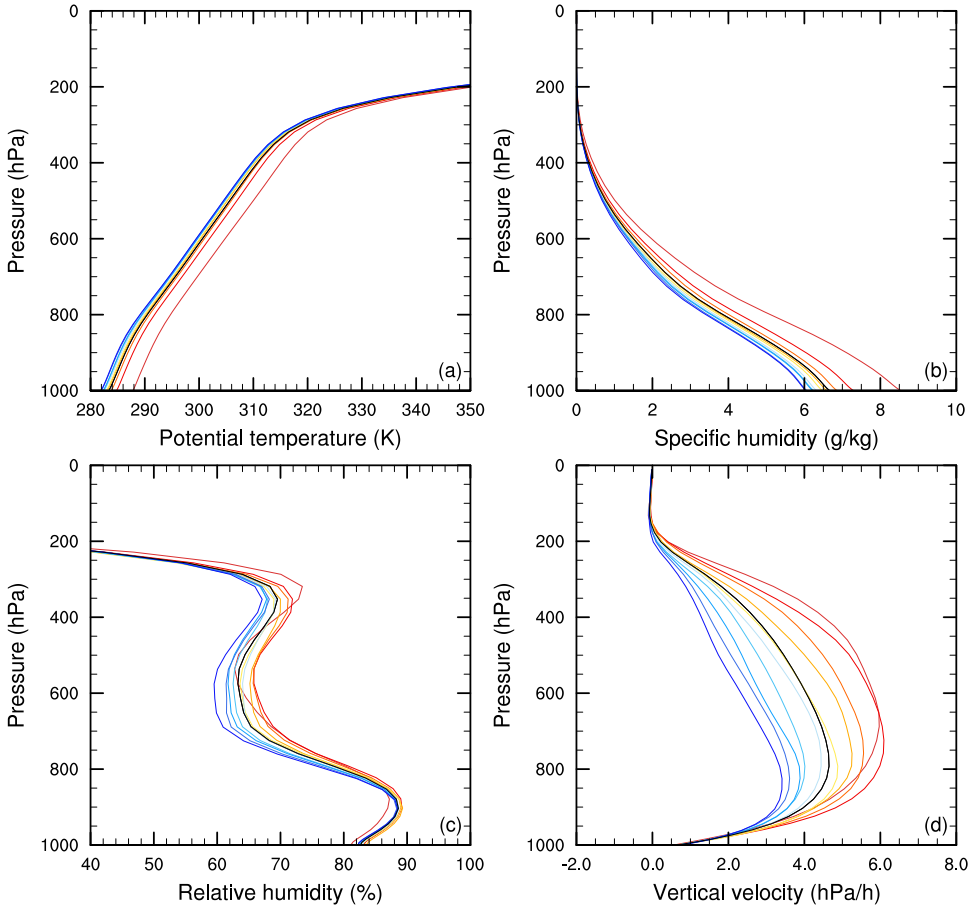

Figure 3.3: Atmospheric profiles of potential temperature (a), specific humidity (b),relative humidity (c) and vertical velocity (d), 3 hours prior to the peak precipitation intensity of the event. The mean profile is shown in black, while the profiles for precipitation deciles are shown from blue (weak precipitation) to red (strong precipitation).

environment. The tropopause is located at around 250 hPa. As expected, an increase in temperature at all levels is observed for increasing precipitation deciles. Figure 3.3 (b) shows the specific humidity, q_v. While q_v increases over the full profile with increasing precipitation deciles, the absolute difference between deciles is largest near the surface. Both the temperature and moisture profiles show the most pronounced increase for the highest precipitation decile bin.

The temperature and moisture profiles are combined in figure 3.3 (c), which shows the relative humidity profiles. Interestingly, while the first through ninth deciles show a steady increase of relative humidity with increasing peak intensity, the highest precipitation decile has a deviating profile. Both surface and mid-tropospheric relative humidity is lower than most of the weaker deciles. This shows that for the most extreme precipitation events, the temperature increase with respect to less extreme deciles dominates over the increase in specific humidity, leading to a lower relative humidity.

Figure 3.3 (d) shows the vertical velocity (ω) which is an indirect measure of the large-scale convergence. Note that we have defined ω positive in the upward direction. All of the decile bins show upward motion, which increases until it peaks somewhere between 850 (weak precipitation) and 700 hPa (strong precipitation), after which the vertical velocity decreases again, approaching zero as the tropopause is reached. Note that the upper decile bin has a slightly different shape than the weaker deciles, which may be an indication of different large-scale dynamics.

Although the order of magnitude of the maximum vertical velocity is quite similar for strong precipitation, these profiles differ from more tropical vertical velocity profiles (Davies et al., 2013). For weaker precipitation we still find upward vertical velocity, while Davies et al. (2013) see downward motion over a large pressure range for most precipitation deciles in the tropics.

Next, we look at the 1 h mean temperature (a-c) and specific humidity tendencies (d-f) in figure 3.4. Apart from the total tendencies, the model provides a decomposition into a dynamical and physical component. The dynamical component gives the tendency contribution due to resolved processes, i.e. horizontal and vertical advection, while the physics component contains the tendencies caused by model parameterizations, such as the radiation, con-

vection and condensation. In figure 3.4, the dynamical (a,d) and physical (b,e) components are shown separately, as well as the sum of both components (c,f).

The dynamical component of the temperature tendency shows cooling up to 400 to 300 hPa (weak, resp. strong precipitation), which destabilizes the temperature profile. This is mostly due to vertical advection (not shown), which means that the dynamical tendency is largely influenced by the vertical velocity profiles shown in figure 3.3 (d). The dynamical temperature tendency is largest for the highest precipitation decile, and peaks at -7 K per day, near 650 hPa. The lower deciles show the same pattern, but with lower values and peaking at lower altitudes. Above the cooling layer, the tendency is positive, peaking on average at 3 K day^{-1} around 200 hPa. This can be explained by the drop in tropopause height as the event approaches. As can be seen from the dynamical moisture tendency profile, the tropospheric cooling is accompanied by a moistening of the troposphere, apart from the boundary layer. Again, this is mainly caused by the vertical advection. Similar to the vertical velocity and dynamical temperature tendency profiles, the signal is strongest for the highest precipitation decile, showing a moistening of 3 g kg^{-1} day^{-1} at 750 hPa. This moistening and cooling of the layer leads to conditions more favorable for convection and condensation.

The physical tendency components show cooling and moistening near the surface, but drying and warming in the rest of the troposphere, indicating possible condensation and condensational heating as a result of the dynamical tendencies. Again we see a clear stratification for the precipitation deciles, with the strongest tendencies (5 K day^{-1}, -2 g kg^{-1} day^{-1}) occurring for the highest precipitation deciles.

The combined dynamical and physical temperature contributions show cooling from the surface up to approximately 300 hPa that is weak and near constant with height for the lowest deciles, but becomes more stratified, and increases to -2 K day^{-1} at 400 hPa for the highest deciles. There is quite a strong warming tendency above 300 hPa, peaking at 3.5 K day^{-1} since the dynamical contribution is not compensated by a strong physical cooling component. The combined moisture tendency shows moistening of the atmospheric profile up to approximately 600 hPa, which increases with increasing precipitation deciles. At higher levels, the physical and dynamical contributions approximately cancel

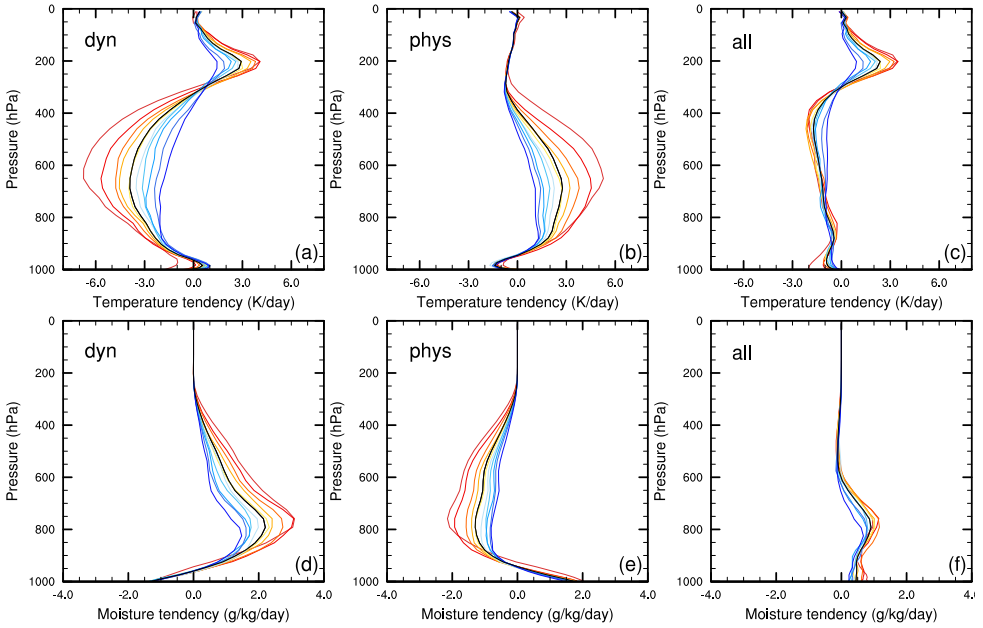

Figure 3.4: Atmospheric tendency profiles of temperature (a-c) and specific humidity (d-f) 3 hours prior to the peak precipitation intensity of the event. The dynamical (a,d) and physical contributions (b,e) are followed by the total tendency profiles in figures (c) and (f). Colors as described in figure 3.3.

each other out. For both moisture and temperature tendencies, the dynamical contribution appears to dominate over the physical contribution, and tendencies are stronger for the highest precipitation deciles. However, the combined moisture and temperature tendencies are both much weaker than the separate dynamical and physical components. Though the separation into dynamical and physical tendency components is not exactly the same as a separation into large-scale and convective tendency components, it is interesting to note the parallel with the work of Zhang (2002, 2003), suggesting that the atmosphere is close to convective quasi-equilibrium.

To get a better idea of the changing atmospheric state and the timing of separate tendency contributions, we also look at the temporal evolution of these terms. Since the vertical velocity and tendency profiles all peak between 650 and 750 hPa, we have chosen to analyze the temporal evolution of the profiles

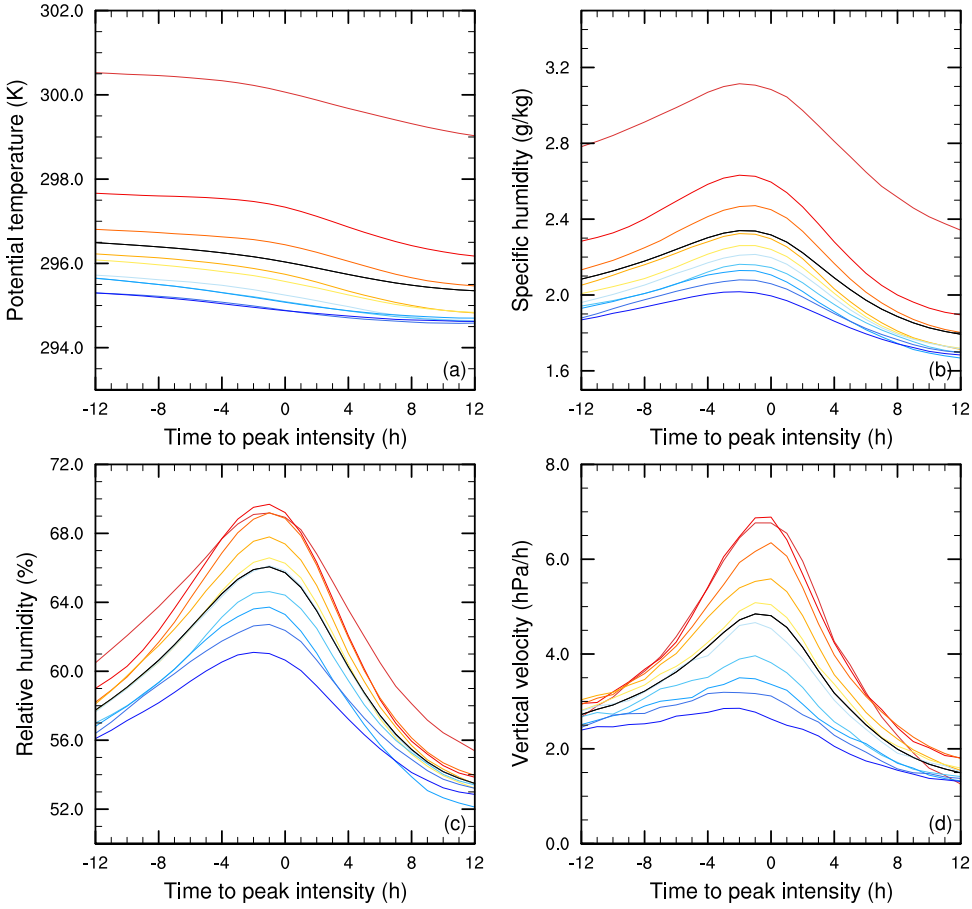

Figure 3.5: Temporal evolution of the atmospheric profiles of potential temperature (a), specific humidity (b),relative humidity (c) and vertical velocity (d) at 700 hPa, from 12 hours prior to 12 hours after the time of the peak intensity of the event. Colors as described in figure 3.3.

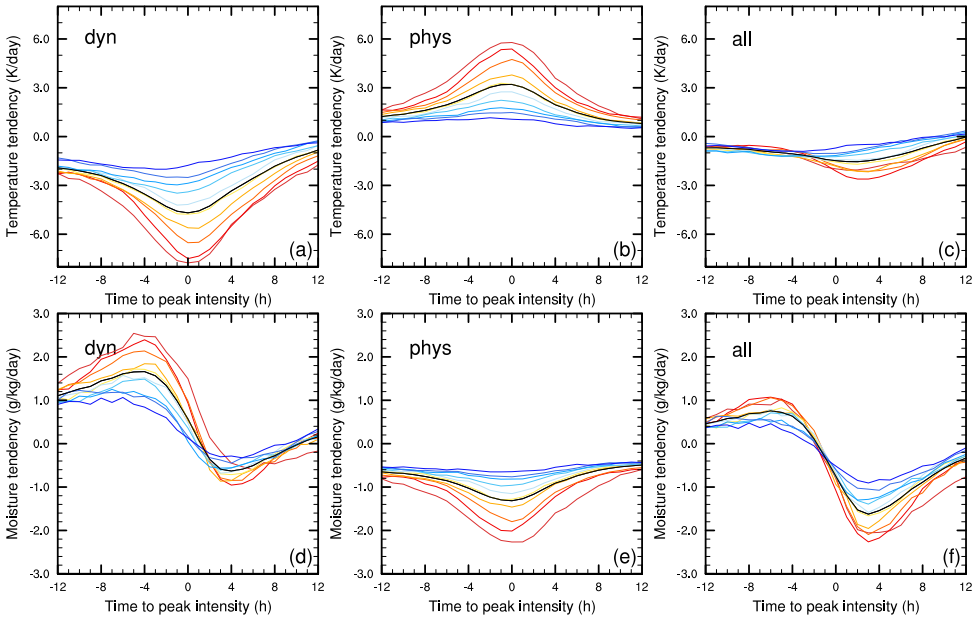

Figure 3.6: Temporal evolution of the atmospheric temperature (a-c) and specific humidity (d-f) tendencies at 700 hPa from 12 hours prior to 12 hours after the time of the peak intensity of the event. The dynamical (a,d) and physical contributions (b,e) are followed by the total tendency profiles in figures (c) and (f). Colors as described in figure 3.3.

at 700 hPa (figures 3.5 and 3.6).

Figure 3.5 shows the temporal evolution of the atmospheric profiles of figure 3.3 from 12 hours before to 12 hours after the peak intensity. The potential temperature (a) shows cooling of approximately 0.5 to 1.5 K per day for weak to strong precipitation deciles, respectively. During the full period, the temperature tends to be higher for the higher precipitation deciles. The temporal evolution of the specific humidity (b) shows the strongest pre-event moistening for the highest precipitation deciles. For lower deciles the temporal signal is much weaker. After the peak intensity is reached, the specific humidity decreases to values below the initial specific humidity for each decile bin. Figure 3.5 (c) shows the temporal evolution of the relative humidity. At 700 hPa, the highest precipitation decile does not yet show the decrease in relative humidity with respect to the lower precipitation deciles seen in figure 3.3 (c). Therefore, the temporal evolution does not show a clear deviation between the highest decile and the other deciles. The relative humidity simply increases as the event approaches, after which the relative humidity decreases to below starting values. The vertical velocity (d) has a strong stratification, with weak temporal variations for the lowest precipitation deciles, but a very clear increase leading up to the time of the peak intensity, after which the vertical velocity rapidly decreases to approximately 2 hPa/h, which is slightly lower than the starting value. To summarize, at 700 hPa, weak and strong precipitation events all lead to cooling of the layer, with moistening and an increase in vertical velocity leading up to the event, followed by drying and a decrease in large-scale vertical velocity. Eventually the atmosphere is left in a colder, drier state, with weaker large-scale convergence. These effects are most pronounced in the highest deciles.

Next, we look at the temporal evolution of the temperature and moisture tendencies (figure 3.6). The dynamical (a) and physical (b) temperature tendency components both show the strongest temporal signal for the highest precipitation deciles. Prior to the event, there is cooling due to vertical advection which increases as the event approaches (a). Simultaneously, the physical component of the temperature tendency (b) increases as well, indicating convection and condensational heating are already taking place, compensating for the destabilizing cold air advection. There is no time-lag between the physical

and dynamical components, and the total temperature tendency is fairly constant and shows little stratification up to 3 hours before the peak intensity of the event. After that, the highest precipitation deciles show a net cooling which increases up to approximately 3 hours after the peak intensity and decreases until the temperature tendency almost vanishes. This is in line with our earlier observation that the system is close to quasi-equilibrium, even for the highest precipitation deciles.

The moisture tendencies (d-f) also show the strongest temporal signals for the highest precipitation deciles. The dynamical component (d) clearly shows advection of moist air, which peaks 4 hours before the height of the event. The physical component of the moisture tendency (e) lags behind, peaking at the time of the event. This time lag indicates that the moistening precedes the condensation, which unsurprisingly peaks at the time of the peak intensity. The combined effect (f) is a moistening of the layer due to advection of moist air, which is followed by drying of the layer, due to the event itself.

3.4 Precipitation indicators

The clear stratifications and temporal signals seen for the profiles discussed in section 3.3 indicate interaction between precipitation and vertical velocity, moisture and stability. Therefore, we next look at a few relevant parameters, and evaluate their potential role as indicators for extreme precipitation.

Over the tropics, the large-scale vertical velocity correlates well with deep convection (Dorrestijn et al., 2014), and large-scale moisture convergence relates well with tropical total precipitation (Davies et al., 2013). We will therefore continue the analysis of the vertical velocity in this section to determine its potential as an indicator for heavy precipitation over midlatitudes. In the previous section, we already analyzed the vertical velocity profile and its temporal evolution at 700 hPa, based on 7 locations and observed a clear decile stratification of this parameter. As the vertical velocity is a highly fluctuating parameter, we will use the 700 hPa field mean vertical velocity, ω_{LS}, rather than the profile cross-section used before.

A highly unstable atmosphere leads to vigorous convection, which can result in strong precipitation intensities. This can also be seen in the dynamical temperature tendency profile in figure 3.4 (a), which shows the strongest destabilization of the atmosphere for the highest precipitation decile. Using an entraining plume model, Loriaux et al. (2013) have shown that the sensitivity of precipitation intensity to temperature increases with atmospheric instability. Here, we investigate if the atmospheric stability itself is a good indicator of extreme precipitation by examining the relation between CAPE, and peak precipitation intensity.

The systematic intensification of the moisture tendency profiles with increasing precipitation deciles confirms that there is also a relation between atmospheric moisture and the precipitation intensity. Furthermore, tropical precipitation intensities exhibit critical behavior in relation to the water vapor path (Peters & Neelin, 2006). Therefore, we will also evaluate the water vapor path (WVP).

Lastly, we will consider the K-index, a parameter which incorporates both stability and moisture, to determine if a combined effect leads to a better precipitation indicator. The K-index is originally an indicator for the likelihood of thunderstorms to occur, and is based on the temperature lapse rate and atmospheric moisture components, as was shown in eq. (3.1). The highest K-index values are reached when the atmosphere is moist and unstable with high low-level moisture. Therefore, we expect to find a positive relationship between the K-index and precipitation intensity. An advantage of this parameter, is that it isn't affected by the surface conditions as much as CAPE is. Therefore, the K-index is more robust in space and time.

We will first consider the temporal evolution of the parameters separated into groups based on precipitation intensity, as was done in section 3.3. Next we analyze the relation between the peak intensity and the atmospheric parameters directly. This will illustrate which precipitation intensity is most observed for a certain value of the atmospheric parameter, rather than separating the atmospheric parameter into precipitation deciles. Finally, a lag correlation analysis is done to determine how peak precipitation responds to the parameters, and at what time the correlation is highest.

3.4.1 Average temporal evolution

Unsurprisingly, the temporal evolution of the large-scale vertical velocity (figure 3.7 (a)) compares well with our first approximation based on the vertical velocity profile (figure 3.5 (d)), albeit with slight differences. Note that the top decile has been split up into percentile bins (dashed) to emphasize the extreme intensities. The vertical velocity peaks a few hours before the maximum intensity of the event, and drops to approximately 1 hPa/h for all percentiles, which is weaker than the starting value of approximately 2.5 hPa/h. This peak in ω_{LS} is not seen for the weakest deciles. Furthermore, the separation into percentiles shows that there is hardly any difference in the temporal signal of the vertical velocity for events in the eightieth percentile or higher. Apparently, ω_{LS} levels off for the highest precipitation intensities.

The temporal evolution of CAPE is shown in figure 3.7 (b) for deciles (solid) and the top ten percentiles (dashed) of peak precipitation intensity. The lowest deciles hardly show a signal, but for the highest intensities, there is a strong increase in CAPE leading up to a few hours before the height of the event, after which CAPE drops drastically at the time of the peak intensity. This signal increases for increasing precipitation percentiles. It indicates a strong destabilization of the atmosphere leading up tot the heavy precipitation events, after which CAPE is quickly reduced due to surface cooling and consumption by the event. At the time of the peak intensity, CAPE has reached its minimum value, and CAPE is slightly restored and remains steady at low values.

The temporal evolution of the water vapor path (figure 3.7 (c)) shows a modest increase in the water vapor path leading up to the peak intensity, which is most clear for the highest percentiles. As the water vapor is condensed and precipitated out, the atmosphere becomes slightly drier than it was 12 hours before the peak intensity. The water vapor path shows hardly any distinction between the lowest deciles, but the spread increases for the highest deciles. The top 10 percentiles show a very strong increase of WVP with increasing intensity.

Figure 3.7 (d) shows the temporal evolution of the K-index from 12 hours before, to 12 hours after the maximum precipitation intensity is reached. The spread of increasing K-index for increasing precipitation intensity deciles is very clear for the top 20% of the peak intensities in this figure. There is also a clear

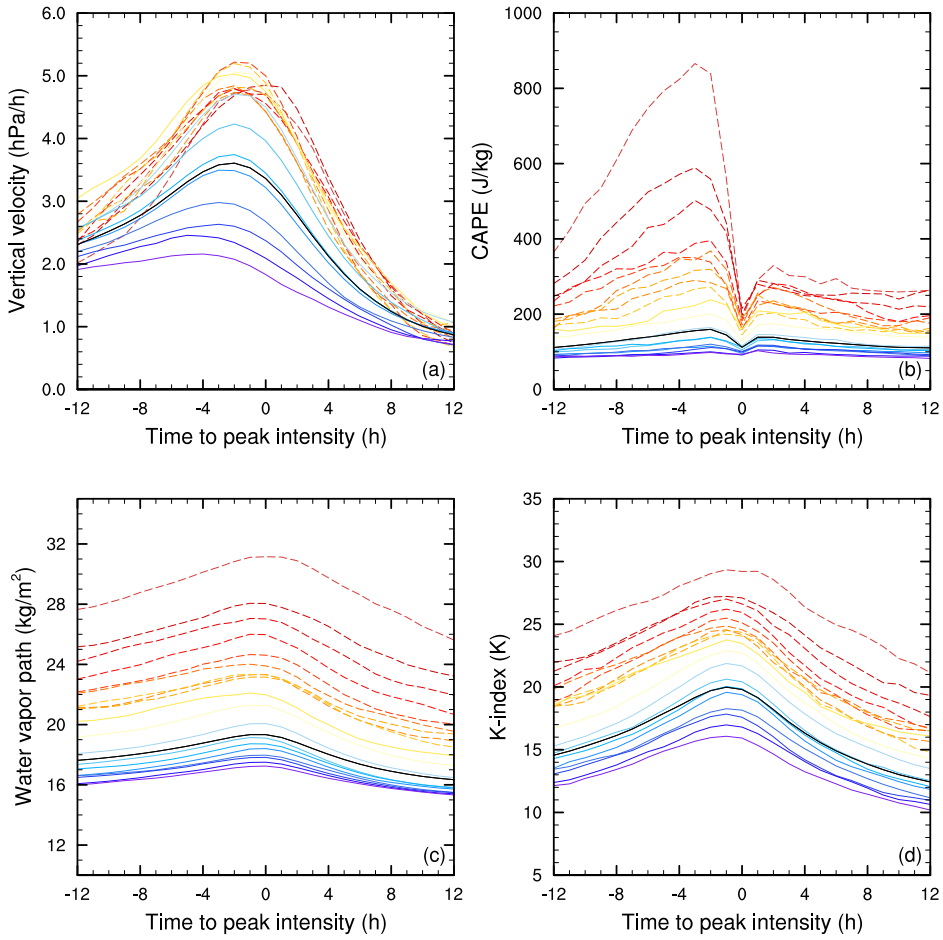

Figure 3.7: Temporal evolution of large-scale vertical velocity (a), CAPE (b), WVP (c) and K-index (d), from 12 hours prior to 12 hours after the time of the peak intensity of the event. The mean profile is shown in black, while the profiles for increasing precipitation bins are shown from blue (weak precipitation) to red (strong precipitation). The solid lines are decile bins. The highest decile bin has been split up into percentile bins (dashed lines).

temporal signal, where the K-index increases up to an hour before the event peaks, and decreases afterwards to a slightly lower value than it started off with.

3.4.2 Distributions

The distributions of the atmospheric parameters discussed in this section and the relations between the peak intensity and these parameters, are shown in figure 3.8. Again, the atmospheric parameters are taken at a 3 hour lead with respect to the peak intensity, to keep event induced effects to a minimum. The data is evaluated for 25 bins of equal sample size of the atmospheric parameter. The black solid line in the top panel of each atmospheric parameter shows the mean relation with the peak intensity. The shaded area indicates the range of the 10th to 90th precipitation percentile, and the binned 99th percentile is shown by the dashed line. The bottom panel of each parameter shows the distribution of the frequency of occurrence of the parameter values. A good precipitation indicator will show a positive (or negative) relation with peak intensity, with hardly any difference between the different precipitation percentiles and the mean.

The relation between ω_{LS} and the peak intensity is shown in figure 3.8 (a). The bin averaged peak intensity increases from 1.5 to 3.5 mm/h with increasing large-scale vertical velocity (solid). The 99th percentile increases from approximately 10 to 20 mm/h over the same range of vertical velocity. While most of the data is concentrated around weak ω_{LS} values, there is plenty of data where the vertical velocity exceeds 5 hPa. This means that the leveling off seen in figure 3.7 (a) for precipitation percentiles, is not due to a physical limit. Instead, it results from the high concentration of data around low ω_{LS} values, in combination with the weak increase in the peak intensity with ω_{LS}. As a consequence, even the heaviest precipitation percentiles will contain a relatively large amount of weak ω_{LS} values, leading to the observed leveling off when we look at the percentile spread in figure 3.7 (a).

The peak intensity shows a stronger increase with CAPE (b), from 2 to 10 mm/h. The spread, and the 99th percentile also increase with increasing CAPE, indicating that an increase in CAPE leads to a large range of precipitation intensities, both high and low. This may have to do with the fact that CAPE is a

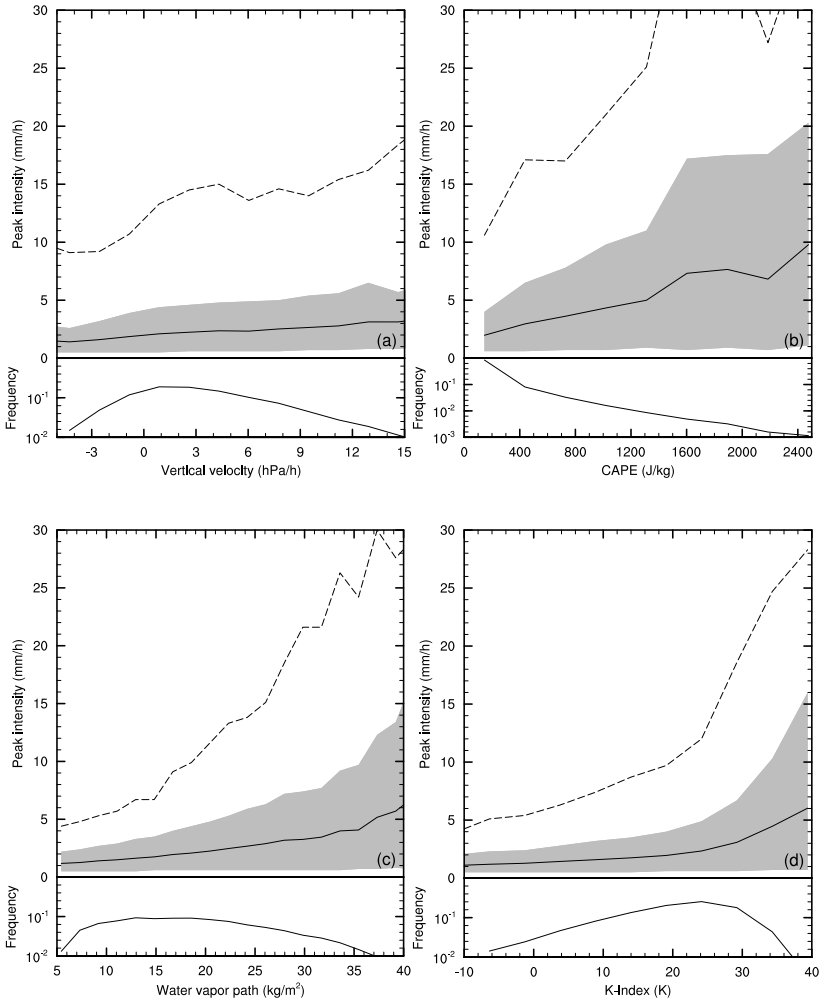

Figure 3.8: The top panel of (a) shows the mean vertical velocity 3 hours prior to peak intensity versus peak intensity based on 25 of equal sample sizes ω_{LS} bins (solid). The grey shading gives the range from p10 to p90. The dashed line is p99. The bottom panel gives the frequency distribution of the vertical velocity. The same is shown for CAPE (b), WVP (c), and the K-index (d).

potential that does not have to be consumed, increasing the amount of scatter in the relation between CAPE and peak precipitation. However, removing data with a high convective inhibition (CIN) from the data set has not lead to significant changes in the results (not shown). Most of the data is concentrated around low CAPE values.

Figure 3.8 (c) shows the relation between the water vapor path and peak intensity. The slope of the peak intensity versus the water vapor path increases with increasing water vapor path but does not show the same characteristic critical behavior as can be seen in e.g. Peters & Neelin (2006). However, this may be due to the fact that the water vapor path does not reach the tropical WVP values at which they observe critical behavior. The peak intensity clearly increases with increasing WVP, from 1 to 6 mm/h in the mean, and from 4 to 29 mm/h for the 99th percentile. This, in combination with a reasonably uniform frequency distribution, explains the increase in stratification with increasing deciles of peak precipitation in figure 3.7 (c); The highest precipitation deciles only contain a small range of WVP values, while the lower deciles all contain a large range of WVP values, causing the difference between each weakening decile to decrease. Furthermore, the increasing spread of the peak intensity shows that while low water vapor paths hardly ever result in heavy precipitation, a high water vapor path can lead to a large range of precipitation intensities.

Finally, the relation between the K-index and the peak intensity is shown in figure 3.8 (d). While for low K-index values there is hardly any relation with the peak intensity, the peak intensity starts to rapidly increase for K-index values beyond roughly 20 K. However, the range between the 10th and 90th percentile also increases for the K-index above 20 K, so that again, a high K-index does not necessarily have to lead to high precipitation intensities.

3.4.3 Lag correlation

So far, we have found clear stratification in the precipitation deciles and percentiles of the atmospheric parameters shown in figure 3.7. Furthermore, the peak intensity is positively related to all atmospheric parameters (figure 3.8). However, the latter figure also shows a large amount of scatter in these relations, as shown for instance by the broad grey shading between the 10th and

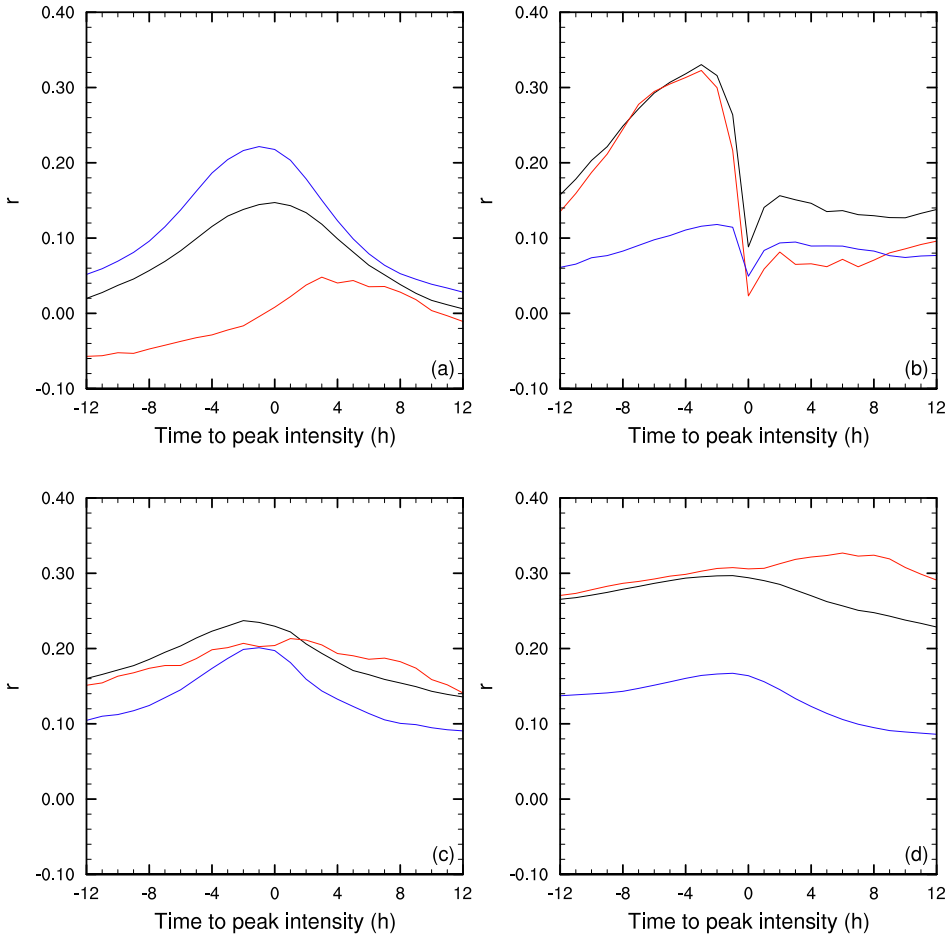

Figure 3.9: Lag correlations between peak intensity and vertical velocity (a), CAPE (b), water vapor path (c) and the K-index (d). The correlation of the whole peak intensity distribution is shown in black. The high intensities (90-100%) are shown in red, and the weak to moderate intensities in blue.

90th percentiles. Figure 3.9 (black lines) shows the lag correlations between ω_{LS} (a), CAPE (b), WVP (c) and the K-index, and the peak intensity, which enables us to see how the correlation between these parameters and the peak intensity changes in time. The values of the maximum correlations can be found in table 3.3.

Table 3.3: Maximum cross-correlations with the peak intensity, and the time at which the maximum cross-correlation is reached. The decomposition of the K-index is shown below the horizontal line.

Variable:	Cross-correlation:	time:
Vertical velocity	0.15	0 h
CAPE	0.33	-3 h
WVP	0.30	-1 h
K-index	0.24	-2 h
LTS	0.10	-1 h
LLM	0.28	-1 h
MLH	0.08	+1 h

The CAPE correlation pattern is similar to the temporal evolution seen in figure 3.7 (b). At t = -3 h a maximum correlation of 0.33 is reached, after which it drops drastically. As expected from figure 3.7 (b), the correlation reaches its minimum value at t = 0 h. The correlation between CAPE and the peak intensity is the highest of all parameters, despite the large amount of scatter seen in figure 3.8 (b). It seems that high CAPE does increase the chance of an extreme event occurring in the next couple of hours, but the relation is not strong enough for CAPE alone to be a good indicator for extreme precipitation. While extreme events are usually preceded by high CAPE values, high CAPE conditions do not necessarily lead to strong precipitation.

The correlation between the water vapor path and the peak intensity has a weaker temporal signal, increasing from 0.26 to 0.30 at t = -1 h, after which the correlation gradually decreases to 0.22 at t = +12 h. The fact that the correlation is not influenced much by the timing of the event, shows that this is

more of a climatological correlation; the precipitation intensity is stronger when the atmosphere contains more moisture.

The K-index correlation with the peak intensity increases from 0.16 at t = -12 h to 0.24 at t = -2 h, followed by a decrease to 0.14 at t = +12 h. Despite the strong increase of peak precipitation with K-index (figure 3.8 (d)), the maximum correlation is weak. Apart from a still significant amount of scatter, this can also be explained by the large range (up to 25 K) where there is hardly any increase in the peak intensity with increasing K-index. Of the three moisture and stability terms that form the K-index (equation (3.1)), the correlation with precipitation intensity of the LLM resembles the correlation of the K-index the most, and even exceeds it (table 3.3). There is hardly any correlation between precipitation intensity and the MLH or LTS. Apparently, this combination of qualities does not lead to an enhanced correlation with the peak intensity.

In contrast to tropical results (Dorrestijn et al., 2014; Davies et al., 2013), the correlation between the vertical velocity and the peak intensity is almost nonexistent at $\pm$12 hours and is nearly symmetrical about the time of the event, at which it peaks at 0.15. This very weak correlation is in line with the leveling off seen in figure 3.7 (a), and the weak relation between the vertical velocity and peak intensity seen in figure 3.8 (a). While these figures show that precipitation intensities are more prone to stronger upward velocities, the distinction between moderate (80th percentile) and more extreme precipitation (99th percentile) is weak.

To investigate whether these correlations depend on the intensity range, figure 3.9 also show the correlations for lower intensities (decile range 0 to 90, blue) and the upper decile range (red). While the correlations of CAPE (b), the water vapor path (c) and the K-index (d) are mainly determined by the highest peak intensities, the correlation with large-scale vertical velocity (a) is mainly controlled by the lower intensities. This is not an unexpected result, since lower intensities often occur in the presence of fronts. Overall, these results suggest that while large-scale vertical velocity tends to be higher for high peak intensities than low peak intensities, the atmospheric stability becomes a controlling factor for more extreme precipitation to occur.

The correlations depicted in figure 3.9 are rather weak and follow similar temporal patterns as in figure 3.7. It seems counterintuitive for a correlation

to be weak, despite strong stratification for precipitation deciles. But a strong stratification based on precipitation percentiles does not necessarily mean that this parameter will be a good indicator for precipitation. Figure 3.8 has already shown that there is a large amount of scatter in these relations, that ultimately leads to the weak correlations seen in figure 3.9. Even for CAPE, which has the highest peak-correlation, figure 3.8 (c) shows that a high CAPE can still lead to a large range of peak intensities. In order to find an atmospheric indicator for extreme precipitation, it may be necessary to combine the atmospheric parameters discussed here.

3.5 Summary and final remarks

With this study, we present a comprehensive statistical analysis of atmospheric conditions for the precipitating atmosphere and precipitation controlling factors at midlatitudes. To this end, in situ precipitation observations over the Netherlands are used in combination with atmospheric data from a high-resolution reanalysis. To remove double counting, the data has been evaluated in an event based setting.

To gain a better understanding of what the precipitating atmosphere looks like, we have performed profile and temporal analyses of large-scale atmospheric conditions and forcing. Separation of the data into precipitation deciles was used to reveal the change in atmospheric conditions with increasing event intensity. These analyses have shown that heavy precipitation events tend to occur under warmer, moister conditions than weaker events, and have a stronger temporal signal.

The large-scale vertical velocity is positive, which is associated with large-scale convergence, and nearly doubles for strong peak intensities with respect to the weakest precipitation decile. The temporal signal also increases for more extreme peak intensities. Driven by vertical advection, the dynamical temperature and moisture tendencies are strongest for the heaviest peak intensities, and show cooling and moistening prior to the event. This is largely compensated by the condensation and condensational heating resulting in a precipitation response. The total tendencies, temperature in particular, are much weaker than

the separate dynamical (large-scale) and physical (convection) components, suggesting near convective quasi-equilibrium.

Based on the profile analysis, we have evaluated four atmospheric parameters as potential precipitation indicators at midlatitudes; the large-scale vertical velocity, CAPE, the water vapor path and the K-index. The temporal signal tends to increase with increasing precipitation deciles, indicating that these atmospheric parameters are more strongly influenced by the event than weaker events. Furthermore, the stratification of the atmospheric parameters increases for increasing deciles of peak intensity, apart from the vertical velocity, which shows a leveling off for the upper 20% of peak intensities. Overall, the strongest events are prone to stronger convergence, and take place under moister, more unstable conditions than weaker events.

However, this does not necessarily mean that, for example, a very unstable atmosphere will always lead to heavy precipitation. In fact, the relations between the peak intensity and all four atmospheric parameters contain a large amount of scatter. The leveling off seen for high precipitation percentiles of ω_{LS}, is not caused by a physical process, but is induced statistically by the weak increase of peak intensity with vertical velocity, and the large spread of the vertical velocity. Because of the large spread, the mean vertical velocity does not increase much with increasing intensity deciles, even though individual values of omega can be much higher. This also leads to a very weak correlation between the large-scale vertical velocity, and peak intensity. The other parameters show a stronger increase, but also contain large amounts of scatter, again leading to weak correlations. With 0.33, CAPE at -3 hours has the highest correlation with the peak precipitation intensity. A decomposition into weak to moderate (<4.7 mm/h) and heavy (>4.7 mm/h) peak intensities has shown that the correlation between peak intensity and CAPE is mainly determined by heavy intensities, while the opposite is true for the vertical velocity.

Interestingly, CAPE and the vertical velocity show large variations in time, whereas atmospheric moisture hardly shows a temporal signal. The K-index, which is based on both absolute and relative moisture, as well as the vertical temperature gradient, displays an in-between behavior. This suggest that moisture is a background forcing; precipitation tends to be more extreme with higher moisture contents, but at the same time does not link very well with the timing

of the event. On the other hand, CAPE and the vertical velocity do appear to be linked to the timing of the event. The high variations in CAPE also show that using CAPE from proximity data such as radio sondes, has its limitations, possibly explaining the different results reported on the relation between CAPE and precipitation extremes (Dyson et al., 2014; Barkidija & Fuchs, 2013).

In summary, we presented an analysis of the relation between atmospheric conditions and large-scale forcing related to precipitation evens of different magnitudes, with an emphasis on the most extreme cases. This research has shown that overall, the strongest precipitation events take place under warmer, moister conditions than weak events, enduring stronger large-scale convergence. The temporal signal of these attributes with respect to the time of the peak intensity increases with increasing peak intensity deciles as well. These results do not translate to one single indicator for precipitation, unlike the tropics, where strong relations are found between convection and convective precipitation, and the vertical velocity (Dorrestijn et al., 2014; Davies et al., 2013). Apparently, while high deciles of peak intensity do show a preference for high moisture, instability and large-scale convergence, none of these conditions are reliable indicators for high precipitation amounts.

Acknowledgements

This study was funded by Knowledge for Climate theme 6. For the RACMO data and the radiosondes used to validate CAPE, contact Geert Lenderink (geert.lenderink@knmi.nl). The automated weather station data used in this study can be obtained from www.knmi.nl/uurgegevens.

4

Large-scale controls on extreme precipitation

Large eddy simulations with strong lateral forcing representative of precipitation over the Netherlands are performed to investigate the influence of stability, relative humidity, and moisture convergence on precipitation. Furthermore, a simple climate perturbation is applied to analyze the precipitation response to increasing temperatures. Precipitation is decomposed to distinguish between processes affecting the precipitating area and the precipitation intensity. It is shown that amplification of the moisture convergence and destabilization of the atmosphere both lead to an increase in precipitation, but due to different effects; Atmospheric stability mainly influences the precipitation intensity, while the moisture convergence mainly controls the precipitation area fraction. Extreme precipitation intensities show qualitatively similar sensitivities to atmospheric stability and moisture convergence. Precipitation increases with RH due to an increase in area fraction, despite a decrease in intensity. The precipitation response to the climate perturbation shows a stronger response for the precipitation intensity than the overall precipitation, with no clear dependency of changes in atmospheric stability, moisture convergence and relative humidity.

Accepted article:

J. M. Loriaux, G. Lenderink and A. P. Siebesma, Large-scale controls on extreme precipitation, *J. Clim*, 2016

4.1 Introduction

In view of the disruptive nature of precipitation extremes to society, many studies have been published on the behavior of extreme precipitation, and its response to climate change (O'Gorman, 2015; Westra et al., 2014). Model predictions indicate that extreme precipitation will intensify and become more frequent with warming (IPCC, 2014), and studies have already been able to attribute changes in extreme precipitation to observed warming (Min et al., 2011; Pall et al., 2011; Lenderink & Attema, 2015). However, the magnitude of the response is quite variable (e.g. O'Gorman, 2012), and the sensitivity of the response to mesoscale conditions is not yet completely understood, in either present-day or future climate.

Present-day relations between observed temperature and precipitation extremes show an increase of approximately 7% to 14% K^{-1}, depending on the surface temperature, over Western Europe (Lenderink & Meijgaard, 2008; Lenderink & van Meijgaard, 2010; Berg et al., 2013; Blenkinsop et al., 2015). Similar results were found for stations across Australia (Hardwick-Jones et al., 2010a) and the United States (Mishra et al., 2012). Since these observed sensitivities of extreme precipitation may not necessarily translate to a response to global warming (Westra et al., 2014), it is important to understand the physical processes that influence extreme precipitation as well as the precipitation response.

The moisture holding capacity of the atmosphere increases with temperature. In areas where enough moisture is available, the specific humidity of the atmosphere will increase following the Clausius-Clapeyron equation. Near the surface, this amounts to an increase of approximately 6-7% K^{-1} (CC scaling). If thermodynamics are dominant in determining extreme precipitation intensities, they are expected to increase at the same rate (Allen & Ingram, 2002). However, precipitation extremes can be invigorated or diminished by dynamical processes (Trenberth et al., 2003; Emori & Brown, 2005) and microphysics (Singh & O'Gorman, 2014). These components are conceptualized in the following approximation of the precipitation rate:

$$P \approx -\epsilon \int_{z_b}^{z_t} w_c \frac{\partial q_{s,c}}{\partial z} \rho dz. \tag{4.1}$$

This equation simply states that the precipitation rate, P, is determined by a precipitation efficiency, ϵ, times the vertically integrated condensation rate in the cloud. The condensation rate consists of a dynamical, and thermodynamical contribution; through the updraft velocity, w_c, and the vertical derivative of the saturation specific humidity following the parcel, $q_{s,c}$, respectively. If the updraft velocity and efficiency are constant with warming, for deep convection the precipitation response leads to CC scaling.

Analysis of the precipitation response to climate change in terms of equation (4.1) has been presented in numerous studies, using general circulation models (O'Gorman & Schneider, 2009a,b), cloud-resolving models (Muller et al., 2011; Romps, 2011; Muller, 2013; Singh & O'Gorman, 2015) and a conceptual model (Loriaux et al., 2013). While the thermodynamical component is understood quite well, the other components remain rather difficult to predict.

The influence of large-scale dynamics and environmental conditions on extreme precipitation, which indirectly influences the different components of (4.1), is not yet understood well enough. Combining observations and reanalysis data, Davies et al. (2013) have studied the relations between large-scale moisture convergence, stability parameters and tropical precipitation, finding that convective precipitation has a strong relationship with the large-scale vertical velocity and moisture convergence. Another study has analyzed circulation and several atmospheric conditions in relation to midlatitude peak precipitation (Loriaux et al., 2016b), finding only weak relationships with atmospheric stability and vertical velocity. Here, we present a sensitivity study based on the Loriaux et al. (2016b) setup to investigate the role of large-scale dynamics and environmental conditions on precipitation and on the precipitation response to climate change.

For this purpose, we use a large-eddy simulation (LES) model to simulate strong convective precipitation typical for the Netherlands based on composite profiles of the highest 10 percentiles of peak intensities as described by Loriaux et al. (2016b). Realistic large-scale advective tendencies for heat and moisture are used to drive the simulations. Using these atmospheric conditions as a reference, we systematically vary the relative humidity, stability and large-scale vertical velocity. Furthermore, this analysis is repeated under a temperature perturbation, to simulate a warmer climate.

Within a convective framework, based on a case study of Loriaux et al. (2016b), we thus aim to

1. understand how precipitation depends on atmospheric conditions and lateral forcing, and

2. analyze how precipitation is affected by a climate perturbation.

To this end, we first present our methods in section 4.2. This is followed by the results for the present-day climate in section 4.3, where we present sensitivity analyses of the moisture budget, attribute changes in the mean precipitation to changes in the precipitation area and changes in the intensity of precipitation, and assess the behavior of extreme precipitation. In section 4.4, we present an analysis of the response of these precipitation parameters to climate change. Finally, the implications of these results and the conclusions of this study are presented in section 4.5.

4.2 Methodology and case setup

Loriaux et al. (2016b) provide an event based analysis which describes the atmospheric conditions accompanying precipitation events grouped by intensity deciles, from 12 hours prior to 12 hours after the peak intensity of the event. These conditions follow from 20 years of in situ precipitation data over the Netherlands (KNMI, 2014), accompanied by a high resolution model dataset (12 km). This dataset consists of a series of consecutive hindcasts over a period of 20 years using the Regional Atmospheric Climate Model (RACMO,Van Meijgaard et al., 2008), forced and initialized by the ERA-interim reanalysis (Dee & Coauthors, 2011).

Using the same datasets as Loriaux et al. (2016b), a strongly precipitating composite case has been derived by grouping together the upper 10% of the precipitation peak intensities from 12 hours prior to 12 hours after the peak intensity of the event. Only afternoon hours (12 to 20 CET) have been selected, since we are specifically interested in simulating daytime convective precipitation. The resulting composite case starts at 5 CET, and peaks at 17 CET. We will use this composite as the standard reference case to be simulated with

the Dutch Atmospheric Large Eddy Simulation model (DALES 4.0, Heus et al., 2010; Böing et al., 2012), with the ice microphysics scheme described by Böing et al. (2012).

DALES is an anelastic, high resolution model that resolves the largest turbulent eddies and parameterizes the smaller turbulent eddies realistically using the well known turbulent scaling relations in inertial subrange. The prognostic variables are the three wind components u, v, w, the liquid water potential temperature θ_l, the total water specific humidity q_t, and finally, q_r, the rainwater specific humidity. In the model, the total water specific humidity and the liquid water potential temperature are defined as

$$q_t = q_v + q_c, \tag{4.2}$$

$$\theta_l = \theta - \frac{L_v}{c_{pd}\Pi} q_c, \tag{4.3}$$

respectively. Here, q_v is the specific humidity, q_c is the cloud condensate that contains both cloud liquid water and cloud ice. Furthermore, θ describes the potential temperature and $\Pi = (p/p_0)^{R_d/c_{pd}}$ the exner function. The latent heat of vaporization is given by L_v, and the heat capacity for dry air is c_{pd}. The gas constant of dry air is R_d.

All runs are performed over a domain of 96x96x22 km with a horizontal resolution of 200 m, and 240 non-equidistant vertical levels, spaced apart 40 m near the surface, up to 175 m at 22 km. This horizontal resolution is supported by Stein et al. (2015). A test run with a larger domain did not have any noticeable effects on the simulation. This was not pursued further in this study. Initial profiles of liquid water potential temperature and total water specific humidity 12 hours prior to the peak intensity of the composite case study are used as initial conditions for the reference case; figure 4.1 (a), (b). The resulting relative humidity profile is shown in figure 4.1 (c). The initial horizontal wind is taken unidirectionally and increases with height from approximately 6 m/s at the surface, to 20 m/s at the tropopause (not shown).

Besides initial conditions it is crucial to prescribe realistic large-scale forcings originating from scales larger than the domain of the model. The large-scale forcing terms can be introduced by considering the prognostic equations of

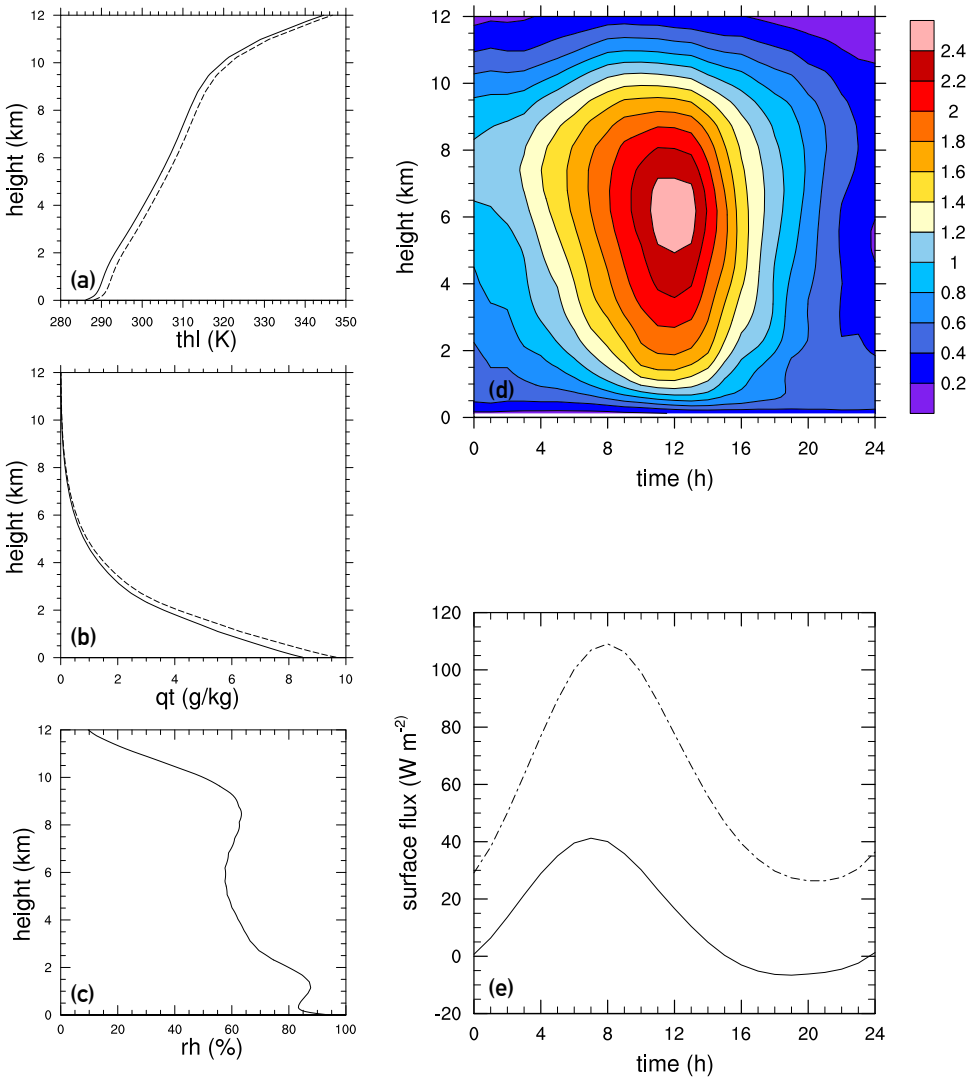

Figure 4.1: Model input parameters. The initial reference profiles of liquid water potential temperature (a), total water humidity (b), and relative humidity with respect to water (c). The dashed lines indicate the perturbed climate profiles. Note that for the reference and perturbed climate, the relative humidity profiles are identical. Figure (d) shows the time-height representation of the large-scale vertical velocity (cm/s). The sensible (solid) and latent (dashed) heat fluxes at the surface are shown in (e).

$\phi = \{\theta_l, q_t, u, v, w\}$ averaged over the domain of the LES model in a schematic way

$$\frac{\partial \overline{\phi}}{\partial t} = \left(\frac{\partial \overline{\phi}}{\partial t}\right)_{LES} + \left(\frac{\partial \overline{\phi}}{\partial t}\right)_{LS} \tag{4.4}$$

where the overbar denotes an average over the LES domain. The first term on the right hand side denotes the tendencies resolved by the LES model while the second term hosts contributions from the large-scale that can not be represented by the LES model. For the heat and moisture equation, i.e $\phi = \{\theta_l, q_t\}$ these are essentially the large-scale advection terms. The large-scale advection terms have been derived from the composite event. Comparison of the magnitudes of the advection terms show that, especially around the maximum peak intensity, the vertical advection term dominates over the horizontal advection term. We therefore approximate the large-scale forcing by only taking the vertical advection term into account, i.e.,

$$\left(\frac{\partial \overline{\phi}}{\partial t}\right)_{LS} = -\overline{u}\frac{\partial \overline{\phi}}{\partial x} - \overline{v}\frac{\partial \overline{\phi}}{\partial y} - \overline{w}\frac{\partial \overline{\phi}}{\partial z} \simeq -\overline{w}\frac{\partial \overline{\phi}}{\partial z} \tag{4.5}$$

Therefore, the large-scale forcing of heat and moisture in this study can, to first order, simply be prescribed by the large-scale vertical velocity $\overline{w}$.

Since the moisture budget plays a crucial role in this study, we derive the resulting vertical integrated moisture budget. The LES resolved tendency for $\phi = q_t$ is given by

$$\left(\frac{\partial \overline{q}_t}{\partial t}\right)_{LES} = -\frac{1}{\overline{\rho}}\frac{\partial \overline{\rho}\,\overline{w'q'_t}}{\partial z} - G \tag{4.6}$$

where the first term describes the moistening due to vertical turbulent transport, ρ denotes the density that only depends on the height and G represents the autoconversion rate from q_t to rain. Primes denote deviations from the domain average values. Substituting (4.6) and (4.5) into (4.4) and vertical integrating gives

$$\int_0^{\text{toa}} \frac{\partial \overline{q_t}}{\partial t}\overline{\rho} dz = -\int_0^{\text{toa}} \overline{\rho w}\frac{\partial \overline{q}_t}{\partial z} dz + \overline{\rho}_0 \overline{w'q'_{t0}} - \overline{P}, \tag{4.7}$$

which describes the moisture budget of the domain. Here $\overline{P}$ denotes the domain averaged surface precipitation while the second term on the right hand side

represents the surface evaporation. The vertical advection in (4.7) represents the large-scale moisture convergence.

The prescribed large-scale vertical velocity $\overline{w}$ is shown in figure 4.1 (d) and is derived from the composite event that we are aiming to simulate. It increases up to t = 12 h, with a maximum of approximately 2.4 cm/s at 6 km, steadily decreasing until the end of the simulation after that. As a result, the moisture convergence also increases up to 12 h, peaking at approximately 12.5 mm/day, after which it decreases again. In addition, the simulation is forced over time by prescribed values of the surface sensible and latent heat fluxes (figure 4.1 (e)), and the geostrophic wind from 12 hours before, to 12 hours after the peak intensity. These parameters are also taken from the composite case. Since the domain averaged radiative tendencies are weaker than the heating terms due to convection and large-scale advection (up to 6 K day^{-1}), we have ignored radiative cooling effects in this case for simplicity. All further details of the profiles and forcings used to set up this LES study can be found online at (Loriaux et al., 2016a).

In addition to the reference experiment described above, a number of additional experiments are defined in which the relative humidity, vertical stability of the mean initial profiles are systematically varied as well as the strength of the prescribed large-scale vertical velocity. This way, the strength of the precipitation response as a function of the initial conditions and the large-scale forcing can be systematically assessed.

The stability is perturbed by subtracting a moist adiabatic correction term from the initial potential temperature profile,

$$\theta = \theta_0 - \alpha \frac{L_v}{c_p \Pi} q_{l,ma}. \tag{4.8}$$

Here, θ_0 is the initial profile of the reference experience. $q_{l,ma}$ is the liquid water humidity for a moist adiabat based on the surface conditions. α is the stability factor. For $\alpha = 0$, the profile is unchanged and remains close to the moist adiabat. For $\alpha = 1$, the profile approaches the dry adiabat, becoming extremely unstable. We've chosen values of α between -0.075 and 0.225 in steps of 0.075, which for the reference experiment leads to potential temperature lapse rates ranging from 2.1 K km^{-1} to 3.6 K km^{-1} at 1100 m, a typical level for cloud

base in this experiment. Figure 4.2 (a) shows the perturbations to the reference liquid water potential temperature profile.

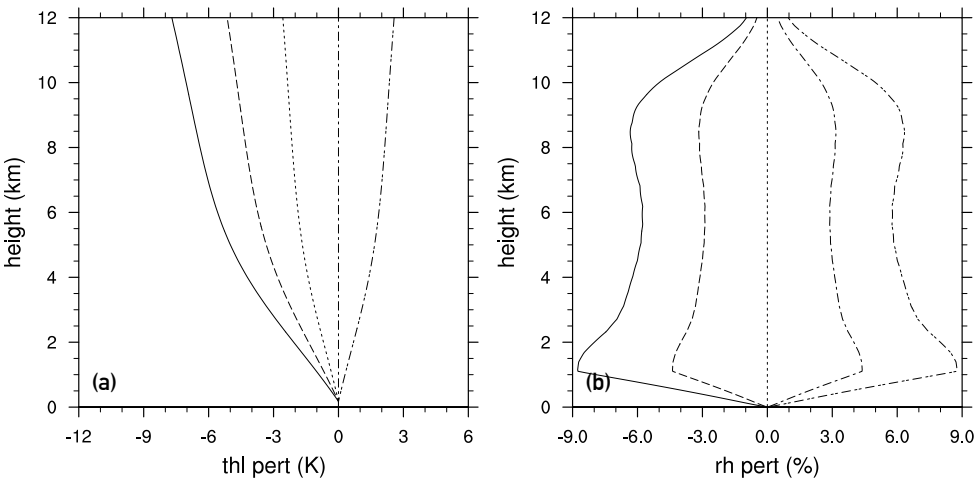

Figure 4.2: Perturbations to the initial reference profiles of the liquid water potential temperature (a) and relative humidity (b).

The relative humidity is perturbed by multiplying the initial relative humidity by a factor ranging from 0.9 to 1.1 in steps of 0.05, from 1100 m up. Below that the factor decreases linearly to 1 at the surface. The resulting perturbations to the initial RH profile, as well as the profiles themselves are shown in figure 4.2 (b). This leads to a combined set of 25 experiments, based on five stability, and five relative humidity perturbations.

In order to analyze the influence of the large-scale moisture convergence, we have furthermore performed a few additional perturbations to the reference experiment, by multiplying the vertical velocity profiles by a factor of 0.5, 2 and 4. These perturbations lead to a moisture convergence that peaks at 6 to 60 mm/day, ranging from the weakest to strongest perturbation.

Finally, to assess the change in precipitation in a changing climate, we have performed a simple climate change simulation, by uniformly warming the reference experiment by 2 degrees, while keeping the relative humidity constant (Sherwood et al., 2010; Dal Gesso et al., 2014). Uniform warming is a reasonable assumption for midlatitudes, as was previously shown by Attema et al. (2014). Note that due to our choice of uniform warming, the atmospheric

stability with respect to moist processes decreases from present-day to future climate.

In this study, we will focus on the reference experiments of the present-day and future climate in more detail. Since single experiments contain a fair amount of noise due to the chaotic behavior of clouds, we have analyzed an ensemble of 5 members for both reference experiments in order to give an idea of the uncertainty of the results. In DALES, simulations are initialized by randomly perturbing the initial θ_l and q_t profiles. The array of random numbers used for these perturbations is determined by the randomization seed. Each ensemble member has a different randomization seed, but the same input profiles. These ensembles are used when analyzing the reference state of the present and future climate.

4.3 Present-day climate

The moisture budget plays a key role in understanding how precipitation responds to different forcings and atmospheric conditions. A symbolic representation of the vertically integrated moisture budget (4.7), is

$$S = M + E - P. \tag{4.9}$$

Moisture is added to the domain through lateral moisture convergence M and the surface evaporation E, and lost through precipitation P. Any imbalance between the inflow and precipitation will affect the moisture content of the domain. The difference between the gain and loss term makes up the moisture tendency, which describes if the domain is becoming moister or drier. This is the storage term S. If more moisture is added to the system, but the storage term remains relatively the same or decreases, the precipitation efficiency increases, and vice versa.

First, we take a look at the temporal development of the moisture budget of the reference experiment. To this end, the temporal evolution of the moisture budget is shown in figure 4.3. The moisture input due to the latent heat flux at the surface maximizes at t = 8 h, at 3.5 mm/day. The lateral moisture convergence dominates the moisture input, peaking at t = 12 h, at 12.5 mm/day.

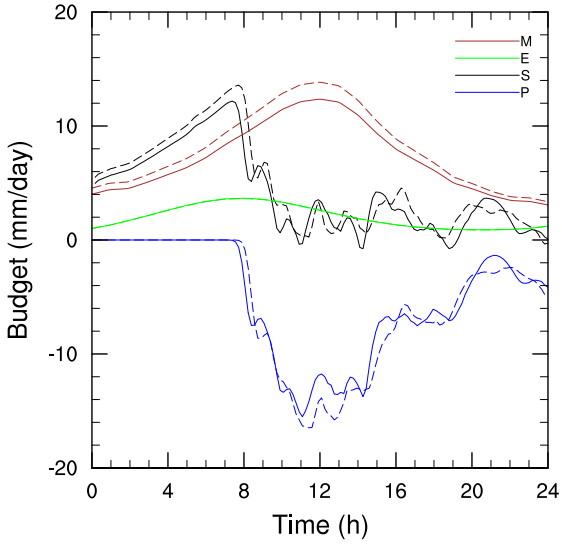

Figure 4.3: Moisture budget of the five-member ensemble mean reference experiment for the current (solid) and warm (dashed) climate.

In response to the increasing moisture input, the total water specific humidity of the domain increases, as can be seen in the storage term, until it starts to rain at t = 8 h. The precipitation very quickly picks up, causing the moisture tendency to drop. Following the moisture convergence, most precipitation falls between t = 10 h and t = 15 h, peaking at approximately -15 mm/day.

Figure 4.4 shows a precipitation snapshot of the domain at t = 12 h, at which time it has been raining for a while, and the precipitation intensities are high. There are several small precipitation clusters, with diameters of approximately 5 km, most of which have maximum precipitation intensities that exceed 5 mm/10 min. The largest cluster is located at x = 30 km, y = 50 km, and spans approximately 10 by 20 kilometers. In this cluster, precipitation intensities are found that are far higher than 10 mm/10 min. There are no clear signs of large-scale organization.

As can be seen in figure 4.3, the amount of precipitation weakens as the moisture convergence starts to decrease during the second half of the experi-

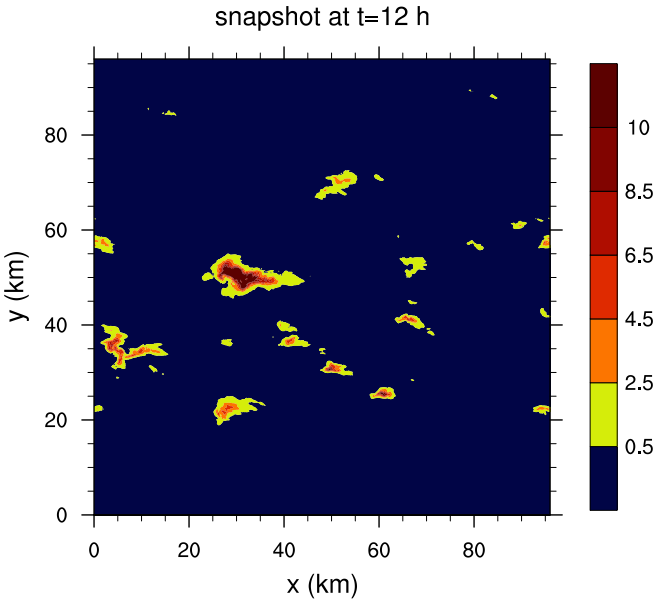

Figure 4.4: Precipitation intensity (mm/10 min) snapshot at the surface, at t = 12h.

ment. Once the precipitation sets in at t = 8 h, the moisture inflow is closely, but never completely balanced by precipitation, which means that the moisture content of the domain continues to slowly increase over time.

Next, we analyze the time averaged moisture budget of the domain;

$$\langle IN \rangle - \langle P \rangle = \langle S \rangle \,, \tag{4.10}$$

where $\langle .. \rangle = \int_{0h}^{24h} .. \; dt/t_{total}$, and $IN = M + E$. The sensitivity of the time integrated moisture budget to initial relative humidity and stability is shown in the left column of figure 4.5. The relative humidity perturbations are shown along the x-axis, the stability perturbations along the y-axis, with the most unstable, moist (stable, dry) conditions in the top right (bottom left). Figure 4.5 (a) shows the sensitivity of the moisture input in the present-day climate. As the latent heat flux is fixed, the dependence of the moisture input on the initial relative humidity and stability is completely due to the moisture convergence,

and maximizes for more stable, wet conditions. The moisture inflow increases by approximately 9% from the lowest to highest values.

The moisture loss term consists of the mean precipitation rate (b). It is influenced by both stability and relative humidity. With the highest values corresponding to the more unstable experiments with high relative humidity, this result is consistent with the results found by Böing et al. (2012). The mean precipitation rate approximately doubles from dry, stable, to moist, unstable conditions.

Since the sensitivity of the moisture convergence to RH and stability conditions is far lower than the domain averaged precipitation, the storage term approximately mirrors the precipitation (c). Storage is lowest for moist, unstable conditions, and highest for dry, stable conditions, where the mean precipitation is lowest. Similar to the precipitation, we see approximately doubling of the storage term over the phase space.

The domain averaged precipitation is not very informative concerning the actual precipitation intensity as the area of precipitation is less than 10% (see figure 4.4). We will therefore reserve the term precipitation intensity for the precipitation conditioned on the precipitating area. To this end, the mean precipitation rate $\langle \overline{P} \rangle$ can be further decomposed into the mean precipitation intensity, $\langle I \rangle$, and the mean precipitation area fraction, $\langle a \rangle$, the fraction of grid columns with precipitation reaching the surface,

$$\langle \overline{P} \rangle = \langle a \rangle \langle I \rangle . \tag{4.11}$$

A precipitation threshold of 0.01 mm/10 min is used.

Figure 4.6 shows the decomposition of the mean precipitation into the precipitation area fraction (a), and the mean intensity (b). The area fraction shows that on average, 5.5% of the domain is covered by precipitation. It is mostly determined by the relative humidity, and nearly doubles from the dry to moist perturbations. While the change in area fraction over the phase space is comparable to the mean precipitation, the stability hardly affects the area fraction.

Consequently, the mean intensity is not influenced by RH in the same way as the mean precipitation seen in figure 4.5 (c). Instead, the mean intensity is

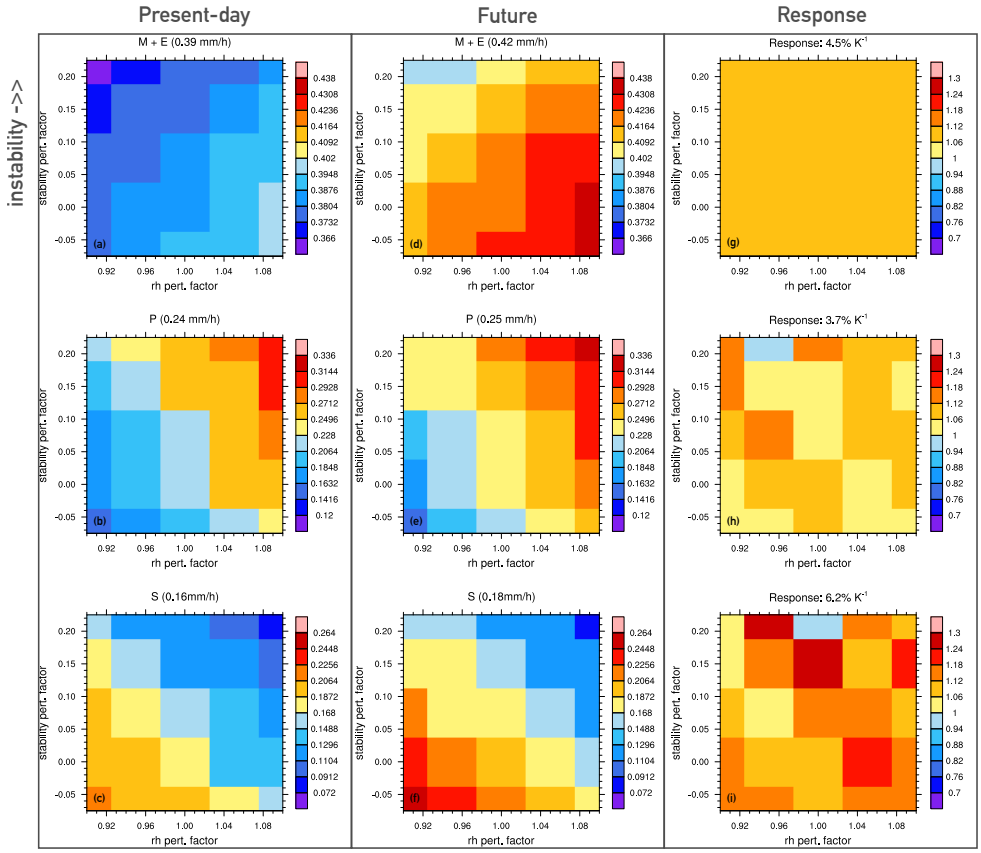

Figure 4.5: Phase space results of the moisture budget, showing the moisture input (a,d,g), precipitation (b,e,h) and storage (c,f,i) for the present-day (a-c) and future climate (d-f), and climate response (g-h). Relative humidity perturbations are shown along the x-axis; stability perturbations along the y-axis.

highest for unstable, but drier conditions. A physical interpretation of these results, is that when the relative humidity is high, it rains sooner, leading to many, light events. When the relative humidity is lower, more buildup is necessary before it rains, leading to fewer, but stronger events. The increase in precipitation intensity with instability follows from increased updraft velocities (not shown). Averaging at 4.3 mm h^{-1}, the mean intensity increases by approximately 60 % over the range of perturbations.

So far, we have focused on the mean precipitation. Although the mean state already represents strong convective precipitation by means of the experimental setup, we will also focus on the extremes of this experiment. Figure 4.7 (a) shows the probability of exceedance distribution of the precipitation intensity (data exceeding the precipitation threshold), for the 5-member ensemble mean reference experiment of the present day climate (black). The grey band denotes $\pm$ one standard deviation to the mean. Only approximately 20% of

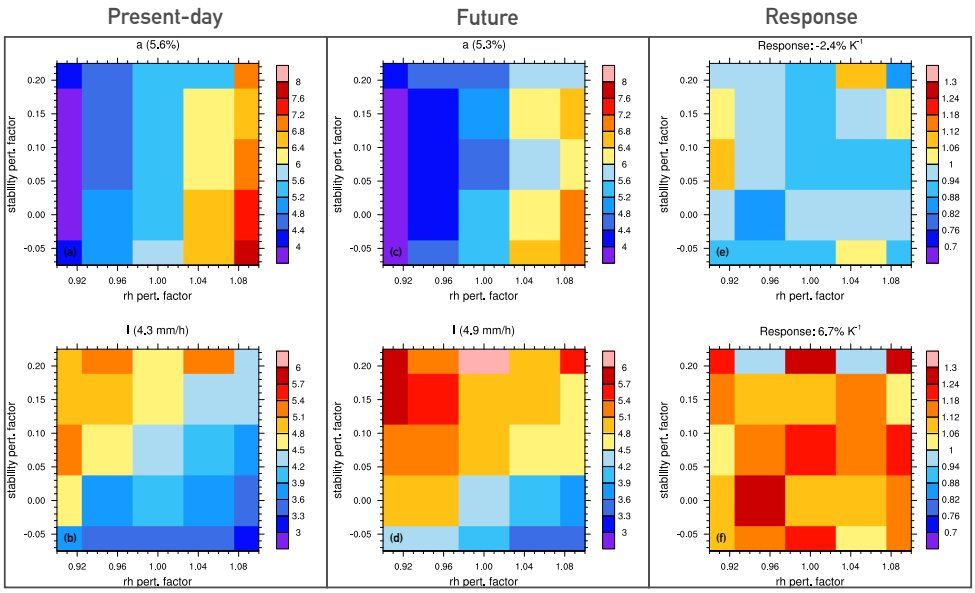

Figure 4.6: Phase space results of the area fraction (a,c,e) and precipitation intensity (b,d,f) for the present-day (a,b) and future climate (c,d), and climate response (e,f). Relative humidity perturbations are shown along the x-axis; stability perturbations along the y-axis.

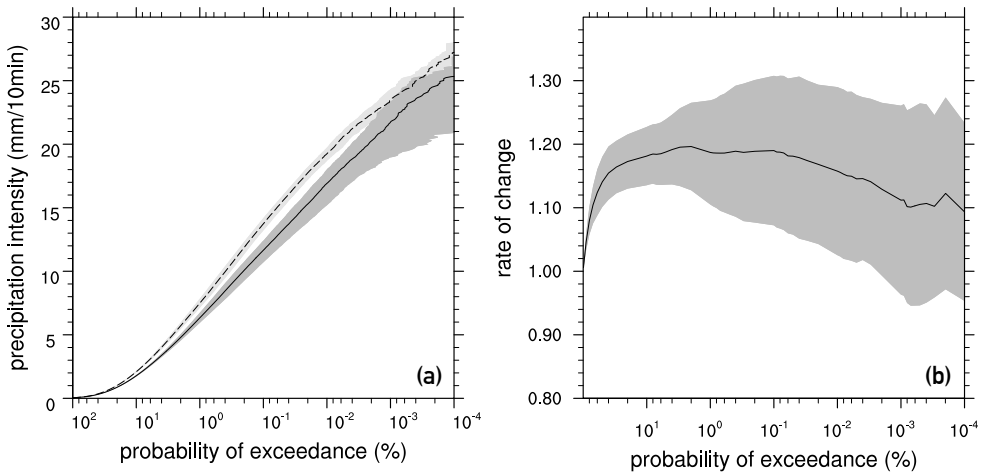

Figure 4.7: Probability of exceedance (a) and percentile response to the climate perturbation (b), using a precipitation intensity threshold of 0.01 mm/10 min.

the precipitation intensities exceed 1 mm/10 min, the highest intensities go beyond 25 mm/10 min. As can be expected, the standard deviation increases with decreasing probability of exceedance. Since we want to ensure that the sensitivity to the different perturbations can be reliably estimated, we will use the 99th percentile of the precipitation intensity (1 % exceedance) when looking at precipitation extremes. This corresponds to $\sim$6.5 mm/10 min for the reference experiment. The equivalent percentile for precipitation is approximately the 99.95th percentile (0.05% exceedance).

Figure 4.8 (a) shows the phase space for the extreme precipitation intensity. Similar to the mean intensity, the extreme precipitation is sensitive to stability and RH. When it is raining, a relatively dry but unstable atmosphere will lead to the strongest precipitation intensities. This supports the theory that there is more precipitation build-up for dry, but unstable conditions, eventually leading to stronger intensities. With an average extreme intensity of 43.6 mm h^{-1}, the extreme intensity increases by 60 % across the phase space.

However, extreme precipitation (not conditioned on the precipitation area) no longer depends on the initial RH, and increases as the initial stability of the atmosphere decreases (b). While the mean and extreme intensities share the same preference for drier, unstable conditions, extreme precipitation is not

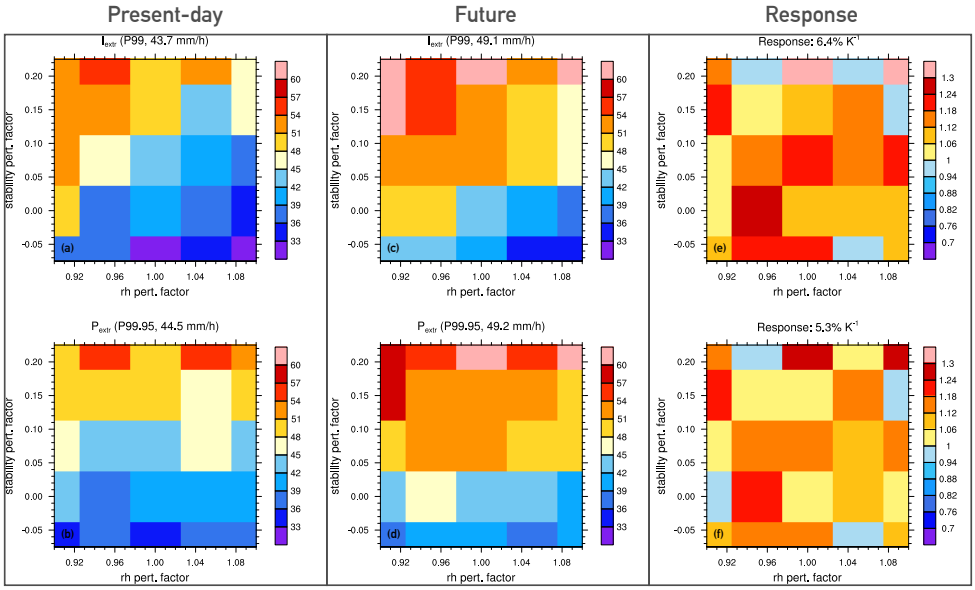

Figure 4.8: Phase space results of the extreme intensity (a,c,e) and extreme precipitation (b,d,f) for the present-day (a,b) and future climate (c,d), and climate response (e,f). Relative humidity perturbations are shown along the x-axis; stability perturbations along the y-axis.

predisposed toward high initial RH conditions like mean precipitation is. This is because the increase of the mean precipitation rate with increasing RH is caused by an increase in the area fraction, but a decrease in intensity. As a result, the upper percentiles of the distribution of the precipitation rate are not strongly affected by the RH for the range investigated in this study. Note that for low values of the relative humidity, a dependence of the extreme precipitation intensity is expected as the lack of moisture availability begins to play a role.

We next examine the role of large-scale dynamics on precipitation, by performing a few coarse perturbations to the large-scale vertical velocity, and hence the moisture convergence. Figure 4.9 (a) shows the relative change of the different components of the moisture budget due to these perturbations, with respect to the reference experiment. As a result of these perturbations, the total moisture input increases slightly less than the w perturbation factor. This, of course, is due to the unchanging surface LHF, which makes up for part

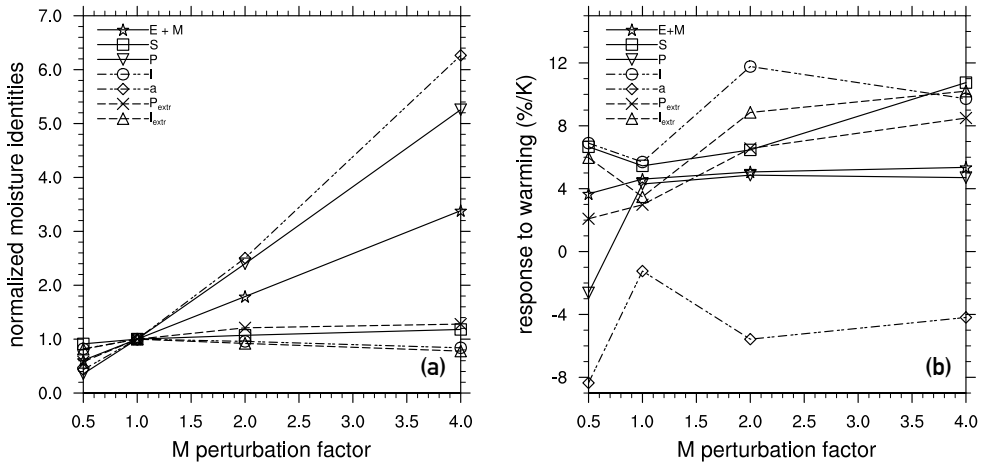

Figure 4.9: Response of the different components of the moisture budget and decomposition of P into the area fraction and precipitation intensity to vertical velocity perturbations in the present-day climate (left). Results are normalized for the reference (perturbation factor = 1). The figure to the right shows the response of mean and extreme precipitation, intensity and the area fraction to climate change for perturbations of the vertical velocity.

of the moisture input. Indeed, mean precipitation increases by more than the perturbation factor – up to 5.2 times the mean precipitation of the reference experiment.

In order to assess whether this change in mean precipitation is achieved by an increase in the area fraction, or intensity, we again decompose the mean precipitation rate. The precipitation intensity (I) and area fraction (a) are also shown in figure 4.9 (a). It is clear that the increase in mean intensity is caused by an increase in the precipitation area fraction, with a slight decrease in the mean intensity for larger moisture convergence. In other words, due to an increase in the large-scale vertical velocity, it rains more, rather than more intensely.

It is possible that this increase in the area fraction can simply be explained by the fact that in a domain that is favorable to convection, more large-scale uplift triggers more convective updrafts by lifting parcels to a level where they become unstable. In this setup, while the area fraction increases, the individual precipitation cells do not appear to grow much larger for higher moisture convergence. The area fraction is thus mostly increased because more of these

cells are present in the domain, rather than a higher level of organization. This should be further investigated in future work.

The same relations are seen for extreme precipitation (P_{extr}), albeit more subtle. While the extreme precipitation shows a small increase with increasing moisture convergence, the extreme intensity (I_{extr}) shows the same weak decrease as the mean intensity. Since the extreme precipitation increases with increasing moisture convergence, the decrease in the extreme intensity is probably caused by a shift in the intensity distribution toward weaker events, even though stronger intensities do also occur. However, it is clear that the moisture convergence has a stronger effect on the area fraction than the precipitation intensity.

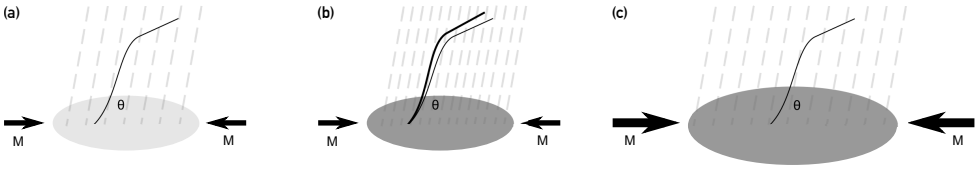

Figure 4.10: Conceptual drawing showing the effects of stability (b) and moisture convergence perturbations (c) on precipitation, with respect to the reference experiment (a). Destabilization and increased moisture convergence both lead to an increase in precipitation. This occurs through intensification (b), and an increase in the precipitation area fraction (c), respectively.

This concludes our sensitivity analysis of the present-day climate. The different effects of the stability and moisture convergence perturbations, both leading to an increase in precipitation, are visualized in figure 4.10; While increasing the atmospheric instability leads to more intense precipitation without greatly affecting the area fraction, moisture convergence leads to a larger precipitation area without substantially influencing the intensity. The relative humidity has two opposing effects. First, the higher the relative humidity, the more precipitation; this is best seen in the precipitation area fraction. Second, the lower the relative humidity, the higher the intensity. This is best seen in the sampled phase spaces, after the effect of the area fraction has been removed.

4.4 Future climate

We have performed a simple warming experiment by perturbing the initial temperature profile by 2 K while keeping the relative humidity constant. For comparison with the present-day climate, the same sensitivity analyses of the relative humidity and stability, and finally the vertical velocity, have been performed for the warm setup.

The dashed lines in figure 4.3 show the moisture budget of the warm run. It is clear that the temporal evolution of the experiment is quite similar to the reference. The moisture convergence rises as a result of the increase in total water specific humidity. In fact, with a growth of 7% K^{-1}, the moisture convergence is almost completely determined by the CC relation. This can be understood when we approximate the specific humidity of the future climate as $q_+ \approx q_{ref} * (1 + 0.07 * \Delta T)$ to account for the moisture increase of CC. After substituting this into M, it can be easily shown that the future climate moisture convergence equals the present-day moisture convergence multiplied by the CC increase factor. Note that in actuality, the CC factor slightly increases with height in the troposphere.

The center column of figure 4.5 shows the phase spaces of the time integrated moisture budget components for the warm setup. The right column shows the rate of change between the warm, and present day climate, normalized by the temperature perturbation. With an increase of approximately 9% from dry, unstable conditions, to moist, stable conditions, the sensitivity of the mean moisture input (d) to initial stability and relative humidity remains the same as the for the present-day climate. As a result, the increase in moisture input from the present-day to future climate is very robust, at 4.5% K^{-1}, with a spread of 4.2 to 4.6% K^{-1} (g). The response of the moisture input is weaker than the response of the moisture convergence alone because the surface evaporation remains constant.

Similar to the present-day climate, the precipitation rate of the future climate also increases from stable, dry, to unstable, wet conditions (e). The mean precipitation increases on average by 3.7% K^{-1} (h). There is no clear sensitivity pattern in the response, which means that the change in mean precipitation is not very sensitive to the initial conditions.

The storage term (f) again depends on stability and RH the same way as in the present-day climate, increasing from moist, unstable conditions to drier, more stable conditions. From present-day to future climate, the storage term grows by approximately 6.2% K^{-1} (i). The variation in this phase space is quite high, but again, no dependence on stability or relative humidity can be observed.

In order to determine whether the relative importance of the area fraction and mean wet precipitation intensity changes due to the climate perturbation, we return now to figure 4.6. Quick comparison of the area fraction (c) and mean precipitation intensity (d) with the reference shows that the dependencies of the moisture budget on initial stability and relative humidity do not change due to warming. Furthermore, as can be seen in (e) and (f), respectively, the response does not depend on the initial relative humidity or stability for either components. The area fraction shows a slight decrease, of approximately 2.4% K^{-1}due to warming, while the mean intensity increases by approximately 6.7% K^{-1}. This means that as a result of warming, it will on average rain slightly less, but more intensely.

The probability of exceedance for the 5-member ensemble run of the warm climate reference experiment (figure 4.7 (a)) shows that precipitation intensities are consistently higher than in the present-day climate. Figure 4.7 (b) shows the fractional rate of change of percentiles of the precipitation intensity for the ensemble reference experiments of the present-day and future climate. From the 60th to the 99.99th percentile, the fractional rate of change shows a fairly robust increase, between 7 and 10% K^{-1}. For higher percentiles the fractional rate of change is slightly lower, with an increase of 5 to 7% K^{-1}. The grey band denotes $\pm$ one standard deviation, showing that the spread is quite large, especially for the high percentiles.

Figure 4.8 shows the dependence of extreme precipitation on initial relative humidity and stability in the warm climate (c),(d) and the rate of change from present-day to warm climate (e),(f). The climate perturbation does not change the dependencies of the extremes within the phase spaces, but does lead to an increase in both extreme precipitation and intensity. On average, the extreme intensity increases by 6.4% K^{-1}due to the climate perturbation (e), which is slightly below the rise in the mean intensity. Due to the decrease in the area fraction, the response of extreme precipitation to the climate perturbation is a

bit weaker; 5.3 % K^{-1} (f).

The climate response of the moisture budget, precipitation components and extremes for perturbations of the large-scale dynamics through M, are shown in figure 4.9 (b). The response of the components of the moisture budget show that with an increase of approximately 4.5 to 5 % K^{-1}, the response of the moisture gain ($M + E$) and loss (P) terms are hardly affected by enhancing the large-scale dynamics. This leads to an increase of the storage response S from approximately 5.5% K^{-1} up to 11% K^{-1} with increasing perturbations of M. For weaker large-scale dynamics (a perturbation factor of 0.5), the mean precipitation decreases as a result of warming, and the storage again has a strong, positive response. Overall, the budget components do not show clear systematic dependencies of the moisture convergence.

Similar to figure 4.6 (e), the area fraction decreases due to warming. With a response between -8 and -1% K^{-1}, there is quite a large spread, but no clear dependence of the response on the amount of large-scale forcing applied. The response of the mean (I) and extreme (I_{extr}) intensity also have a large spread, in the range of 6% K^{-1} to 12% K^{-1} and 4% K^{-1} to 10% K^{-1}, respectively, without a clear dependency on the large-scale dynamics. The response of the extreme precipitation does appear to increase with increasing moisture convergence. As was found in the sensitivity analysis with respect to relative humidity and stability, the response of the extreme intensity is stronger than the extreme precipitation response.

Overall, these result suggest that the change in precipitation characteristics in a future climate are not very sensitive to the relative humidity, stability, and moisture convergence. As a result of warming, more moisture is brought to the system, leading to moistening (storage), and higher mean and extreme precipitation. This is accomplished by means of higher precipitation intensities, while the precipitation area fraction slightly decreases.

4.5 Discussion and conclusions

We have set up a composite LES case for convective precipitation using strong large-scale forcing based on idealized profiles for the highest 10 percentiles of

peak intensities over the Netherlands, as described by Loriaux et al. (2016b). In this setting, we have performed sensitivity analyses for atmospheric stability, large-scale moisture convergence, and relative humidity, and compared present-day climate to a warmer future climate.

Sensitivity analysis has shown that precipitation responds differently to changes in relative humidity, stability and large-scale moisture convergence. Mean precipitation increases with relative humidity. However, decomposition in intensity and precipitation area fraction shows that while the area fraction also increases with relative humidity, the intensity decreases. This indicates that when the relative humidity rises it rains sooner, leading to more but weaker precipitation due to the lack in buildup of precipitable water prior to the event.

By enhancing the instability of the atmosphere or the moisture convergence, the mean precipitation increases. However, this increase is caused by two different effects. While the rise in precipitation with heightened instability is caused by an increase in the mean intensity with only minor changes in the area fraction, the opposite is true for the increased precipitation rate due to large-scale moisture convergence. Here, the increase in the mean precipitation rate is caused by a very distinct expansion of the area fraction, but the mean intensity remains relatively constant.

Changes in the behavior of extreme versus mean precipitation with respect to the relative humidity and large-scale moisture convergence indicate a shift in the precipitation distribution. For example, due to an increase in relative humidity, non-precipitating points become weakly precipitating points. This does not influence the extreme precipitation rate, but does lead to a shift in the intensity distribution towards weaker intensities. As a result, the extreme intensity decreases with increasing relative humidity, while extreme precipitation remains constant with respect to relative humidity perturbations.

Similar to the precipitation response to relative humidity, the rise in mean precipitation with increasing moisture convergence is caused by an expansion of the area fraction. Therefore, it is not surprising that the extreme intensity decreases with increasing moisture convergence. However, unlike the relative humidity, the moisture convergence does lead to a small increase in the extreme precipitation rate. This indicates that while the intensity distribution does shift toward lighter intensities, higher intensities also increase.

The sensitivities of mean and extreme precipitation to the initial relative humidity, stability and large-scale forcing in the future climate are very similar to the present-day climate. As a result, no patterns can be found in the phase spaces of the precipitation response, indicating that the relations between precipitation and large-scale conditions in the present-day climate, are robust for a changing climate.

The precipitation response to climate change is weaker than expected based on observed relations between temperature and precipitation intensity in the present day climate. The response of the precipitation intensity follows CC scaling (6-7% K^{-1}) for both mean and extreme intensities. The area fraction decreases from present-day to future climate, causing the precipitation response to be lower than the response of the precipitation intensity. In other words, our climate perturbation indicates that with warming, it will rain more intensely but in less places, leading to a mean increase in precipitation of 3.5% K^{-1}).

This setup has provided useful insights regarding the sensitivity of precipitation to large-scale forcing and atmospheric conditions, and the continuity of the phase space patterns give us confidence in the results. However, it might be useful to study in more detail why this setup did not reach expected super-CC precipitation responses. We have seen in equation (4.1) that for local precipitation a response below CC scaling can be caused by dynamics or the precipitation efficiency. Here, the dynamical contribution is connected to the updraft velocity, while the precipitation efficiency contains information on the entrainment and detrainment, autoconversion rate and other processes controlling the precipitation intensity. Using conditionally sampled profiles, it is possible to approximate a convective plume. This can be used to determine the climate response for a constant precipitation efficiency based on equation (4.1) to examine if the combined dynamical and thermodynamical contributions explain the precipitation intensity response found in this study of 6.5% K^{-1};

$$I_{th,d} = -\int_{z_b}^{z_t} w_c \frac{\partial q_{s,c}}{\partial z} \rho dz, \tag{4.12}$$

where the subscript c indicates that the it concerns fields that are averaged only over the active convective updrafts. A positive dynamical contribution will cause the approximated intensity response to exceed CC scaling, and vice versa.

Strong deviations of the response of $I_{th,d}$ from 6.5% K^{-1} would suggest that the precipitation efficiency is an important factor in determining the precipitation response. Preliminary results using cloud core sampled profiles ($q_l > 0$ and $\theta_v > 0$) do suggest a strong dynamical component, leading to a super-CC response of $I_{th,d}$. Future work should focus on following precipitation events by means of a clustering scheme, in order to better connect the large-scale conditions to the event-scale (thermo)dynamics and efficiency.

Acknowledgements

The authors would like to thank Steef Böing and Huug Ouwersloot for their useful comments regarding the use of DALES. This study was funded by Knowledge for Climate, theme 6. Furthermore, NWO/Surfsara sponsored the use of supercomputer facilities. Geert Lenderink acknowledges financial support from the EU grant INTENSE (FP7-IDEAS-ERC, project nr 617329).

5

Conclusions and outlook

In this thesis, we have investigated certain aspects of extreme precipitation in relation to atmospheric conditions.This was done by investigating roughly four research questions;

1. How robust is the observed 2CC scaling between extreme precipitation scaling and (dew point) temperature?
2. Which local processes are responsible for the 2CC scaling relation?
3. How does precipitation depend on atmospheric conditions and large-scale forcing?
4. How are these relations affected by climate change?

This chapter holds the main conclusions of this work followed by a brief outlook.

5.1 Conclusions

1. How robust is the observed 2CC scaling between extreme precipitation scaling and (dew point) temperature?

Previous work (Lenderink & Meijgaard, 2008; Lenderink et al., 2011) has suggested a 2CC increase (approximately 14 % K^{-1}) of convective precipitation extremes over the Netherlands and Hong Kong. However, the origin of this scaling has been the center of debate due to a scale break in the hourly data from low to high temperatures. It has been proposed (Haerter & Berg, 2009) that the observed 2CC intensity increase with (dew point) temperature might

be artificial, caused by a statistical enhancement due to the mixing of rain types. However, at least over the Netherlands, we have been able to show that the 2CC scaling relation manifests itself over a larger range of dew point temperatures when the temporal resolution is increased from hourly to 10 minute intensities (chapter 2). Since the highest percentiles are expected to contain relatively more convective and less stratiform events when the temporal resolution is increased, this suggests that 2CC scaling is in fact robust for convective extreme precipitation. Instead, the apparent scale break for hourly data is caused by the pollution of the data by stratiform precipitation events for lower dew point temperatures.

2. Which local processes are responsible for the 2CC scaling relation?

A conceptual analysis of extreme precipitation scaling using a plume model and simple perturbations to the temperature profile under constant relative humidity can be found in chapter 2. Two processes are shown to be responsible for the scaling found; the integrated lateral moisture convergence in the cloud, and the cloud-base moisture flux. The former leads to an increase of approximately 2CC scaling, while the latter only shows an increase slightly greater than CC scaling. The updraft vertical velocity and the specific humidity control the relative contributions of these processes to the total scaling. This indicates the importance of these parameters.

The thermodynamical component is determined by surface-CC scaling through the cloud-base moisture flux, combined with a column integrated component through the lateral moisture convergence. As a result, the thermodynamic scaling is slightly greater than CC scaling, at 7% K^{-1}. The dynamical component adds another 3% K^{-1}, based on changes in the vertical velocity.

Finally, change in environmental stability is shown to influence the scaling, ranging from CC scaling when the temperature profile is perturbed following a moist adiabat (warming increases with tropospheric height), to 10% K^{-1} for a constant temperature perturbation. In midlatitudes climate perturbations appear to be better described by uniform perturbations than moist adiabatic perturbations, indicating that the precipitation response to warming might be higher here than in the tropics.

3. How does precipitation depend on atmospheric conditions and large-scale forcing?

The findings of chapter 2 shed light on the relevant processes and parameters on the local scales. However, local conditions are dependent on large-scale conditions and processes. The relations between large-scale atmospheric conditions and precipitation extremes were first studied in a statistical analysis in chapter 3, followed in chapter 4 by a LES sensitivity analysis for a case setup based on chapter 3.

In chapter 3 we have presented a statistical analysis of atmospheric conditions and controlling factors for the precipitating atmosphere. This was done by creating a dataset of coarsely separated precipitation events and using the peak intensities of these events to group data into deciles of increasing intensities. It was shown that heavy precipitation events tend to occur under warmer, moister conditions than weaker events, enduring stronger large-scale convergence. The temporal signal of these conditions becomes stronger for increasing deciles of peak intensities.

Chapter 4 consists of a sensitivity analysis of convective precipitation with respect to atmospheric stability, relative humidity, and large-scale moisture convergence based on large eddy simulations. These simulations were forced by the time dependent large-scale forcing conditions and atmospheric profiles for the upper decile of peak intensities over the Netherlands, as described in chapter 3. Precipitation responds differently to changes in relative humidity, atmospheric stability, and large-scale moisture convergence. Mean precipitation increases with relative humidity due to an increase in the precipitation area fraction. Both an increase in instability and large-scale convergence lead to a rise in precipitation. However, decomposition into precipitation intensity and area fraction shows that while the large-scale convergence almost exclusively influences the area fraction, the atmospheric stability primarily influences the precipitation intensity.

4. How are these relations affected by climate change?

The sensitivity analyses of chapter 4 were repeated for a future climate. The relations found for the present-day and future climate are very similar, indi-

cating that these relations are robust for a changing climate. The precipitation response to climate change is weaker than expected based on observed relations in the present-day climate, with a CC increase in the precipitation intensity for mean, and extreme intensities. The total precipitation response is lower than CC scaling, due to a decrease in the area fraction. In other words, this sensitivity analysis suggests that in a warmer climate, it will rain more intensely, but in less places.

5.2 Outlook

In chapter 1 it was mentioned that there are three aspects of extreme precipitation that determine the impact of extreme events; intensity, frequency and duration. The research presented in this thesis is primarily focused on the precipitation intensity, but also includes some insights in the area fraction of precipitation. In chapter 4 it was seen that the area fraction increases with stronger moisture convergence. The area fraction is a coarse measure for the frequency of occurrence, since more precipitating cells increase the area fraction of the domain. However, the area fraction can also increase due to increased event sizes. In order to understand what determines the frequency of occurrence and duration of an event and why, future work should include tracking of precipitation events in LES to analyze the frequency and duration of extreme events in a more systematic way.

While this thesis provides insight into different aspects of the behavior of convective extreme precipitation, it also poses some new research challenges. As discussed in section 1.5, one of the main challenges in studying convective extreme precipitation is identifying and connecting the different scale processes involved. In this thesis, we have identified relationships between precipitation intensities and both local and large-scale conditions and processes. It would be valuable to ascertain how the local scale processes presented in chapter 2 are influenced by the larger scales analyzed in chapter 3 and 4.

For example, based on a number of observational studies (e.g. Lenderink & Meijgaard, 2008; Loriaux et al., 2013), the response of the precipitation

intensity to warming is expected to be 6-7% per degree warming for the mean (CC scaling), and between 10-14% per degree warming for extremes (super-CC scaling). The response based on a conceptual model is in line with these results (chapter 2). Based on the LES simulations in chapter 4, the mean intensity increases by approximately CC scaling. However, the response of the extreme intensity is the same as the mean intensity. These results are surprising, given the strong super-CC scaling relations found over the Netherlands from observations in the present-day climate and a non-hydrostatic model climate perturbation (Attema et al., 2014).

As was discussed in sections 1.4 and, more thoroughly, 4.1, the local precipitation response is determined by dynamics, thermodynamics and the precipitation efficiency. In this thesis we have mostly focused on the (thermo)dynamic contributions to the precipitation response. As the thermodynamic contribution is close to CC scaling, a response close to this scaling can either mean that the dynamical and efficiency contributions are low, or that they balance each other out. The efficiency component is difficult to determine, as it incorporates processes such as entrainment, detrainment and microphysics, but the dynamical component can be calculated through the updraft velocity, as described in chapter 2.4.2. By comparing the combined (thermo)dynamical response to the model response, the importance of the precipitation efficiency can be inferred. Alternatively, a weak dynamical response might be caused by the lack of organization in our simulations, which has been shown to increase the precipitation response (Moseley et al., 2016). Using conditionally sampled profiles, it is possible to approximate a convective plume to determine the local conditions needed for these calculations.

To further study the small scale processes in relation to large-scale forcing, LES modeling should be continued, since the high resolution makes it a very suitable tool to study local conditions while it can be driven by realistic large-scale conditions. In order to achieve this, it is necessary to store relevant conditionally sampled profiles, or better yet, follow the precipitating events by means of event tracking. This will allow for the most accurate statistics related to extreme precipitation, whilst also providing useful event characteristics, such as peak intensity, duration and size. The local atmospheric conditions and processes accompanying the extreme events, can then be used in equation 4.1,

so that the conceptual analysis of chapter 2 can be repeated in a realistically modeled, three-dimensional framework.

Bibliography

J. T. Allen & D. J. Karoly. "A climatology of Australian severe thunderstorm environments 1979-2011: Inter-annual variability and ENSO influence." *Int. J. of Climatol.*, 34(1):81–97, 2014.

M. R. Allen & W. J. Ingram. "Constraints on future changes in climate and the hydrological cycle." *Nature*, 419:224–232, 2002.

J. J. Attema, et al. "Extreme precipitation response to climate perturbations in an atmospheric mesoscale model." *Environ. Res. Lett.*, 9(1):014003, 2014.

S. Barkidija, Sandaija & Ž. Fuchs. "Precipitation correlation between convective available potential energy, convective inhibition and saturation fraction in middle latitudes." *Atmos. Res.*, 124:170–180, 2013.

P. Berg & J. O. Haerter. "Unexpected increase in precipitation intensity with temperature – a result of mixing of precipitation types?" *Atmos. Res.*, 119:56–61, 2013.

P. Berg, et al. "Strong increase in convective precipitation in response to higher temperatures." *Nat. Geosci.*, 6(3):181–185, 2013.

S. Blenkinsop, et al. "Temperature influences on intense UK hourly precipitation and dependency on large-scale circulation." *Environ. Res. Lett.*, 10(5):054021, 2015.

S. J. Böing, et al. "Detrainment in deep convection." *Geophys. Res. Lett.*, 39(20), 2012.

S. J. Böing, et al. "Influence of the subcloud layer on the development of a deep convective ensemble." *J. Atmos. Sci.*, 69(9):2682–2698, 2012.

D. Bolton. "The computation of equivalent potential temperature." *Mon. Wea. Rev.*, 108:1046–1053, 1980.

C. S. Bretherton & M. E. Peters. "Relationships between water vapor path and precipitation over the tropical oceans." *J. Climate*, 17:1517–1528, 2004.

Buienradar. "Buienradar terugkijken." http://www.buienradar.nl/radararchief, 2016. [Online; accessed 6-June-2016].

J. L. Catto & S. Pfahl. "The importance of fronts for extreme precipitation." *J. Geophys. Res.: Atmos.*, 118(19):10,791–10,801, 2013.

J. P. Charba. *Operational system for predicting thunderstorms two to six hours in advance*. National Weather Service, NOAA, 1977.

J. P. Craven & H. E. Brooks. "Baseline Climatology of Sounding Derived Parameters Associated with Deep, Moist Convection." *Natl. Wea. Dig.*, 28:13–24, 2004.

S. Dal Gesso, et al. "A mixed-layer model perspective on stratocumulus steady states in a perturbed climate." *Quart. J. Roy. Meteor. Soc.*, 140(684):2119–2131, 2014.

L. Davies, et al. "Relationships between the large-scale atmosphere and the small-scale convective state for Darwin, Australia." *J. Geophys. Res.: Atmos.*, 118(20):11,534–11,545, 2013.

D. P. Dee & Coauthors. "The ERA-Interim reanalysis: configuration and performance of the data assimilation system." *Q. J. R. Meteorol. Soc.*, 137(656):553–597, 2011.

J. Dorrestijn, et al. "Stochastic parameterization of convective area fractions with a multicloud model inferred from observational data." *J. Atmos. Sci.*, 72(2):854–869, 2014.

C. A. Doswell & L. F. Bosart. "Extratropical Synoptic-Scale Processes and Severe Convection." *Meteor. Monogr.*, 28(50):27–70, 2001.

C. A. Doswell, et al. "Flash Flood Forecasting: An Ingredients-Based Methodology." 1996.

V. Ducrocq & Coauthors. "HyMeX-SOP1, the field campaign dedicated to heavy precipitation and flash flooding in the northwestern Mediterranean." *Bull. Amer. Meteor. Soc.*, 95:1083–1100, 2013.

L. L. Dyson, et al. "A baseline climatology of sounding-derived parameters associated with heavy rainfall over Gauteng, South Africa." *Int. J. of Climatol.*, 127(March 2014):114–127, 2014.

K. A. Emanuel. *Atmospheric convection*. Oxford University Press, 1994.

S. Emori & S. J. Brown. "Dynamic and thermodynamic changes in mean and extreme precipitation under changed climate." *Geophys. Res. Lett.*, 32(17), 2005.

D. M. W. Frierson. "Robust increases in midlatitude static stability in simulations of global warming." *Geophys. Res. Lett.*, 33(24), 2006.

L. Gaál, et al. "Selection of intense rainfall events based on intensity thresholds and lightning data in Switzerland." *Hydrol. Earth Syst. Sci.*, 18(5):1561–1573, 2014.

J. O. Haerter & P. Berg. "Unexpected rise in extreme precipitation caused by a shift in rain type?" *Nat. Geosci.*, 2:372–373, 2009.

W. H. Hand, et al. "A study of twentieth-century extreme rainfall events in the United Kingdom with implications for forecasting." *Meteorol. Appl.*, 11(1):15–31, 2004.

R. Hardwick-Jones, et al. "Observed relationships between extreme sub-daily precipitation, surface temperature, and relative humidity." *Geophys. Res. Lett.*, 37, 2010a.

R. Hardwick-Jones, et al. "Observed relationships between extreme sub-daily precipitation, surface temperature, and relative humidity." *Geophys. Res. Lett.*, 37, 2010b.

W. Hazeleger, et al. "Ec-earth v2. 2: description and validation of a new seamless earth system prediction model." *Climate Dynam.*, 39(11):2611–2629, 2012.

T. Heus, et al. "Formulation of and numerical studies with the dutch atmospheric large-eddy simulation (dales)." *Geosci. Model Dev. Disc.*, 3(1):99–180, 2010.

C. E. Holloway & J. D. Neelin. "Moisture vertical structure, column water vapor and tropical deep convection." *J. Atmos. Sci.*, 66(6):1665–1683, 2009.

R. a. Houze. "Mesoscale convective systems." *Rev. Geophys.*, 42(4):1–43, 2004.

IPCC. *Climate Change 2013: The physical science basis: Working group I contribution to the fifth assessment report of the Intergovernmental Panel on Climate Change*. Cambridge University Press, 2014.

J. V. Iribarne & W. L. Godson. *Atmospheric Thermodynamics*. Geophysics Astrophysics Monographs. Kluwer, 1981.

E. Kessler. *On Distribution and Continuity of Water Substance in Atmospheric Circulation*. Meteorological Monograph Series. American Meteorological Society, 1969.

KNMI. "Uurgegevens van het weer in Nederland." http://www.knmi.nl/klimatologie/uurgegevens, 2014. [Online; accessed 13-November-2014].

KNMI. "Geografische overzichten van het weer in Nederland." http://www.knmi.nl/nederland-nu/klimatologie/geografische-overzichten, 2016a. [Online; accessed 4-June-2016].

KNMI. "Weerkaarten archief Europa." https://www.knmi.nl/nederland-nu/klimatologie/daggegevens/weerkaarten, 2016b. [Online; accessed 4-June-2016].

G. Lenderink & E. van Meijgaard. "Linking increases in hourly precipitation extremes to atmospheric temperature and moisture changes." *Environ. Res. Lett.*, 5:025208, 2010.

G. Lenderink, et al. "Scaling and trends of hourly precipitation extremes in two different climate zones – hong kong and the netherlands." *Hydrol. Earth Syst. Sci.*, 15:3033–3041, 2011.

G. Lenderink & J. Attema. "A simple scaling approach to produce climate scenarios of local precipitation extremes for the Netherlands." *Environ. Res. Lett.*, 10(8):085001, 2015.

G. Lenderink & E. v. Meijgaard. "Increase in hourly precipitation extremes beyond expectations from temperature changes." *Nat. Geosci.*, 1(8):511–514, 2008.

C. Lepore, et al. "Temperature and cape dependence of rainfall extremes in the eastern united states." *Geophys. Res. Lett.*, 42(1):74–83, 2015. 2014GL062247.

J. M. Loriaux, et al. "Understanding convective extreme precipitation scaling using observations and an entraining plume model." *J. Atmos. Sci.*, 70(11):3641–3655, 2013.

J. M. Loriaux, et al. "Composite case of conditions leading to high peak precipitation intensities in the Netherlands [Data files].", 2016a. Available from doi:10.4121/uuid:e066b7f5-f83b-406b-93e8-6ba3eb3659eb.

J. M. Loriaux, et al. "Peak precipitation intensity in relation to atmospheric conditions and large-scale forcing at midlatitudes." *J. Geophys. Res.: Atmos.*,

121(10):5471–5487, 2016b.

E. E. Maeda, et al. "Decreasing precipitation extremes at higher temperatures in tropical regions." *Nat. Hazards*, 2012.

E. v. Meijgaard, et al. *The KNMI regional atmospheric climate model RACMO version 2.1*. Koninklijk Nederlands Meteorologisch Instituut, 2008.

S.-K. Min, et al. "Human contribution to more-intense precipitation extremes." *Nature*, 470(7334):378–381, 2011.

V. Mishra, et al. "Relationship between hourly extreme precipitation and local air temperature in the united states." *Geophys. Res. Lett.*, 39(16):L16403, 2012.

P. Molnar, et al. "Storm type effects on super Clausius-Clapeyron scaling of intense rainstorm properties with air temperature." *Hydrol. Earth Syst. Sci.*, 19(4):1753–1766, 2015.

C. Moseley, et al. "Intensification of convective extremes driven by cloud-cloud interaction." *Nature Geosci*, 9(10):748–752, 2016.

C. J. Muller, et al. "Intensification of precipitation extremes with warming in a cloud-resolving model." *J. Climate*, 24:2784–2800, 2011.

C. J. Muller. "Impact of convective organization on the response of tropical precipitation extremes to warming." *J. Climate*, 26(14):5028–5043, 2013.

NRC. "Rode cijfers Achmea wegens schade noodweer." http://www.nrc.nl/nieuws/2016/07/11/rode-cijfers-achmea-wegens-schade-noodweer-a1510926, 2016. [Online; accessed 4-June-2016].

P. A. O'Gorman & T. Schneider. "The physical basis for increases in precipitation extremes in simulations of 21st-century climate change." *Proc. Natl. Acad. Sci. U.S.A.*, 106:14773–14777, 2009a.

P. A. O'Gorman & T. Schneider. "Scaling of precipitation extremes over a wide range of climates simulated with an idealized gcm." *J. Climate*, 22:5676–5685, 2009b.

P. A. O'Gorman. "Sensitivity of tropical precipitation extremes to climate change." *Nature Geosci*, 5(10):697–700, 2012.

P. A. O'Gorman. "Precipitation extremes under climate change." *Curr. Clim. Chang. Rep.*, 1(2):49–59, 2015.

G. J. van Oldenborgh, et al. "Rapid attribution of the May/June 2016 flood-inducing precipitation in France and Germany to climate change." *Hydrol.*

Earth Syst. Sci. Discuss., 3:1–23, 2016.

P. Pall, et al. "Testing the clausius–clapeyron constraint on changes in extreme precipitation under co_2 warming." *Climate Dynam.*, 28:351–363, 2007.

P. Pall, et al. "Anthropogenic greenhouse gas contribution to flood risk in england and wales in autumn 2000." *Nature*, 470(7334):382–385, 2011.

O. Peters & J. D. Neelin. "Critical phenomena in atmospheric precipitation." *Nat. Phys.*, 2:393–396, 2006.

S. Pfahl & H. Wernli. "Quantifying the relevance of cyclones for precipitation extremes." *J. Climate*, 25(19):6770–6780, 2012.

D. M. Romps. "Response of tropical precipitation to global warming." *J. Atmos. Sci.*, 68(1):123–138, 2011.

S. R. de Roode, et al. "Parameterization of the vertical velocity equation for shallow cumulus clouds." *Mon. Wea. Rev.*, 140(8):2424–2436, 2012.

W. C. de Rooy & A. P. Siebesma. "A simple parameterization for detrainment in shallow cumulus." *Mon. Wea. Rev.*, 136:560–576, 2008.

T. Schneider & P. A. O'Gorman. "Moist convection and the thermal stratification of the extratropical troposphere." *J. Atmos. Sci.*, 65(11):3571–3583, 2008.

S. C. Sherwood, et al. "Relative humidity changes in a warmer climate." *J. Geophys. Res.: Atmos.*, 115(D9), 2010.

A. P. Siebesma. "Shallow cumulus convection." In *Buoyant Convection in Geophysical Flows*, editors E.J.Plate, et al., 17-27 March NATO Advanced Study Institute, pages 441–486. Kluwer, Pforzheim, Germany, 1998.

A. P. Siebesma & A. A. M. Holtslag. "Model impacts of entrainment and detrainment rates in shallow cumulus convection." *J. Atmos. Sci.*, 53:2354–2364, 1996.

M. S. Singh & P. A. O'Gorman. "Influence of microphysics on the scaling of precipitation extremes with temperature." *Geophys. Res. Lett.*, 41(16):6037–6044, 2014.

M. S. Singh & P. A. O'Gorman. "Increases in moist-convective updraught velocities with warming in radiative-convective equilibrium." *Quart. J. Roy. Met. Soc.*, 141(692):2828–2838, 2015.

A. Singleton & R. Toumi. "Super-clausius–clapeyron scaling of rainfall in a model squall line." *Quart. J. Roy. Meteor. Soc.*, 139(671):334–339, 2013.

T. H. M. Stein, et al. "The DYMECS Project: A Statistical Approach for the Evaluation of Convective Storms in High-Resolution NWP Models." *Bull. Amer. Meteor. Soc.*, 96(6):939–951, 2015.

G. L. Stephens & T. D. Ellis. "Controls of global-mean precipitation increases in global warming gcm experiments." *J. Climate*, 21(23):6141–6155, 2008.

R. B. Stull. *An Introduction to Boundary Layer Meteorology*, volume 13. Springer Science & Business Media, 1988.

H. Sundqvist. "A parameterization scheme for non-convective condensation including prediction of cloud water content." *Quart. J. Roy. Met. Soc.*, 104:677–690, 1978.

K. E. Taylor, et al. "An overview of cmip5 and the experiment design." *Bull. Amer. Meteor. Soc.*, 93(4):485–498, 2012.

M. Tiedtke. "A comprehensive mass flux scheme for cumulus parameterization in large-scale models." *Mon. Wea. Rev.*, 117:1779–1800, 1989.

K. E. Trenberth, et al. "The changing character of precipitation." *Bull. Amer. Meteor. Soc.*, 84:1205–1217, 2003.

N. Utsumi, et al. "Does higher surface temperature intensify extreme precipitation?" *Geophys. Res. Lett.*, 38(16), 2011.

E. Van Meijgaard, et al. *The KNMI regional atmospheric climate model RACMO version 2.1*. Koninklijk Nederlands Meteorologisch Instituut, 2008.

M. L. Weisman & J. B. Klemp. "The dependence of numerically simulated convective storms on vertical wind shear and buoyancy." *Mon. Wea. Rev.*, 110:504–520, 1982.

S. Westra, et al. "Future changes to the intensity and frequency of short-duration extreme rainfall." *Rev. Geophys.*, 52(3):522–555, 2014.

G. J. Zhang. "Convective quasi-equilibrium in midlatitude continental environment and its effect on convective parameterization." *J. Geophys. Res.: Atmos.*, 107(D14):ACL 12–1–ACL 12–16, 2002.

G. J. Zhang. "Convective quasi-equilibrium in the tropical western Pacific: Comparison with midlatitude continental environment." *J. Geophys. Res.: Atmos.*, 108(D19):ACL 1–1–ACL 1–10, 2003.

About the author

May 24, 1985	Born in Amsterdam
1998 - 2003	Het Nieuwe Lyceum, Bilthoven
2005 - 2009	Bachelor degree in Earth Sciences, Utrecht University with honors
2009 - 2011	Master degree in Meteorology, Physical Oceanography and Climate, Utrecht University cum laude
2011 - 2016	PhD position as part of the project "Kennis voor Klimaat", Royal Netherlands Meteorological Institute (KNMI) and Delft University of Technology
2016 - Present	Postdoc position on climate effects on sustainable energy technology, Radboud University, Nijmegen

List of journal publications

- G. Lenderink, R. Barbero, J.M. Loriaux, H., *Super Clausius-Clapeyron scaling of extreme hourly precipitation and its relation to large-scale atmospheric conditions*, submitted to J. Climate
- J.M. Loriaux, G. Lenderink, A.P. Siebesma, *Large-Scale Controls on Extreme Precipitation*, accepted, J. Climate, doi:10.1175/JCLI-D-16-0381.1
- J.M. Loriaux, G. Lenderink, A.P. Siebesma, *Peak precipitation intensity in relation to atmospheric conditions and large-scale forcing at midlatitudes*, 2016, J. Geoph. Res.: Atmos., doi:10.1002/2015JD024274
- J.J. Attema, J.M. Loriaux, G. Lenderink, *Extreme precipitation response to climate perturbations in an atmospheric mesoscale model*, 2014, Environ. Res. Lett., doi:10.1088/1748-9326/9/1/014003
- J.M. Loriaux, G. Lenderink, A.P. Siebesma, S.R. de Roode, *Understanding Convective Extreme Precipitation Scaling Using Observations and an Entraining Plume Model*, 2013, J. Atmos. Sci., doi:10.1175/JAS-D-12-0317.1

Dankwoord

Alweer 5.5 jaar geleden kwam ik op gesprek bij Pier, Geert en Stephan om te praten over dit project. Ik was toen nog bezig met mijn master scriptie, en had eigenlijk nog helemaal geen idee van wat het doen van een promotieonderzoek inhield. Ik heb het als een enorm voorrecht ervaren om met Pier en Geert, en voor het eerste paper ook met Stephan en zijn aanstekelijke enthousiasme, aan dit onderzoek te werken.

Geert, ik kon altijd bij je aankloppen als ik ergens op vastliep, en als ik even niets van me liet horen kwam je altijd even kijken of het nog wel goed ging. Jouw oog voor detail heeft mij geleerd om niet te snel conclusies te trekken en wat uitgebreider naar dingen te kijken dan ik uit mezelf zou doen. Pier, jouw talent om in grote lijnen te denken vond ik altijd erg inspirerend en ik moest altijd erg lachen om je wilde verhalen en grapjes. De manier waarop je mijn onderzoek altijd promootte bij andere grote wetenschappers heeft voor mij zeker veel deuren geopend. Ik wil jullie beiden bedanken voor deze mooie, leerzame tijd.

Ik wil ook mijn collega's op het KNMI bedanken voor de gezelligheid en goede ideeën. Ook aan mijn groep in Delft heb ik warme herinneringen. De wekelijkse paper discussions, de koffiepauzes met Sara en 'de jongens', het was de vele treinvertragingen meer dan waard. Mijn paranimfen, Eveline en Anna, wil ik in het bijzonder bedanken voor alle steun, klaagmomentjes, en lachbuien. Meisjes, bij jullie kon ik altijd terecht. Eveline, ik ben ervan overtuigd dat ik zonder onze weekendsessies nog lang niet klaar was geweest.

Mark, ik wil jou bedanken voor het geduld en vertrouwen dat je in me gesteld hebt door me aan mijn postdoc te laten beginnen toen ik nog verre van klaar

was met mijn proefschrift.

Naast mijn collega's had ik dit nooit af kunnen krijgen zonder de steun van mijn ouders, Daan en Anne en andere vrienden en familie. Mam en pap, duizend maal dank voor de vele oppassessies, en het proeflezen van mijn thesis. Vrienden en familie, bedankt voor jullie belangstelling en vooral ook begrip en geduld als ik weer eens tegen een deadline aanzat en helemaal niet zo gezellig was.

Tot slot wil ik natuurlijk Timo en Amber bedanken. Amber, bedankt voor de vrolijke afleiding als ik gestrest thuiskwam van werk en voor je onvoorwaardelijke liefde, ook al moest je het laatste jaar wat vaker een extra dagje naar de creche of bij opa en oma logeren. Timo, bedankt voor je geduld, je steun, je liefde en begrip.